Assessment of Energy Storage and Dynamic Response Requirements in Modular Multilevel Converters for Frequency Response Improvement

by

Ashley Wing Yan Ng

A thesis submitted to the Faculty of Graduate Studies of
The University of Manitoba
in partial fulfilment of the requirements of the degree of

Master of Science

Department of Electrical and Computer Engineering
University of Manitoba
Winnipeg, Canada

Copyright © 2022 Ashley Wing Yan Ng

Abstract

The call for clean energy has driven the power system to become increasingly dominated by renewable energy sources (RESs). This has led to a reduced proportion of power contributions by conventional synchronous generators. As a result, the grid is becoming more prone to frequency excursions from fluctuations between the electrical generation and demand due to the decreasing system inertia. RESs are interfaced to the grid by power electronic converters, such as the modular multilevel converter (MMC). The MMC has an inherent energy storage that can be dynamically controlled. This capability has been used to compensate power imbalances and effectively reduce the magnitude of the consequent frequency excursions.

The research in this thesis investigates how different system parameters and operating conditions impact the ability of such energy-based frequency support control to improve the frequency response, through detailed electromagnetic transients (EMT) simulations in PSCAD/EMTDC. One important factor is the response speed of the MMC. A model is proposed to simulate the dynamics of the DC voltages and currents in the MMC, from which a closed-form equation is derived to approximate its settling time. The model is validated by EMT simulations and used to investigate how varying system parameters and operating conditions impact the MMC response speed. It may be used as a design tool in determining operating and sizing requirements for the MMC with frequency support capability.

Table of Contents

Abstract i

Table of Contents ii

List of Figures v

List of Tables xii

1 Introduction 1

1.1 Background 1

1.2 Problem Definition 3

1.3 Research Objectives 4

1.4 Thesis Organization 5

2 Literature Review 7

2.1 MMC Fundamentals 7

2.1.1 Topology 7

2.1.2 Switching Signal Generation 11

2.2 Conventional Control Methods 15

2.2.1 Direct Control 15

2.2.2 Decoupled Control 17

2.2.3 Circulating Current Suppression Control 18

2.2.4 Phase-Locked Loop 20
2.3 Frequency Support Methods 20
2.3.1 Inertia Emulation Approach 21
2.3.2 Energy Control Approach 22
2.4 Capacitor Sizing Methods 25
2.5 Summary 26

3 Control of the Energy Stored in MMCs 28
3.1 Concepts and Implementation of Energy Control 29
3.2 Test System 36
3.3 Parametric Study on Energy Control 39
3.3.1 MMC with Small Energy Storage 39
3.3.2 MMC with Large Energy Storage 51
3.3.3 Inertia of Synchronous Generators 61
3.4 Summary 63

4 Response Speed Modelling and Sizing Considerations of MMCs 66
4.1 Derivation of Mathematical Model 67
4.2 Validation of Mathematical Model 76
4.2.1 Settling Time Extraction Algorithms 81
4.3 Parametric Study on Response Speed 82
4.3.1 SM Capacitance and Arm Inductance 83
4.3.2 SM Capacitance and Modulation Index 89
4.3.3 SM Capacitance and Load Power Factor 94
4.4 Summary 100

5 Contributions, Conclusions, and Recommendations for Future Work . . 101

5.1 Main Contributions and Conclusions 102

5.2 Future Work 104

Appendix A Model Equations 106

A.1 λ Equations 106

A.1.1 Special Case: Fundamental Component Only in m^{ref} 108

A.2 ξ Equations 108

References 110

List of Figures

1.1 Converter as interface between DC RESs and AC grid. 3

2.1 Conventional three-phase MMC topology. 8
2.2 Conventional submodule topologies. 9
2.3 Half-bridge submodule states. 10
2.4 Basis of PWM operation. 12
2.5 Basis of NLC operation. 13
2.6 Equivalent circuit of MMC connected to an AC system. 15
2.7 Controllers used for PV/PQ control. 16
2.8 Controllers used for decoupled AC active power and AC voltage control. . . . 18
2.9 Block diagram for phase-locked loop. 21

3.1 Energy controller integrated with conventional control schemes. 30
3.2 Energy controller scheme to vary the energy stored in an MMC. 30
3.3 Example frequency response with and without energy control; (b) is a zoom in of (a) on the dotted boxed region. 33
3.4 Example capacitor voltage response with and without energy control. 34
3.5 Example power responses with (solid lines) and without (dashed lines) energy control. 35
3.6 Test system for MMC with energy control connected with SGs. 36

3.7 Sample result of the system frequency responses under varying RES penetration levels with (solid lines) and without (dashed lines) energy control. . . . 40
3.8 Sample result of the SM voltage responses under varying RES penetration levels with (solid lines) and without (dashed lines) energy control. 41
3.9 Comparison of frequency nadirs by (a) magnitude for with (solid lines) and without (dashed lines) energy control, and by (b) percent improvement under varying energy storage capacities and RES penetration levels with MMC 1 subjected to a 2% increase in load. 43
3.10 Comparison of times to reach the frequency nadir after the perturbation occurs by (a) magnitude for with (solid lines) and without (dashed lines) energy control, and by (b) percent improvement under varying energy storage capacities and RES penetration levels with MMC 1 subjected to a 2% increase in load. 45
3.11 Comparison of frequency nadirs by (a) magnitude for with (solid lines) and without (dashed lines) energy control, and by (b) percent improvement under varying energy storage capacities and RES penetration levels with MMC 1 subjected to a 5% increase in load. 47
3.12 Comparison of the percent improvement in the frequency nadir due to energy control between a 2% and 5% increase in load under varying energy storage capacities and RES penetration levels with MMC 1. 48

3.13 Comparison of times to reach the frequency nadir after the perturbation occurs by (a) magnitude for with (solid lines) and without (dashed lines) energy control, and by (b) percent improvement under varying energy storage capacities and RES penetration levels with MMC 1 subjected to a 5% increase in load. 50
3.14 Comparison of the percent improvement in the time to reach the frequency nadir after the perturbation occurs due to energy control between a 2% and 5% increase in load under varying energy storage capacities and RES penetration levels with MMC 1. 51
3.15 Comparison of frequency nadirs by (a) magnitude for with (solid lines) and without (dashed lines) energy control, and by (b) percent improvement under varying energy storage capacities and RES penetration levels with MMC 2 subjected to a 2% increase in load. 53
3.16 Comparison of times to reach the frequency nadir after the perturbation occurs by (a) magnitude for with (solid lines) and without (dashed lines) energy control, and by (b) percent improvement under varying energy storage capacities and RES penetration levels with MMC 2 subjected to a 2% increase in load. 55
3.17 Comparison of frequency nadirs by (a) magnitude for with (solid lines) and without (dashed lines) energy control, and by (b) percent improvement under varying energy storage capacities and RES penetration levels with MMC 2 subjected to a 5% increase in load. 57

3.18 Comparison of the percent improvement in the frequency nadir due to energy control between a 2% and 5% increase in load under varying energy storage capacities and RES penetration levels with MMC 2. 58
3.19 Comparison of times to reach the frequency nadir after the perturbation occurs by (a) magnitude for with (solid lines) and without (dashed lines) energy control, and by (b) percent improvement under varying energy storage capacities and RES penetration levels with MMC 2 subjected to a 5% increase in load. 59
3.20 Comparison of the percent improvement in the time to reach the frequency nadir after the perturbation occurs due to energy control between a 2% and 5% increase in load under varying energy storage capacities and RES penetration levels with MMC 2. 60
3.21 Comparison of frequency nadirs by (a) magnitude for with (solid lines) and without (dashed lines) energy control, and by (b) percent improvement under varying energy storage capacities and SG inertia constants with MMC 1. . . 62
3.22 Comparison of the times to frequency nadirs by (a) magnitude for with (solid lines) and without (dashed lines) energy control, and by (b) percent improvement under varying energy storage capacities and SG inertia constants with MMC 1. 64

4.1 MMC KVL paths. 70

4.2 Comparison of responses from the model and PSCAD/EMTDC simulation to a +5% change in V_{DC} with $C_{\mathrm{sm}} = 4000$ μF and $L_{\mathrm{arm}} = 50$ mH for (a) SM voltage [kV] and (b) arm current [kA] responses where the solid lines are the full waveform, and the dashed lines are the averaged waveform, and (c) power [MW] responses where the solid lines are when with CCSC, and the dashed lines are when without CCSC. (Continued on next page) 77

4.2 (Continued from previous page) Comparison of responses from the model and PSCAD/EMTDC simulation to a +5% change in V_{DC} with $C_{\mathrm{sm}} = 4000$ μF and $L_{\mathrm{arm}} = 50$ mH for (a) SM voltage [kV] and (b) arm current [kA] responses where the solid lines are the full waveform, and the dashed lines are the averaged waveform, and (c) power [MW] responses where the solid lines are when with CCSC, and the dashed lines are when without CCSC. 78

4.3 Comparison of responses from the model and PSCAD/EMTDC simulation to a +5% change in V_{DC} with $C_{\mathrm{sm}} = 4000$ μF and $L_{\mathrm{arm}} = 15$ mH for (a) SM voltage [kV] and (b) arm current [kA] responses where the solid lines are the full waveform, and the dashed lines are the averaged waveform, and (c) power [MW] responses. (Continued on next page) 80

4.3 (Continued from previous page) Comparison of responses from the model and PSCAD/EMTDC simulation to a +5% change in V_{DC} with $C_{\mathrm{sm}} = 4000$ μF and $L_{\mathrm{arm}} = 15$ mH for (a) SM voltage [kV] and (b) arm current [kA] responses where the solid lines are the full waveform, and the dashed lines are the averaged waveform, and (c) power [MW] responses. 81

4.4 SM voltage settling times with perturbation of (a) +5% (b) −10% (c) +2% change in V_{DC} for SM capacitance and arm inductance parametric analysis. Time bounds predicted by model in lower opacity, measured time in higher opacity. (Continued on next page) 84

4.4 (Continued from previous page) SM voltage settling times with perturbation of (a) +5% (b) −10% (c) +2% change in V_{DC} for SM capacitance and arm inductance parametric analysis. Time bounds predicted by model in lower opacity, measured time in higher opacity. 85

4.5 Error of model SM voltage settling times subjected to a perturbation of (a) +5% (b) −10% (c) +2% change in V_{DC} for the SM capacitance and arm inductance parametric analysis considering (d) peak-to-peak SM voltage ripple. (Continued on next page) 87

4.5 (Continued from previous page) Error of model SM voltage settling times subjected to a perturbation of (a) +5% (b) −10% (c) +2% change in V_{DC} for the SM capacitance and arm inductance parametric analysis considering (d) peak-to-peak SM voltage ripple. 88

4.6 SM voltage settling times with perturbation of (a) +5% (b) −10% (c) +2% change in V_{DC} for SM capacitance and modulation index parametric analysis. Time bounds predicted by model in lower opacity, measured time in higher opacity. (Continued on next page) 90

4.6 (Continued from previous page) SM voltage settling times with perturbation of (a) +5% (b) −10% (c) +2% change in V_{DC} for SM capacitance and modulation index parametric analysis. Time bounds predicted by model in lower opacity, measured time in higher opacity. 91

4.7 Error of model SM voltage settling times subjected to a perturbation of (a) +5% (b) −10% (c) +2% change in V_{DC} for the SM capacitance and modulation index parametric analysis considering (d) peak-to-peak SM voltage ripple. (Continued on next page) 92
4.7 (Continued from previous page) Error of model SM voltage settling times subjected to a perturbation of (a) +5% (b) −10% (c) +2% change in V_{DC} for the SM capacitance and modulation index parametric analysis considering (d) peak-to-peak SM voltage ripple. 93
4.8 SM voltage settling times with perturbation of (a) +5% (b) −10% (c) +2% change in V_{DC} for SM capacitance and power factor parametric analysis. Time bounds predicted by model in lower opacity, measured time in higher opacity. (Continued on next page) 96
4.8 (Continued from previous page) SM voltage settling times with perturbation of (a) +5% (b) −10% (c) +2% change in V_{DC} for SM capacitance and power factor parametric analysis. Time bounds predicted by model in lower opacity, measured time in higher opacity. 97
4.9 Error of model SM voltage settling times subjected to a perturbation of (a) +5% (b) −10% (c) +2% change in V_{DC} for the SM capacitance and power factor parametric analysis considering (d) peak-to-peak SM voltage ripple. (Continued on next page) 98
4.9 (Continued from previous page) Error of model SM voltage settling times subjected to a perturbation of (a) +5% (b) −10% (c) +2% change in V_{DC} for the SM capacitance and power factor parametric analysis considering (d) peak-to-peak SM voltage ripple. 99

List of Tables

2.1 Half-Bridge Submodule Switch Configurations 11

3.1 Synchronous Generator Parameters 37
3.2 MMC Parameters 37
3.3 Values used in SM Capacitance and RES Penetration Parametric Analysis for MMC 1 39
3.4 Values used in SM Capacitance and RES Penetration Parametric Analysis for MMC 2 52
3.5 Values used in SM Capacitance and Inertia Constant Parametric Analysis . . 61

4.1 MMC System Parameters 76
4.2 Values used in SM Capacitance and Arm Inductance Parametric Analysis . . 83
4.3 Values used in SM Capacitance and Modulation Index Parametric Analysis . 89
4.4 Values used in SM Capacitance and Load Power Factor Parametric Analysis 94
4.5 Values of Load Components for Different Power Factors 95

Chapter 1

Introduction

1.1 Background

An equilibrium between electrical energy generation and demand in power systems is not always attained. Limits of the available generation profiles, dynamics of the demand, and contingencies are among factors that disturb the power balance. When such power imbalances occur, the system frequency deviates from its nominal value. Proper countermeasures must, therefore, be set in place to regulate the frequency and prevent instability.

In conventional AC power systems dominated by synchronous generators (SGs), the inertia of the large rotating masses help maintain the frequency near its nominal value (e.g., 60 Hz in North America). The kinetic energy of the rotating masses is autonomously changed according to the frequency deviation as per the swing equation, and helps to restore the power balance [1]. In other words, the inertial nature of the rotating shaft serves as a reservoir of energy that can help maintain the system frequency when imbalances between the generation and load occur. This is referred to as primary frequency control and helps

to prevent significant frequency deviations. Secondary frequency control is triggered after to help restore the power balance. Then, tertiary frequency control is executed by system operators to change the states of the generating units accordingly [2].

In response to the call for clean energy, the demand for renewable energy sources (RESs) has been on the rise [3,4]. Consequently, the proportion of generation from RESs to generation from SGs is increasing, and will continue to do so. With RESs typically located far from where the energy is used, low-loss power transfer over long distances is essential. This is one of the main reasons why high-voltage direct current (HVDC) transmission systems are being used to connect RESs to the AC grid [5–7]. HVDC transmission is generally categorized by two converter types, namely line-commutated converters (LCCs) and voltage-sourced converters (VSCs) [8, 9]. Both converters have been studied extensively in literature, and it has been concluded that the VSC alternative is more suitable for HVDC applications because of its superior power control, better harmonic performance, and efficiency [10, 11].

The concept of multilevel VSCs eventually brought forth the modular multilevel converter (MMC) topologies. The MMC can be seen as a multilevel VSC and is built upon a number of series-connected submodules (SMs) [12, 13]. Its high modularity and ease of scalability, along with its efficiency and improved harmonic performance over conventional VSCs have demonstrated its potential [14–17]. In recent years, the MMC has become a top candidate for HVDC applications [6, 18–21].

It is important to note that the RESs generally produce DC power or AC power that is unsuitable for direct connection to an AC system, and are, therefore, connected to the AC grid via static power electronic converters [3, 22, 23]. As a result of this inverter-based interface, the rotating masses that the power system conventionally relies on to dampen the frequency excursions is not present. As illustrated in Fig. 1.1, the converter acts as

an interface between the DC RESs and the AC grid. This may include connections with transmission lines (represented by the short-line model for simplicity) on both sides, and a DC-link capacitor on the converter's DC-side to help maintain the DC-side voltage.

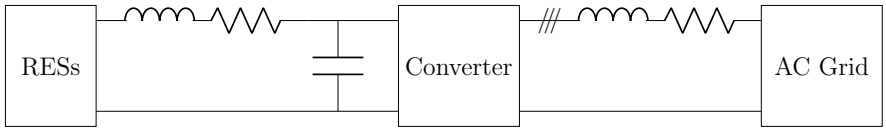

Fig. 1.1: Converter as interface between DC RESs and AC grid.

With the converter not inherently possessing inertia, the overall inertia of the power system will consequently decrease and become more prone to instability. Studies in [24], for example, have already shown the trend of the decreasing inertia in the Eastern Interconnection in North America. This concern must be addressed in order to ensure that the power system complies with the grid standards and codes [25, 26], and continues to operate with adequate security margins.

1.2 Problem Definition

The SGs have been conventionally relied on to mitigate the frequency excursions that occur due to perturbations in the power system. This is because of their inherently large inertia. However, as RESs take up a higher proportion in generation portfolios, the system inertia decreases and the inherent frequency damping may no longer be sufficient. The decommissioning of SGs as renewables are brought into service accelerates the erosion of system inertia. The frequency excursions must be mitigated by an alternative means.

A general solution is to augment the control functions of an MMC to include the additional role of supporting the system frequency, since it already acts as the interface between

the RESs and the AC grid. This consideration is possible because of the MMC's inherent capability to supply and absorb energy. The use of MMCs for frequency support in HVDC systems has taken on several approaches, but the common trait among them is that the converter's control schemes are implemented to achieve this additional capability. In other words, the MMC does not inherently possess a large inertia like SGs, but its energy control schemes can be used to achieve the same effect, albeit with limitations and differences. However, the implementation details such as controller parameters are dependent on the system. For example, some systems may be inherently more resilient against frequency excursions than other systems, and would, therefore, have different controller requirements. Some contributing factors may be governed by the sizing of the components of the MMC. Furthermore, as system penetration levels continue to increase, the controller functionalities may be compromised and there may also be implications on the sizing requirements. It is therefore necessary to investigate these relationships and evaluate the trade-offs.

1.3 Research Objectives

The main objectives of this research and methodologies adopted to address them are described as follows:

- *Implementation of an energy-based control frequency support scheme in an MMC system.* This will be done by augmenting the conventional control system of an MMC with provisions to allow short-term energy transactions with the SM capacitors.

- *Investigation and analysis of the effectiveness of MMC energy control in mitigating frequency excursions.* The impact of energy control on the frequency nadir and the duration of the arresting period will be quantitatively evaluated under different system

conditions in a series of parametric studies through detailed electromagnetic transients (EMT) simulations (in PSCAD/EMTDC).

- *Development of an explicit mathematical model for component sizing of the MMC under different system and operating conditions.* The model will be derived based on the fundamental differential equations of MMC operation and simplified into a 2×2 state-space form representing its DC dynamics. From this, a closed-form equation that provides an estimate of its settling time will be obtained.

- *Implementation of the model as a custom component in PSCAD/EMTDC and its validation against detailed simulations, including the integration of conventional MMC control schemes.* The model equations will be written as a black box program and interfaced with control systems developed in PSCAD/EMTDC. Once the simulation parameters are provided, the voltage and current output waveforms will be compared against those from PSCAD/EMTDC.

- *Investigation and analysis of MMC response speed under different component sizes and operating points.* Parametric studies will be conducted both using the model and in PSCAD/EMTDC with varying parameters, and the impacts on the response speed will be quantitatively compared and evaluated.

1.4 Thesis Organization

The remainder of this thesis is divided into four chapters as described below:

- **Chapter 2:** The operation, conventional and frequency support control schemes, as well as sizing methods for MMCs found in literature are reviewed.

- **Chapter 3:** The energy control scheme is developed and implemented. A parametric study is conducted to investigate the impact of different system parameters on the effectiveness of energy control in mitigating frequency excursions.

- **Chapter 4:** The closed-form equations of the mathematical model are developed and validated. A parametric study is conducted to investigate the impact of different system parameters on MMC operating with consideration of energy control requirements.

- **Chapter 5:** The contributions and conclusions of this thesis are summarized, and recommendations for future work are discussed.

Chapter 2

Literature Review

The material reviewed in this chapter lays the foundations for the research presented in the consequent chapters of this thesis. Fundamentals of MMC operation are first discussed, including conventional control systems. It is followed up by newer control schemes designed for frequency support. Capacitor sizing of the MMCs is also included.

2.1 MMC Fundamentals

2.1.1 Topology

The conventional three-phase MMC topology [18] is shown in Fig. 2.1 . As indicated, each phase (leg) consists of an upper and a lower arm. Each arm consists of N submodules (SMs) connected in series. These SMs are what enable the high modularity and scalability of the MMC. For example, higher power and voltage ratings can be achieved with the inclusion of more SMs, without any changes in the MMC topology or altering the individual SM ratings. The arm inductors are included to absorb any voltage mismatch in the DC loop of each

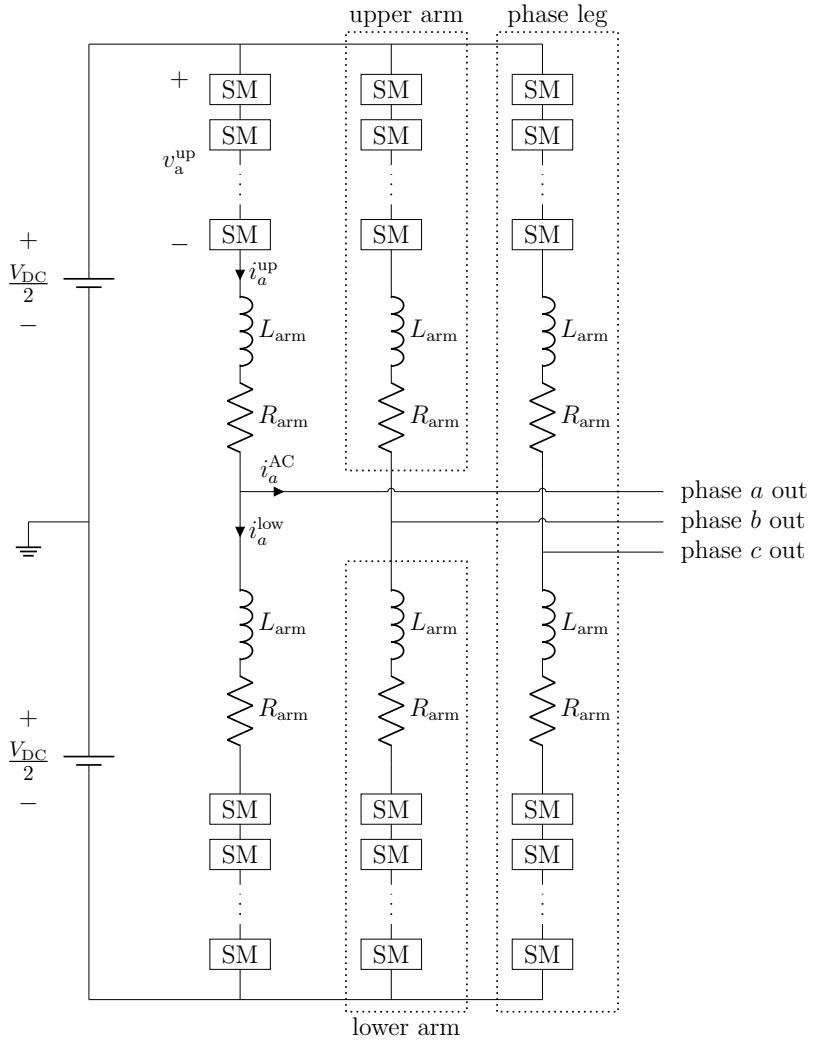

Fig. 2.1: Conventional three-phase MMC topology.

arm according to Kirchhoff's Voltage Law (KVL). They also have the additional benefit of suppressing higher order harmonics in the arm currents. An arm resistance is included to represent the switching and conduction losses within each arm.

The SMs in each arm are switched in or out according to a generated switching signal. Ideally, there are N SMs inserted and N SMs bypassed in each phase at each time instant

to satisfy KVL. This is assuming that the voltage of each SM is maintained at its nominal voltage given by

$$V_{\text{sm,nom}} = \frac{V_{\text{DC}}}{N}, \tag{2.1}$$

where V_{DC} is the DC-link voltage, typically from an external DC source. This property enables the MMC to operate as an $(N+1)$-level VSC. Further operating capabilities and details of the MMC depend on its SM topology/topologies and switching signals.

2.1.1.1 Submodules

The SM topology is a primary determinant of the MMC's operating capabilities. Various SM topologies have been investigated in the interest of expanding the MMC capabilities, such as the inclusion of more voltage levels for each SM, DC-side fault blocking, and the reduction of power losses. The most common SM topologies [18] are the half-bridge (HB) and full-bridge (FB) SMs, which are shown in Fig. 2.2.

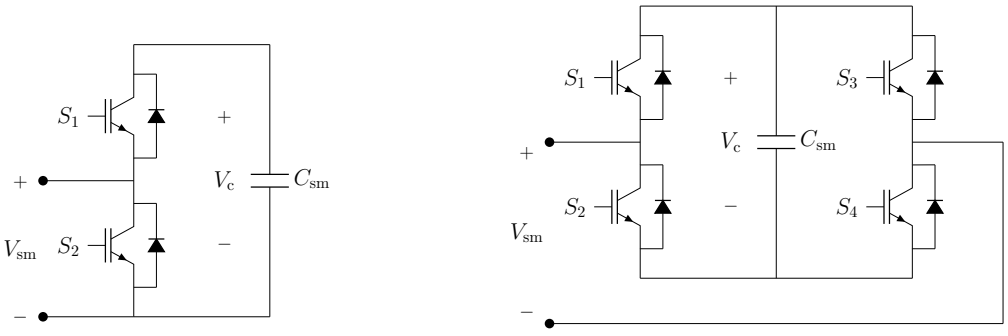

(a) Half-bridge submodule. **(b)** Full-bridge submodule.

Fig. 2.2: Conventional submodule topologies.

The FB SM is advantageous over the HB SM in aspects including its ability to output a negative voltage and DC-side fault blocking capability. However, as the FB SM also comes

at the additional cost of size and switching and conduction losses, the HB SM has been the more common of the two. This thesis will, therefore, consider the HB SM implementation of the conventional MMC.

During normal operation, the HB SM has four possible states based on the states of its two switches S_1 and S_2. These four states are shown in Fig. 2.3 and the corresponding switch configurations are summarized in Table 2.1.

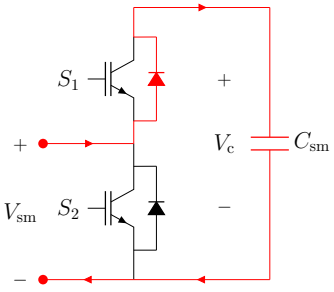

(a) Inserted; positive current.

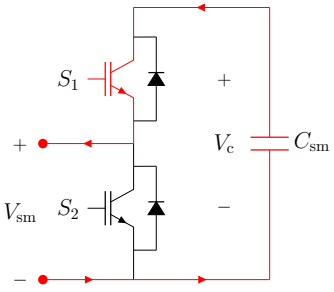

(b) Inserted; negative current.

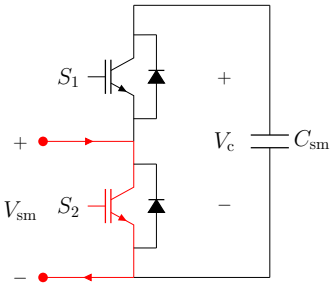

(c) Bypassed; positive current.

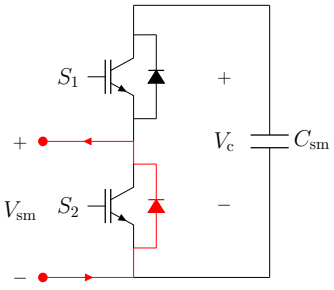

(d) Bypassed; negative current.

Fig. 2.3: Half-bridge submodule states.

When the HB SM is bypassed, it has no contribution to the arm voltage regardless of the current direction because the capacitor is not inserted. On the other hand, when the HB SM is inserted, it contributes a voltage of V_{sm} to the arm voltage. However, the capacitor

Table 2.1: Half-Bridge Submodule Switch Configurations

S_1	S_2	Inserted/Bypassed	V_{sm}	Current Direction
OFF	OFF	Inserted	V_c	Positive
ON	OFF	Inserted	V_c	Negative
OFF	ON	Bypassed	0	Positive
OFF	OFF	Bypassed	0	Negative

voltage, and therefore V_{sm}, will either decrease or increase based on the current direction, and at a rate based on the size of C_{sm}. The capacitor will be charging when the current is positive, so the SM voltage will be increasing. Vice versa, the capacitor will be discharging when the current is negative, so the SM voltage will be decreasing. The functionality of the MMC depends on maintaining these SM voltages near their nominal value. At the same time, only N SMs in each phase will be inserted at each time instant. One of the main roles of the converter's switching scheme is, therefore, to ensure that the SMs are inserted and bypassed such that their voltages are maintained near their nominal value.

2.1.2 Switching Signal Generation

The switching signals need to determine (i) how many and (ii) which SMs are inserted at each time instant. The former is determined by the modulation method, and the latter is determined according to the balancing method. Both of these are discussed in this section.

2.1.2.1 Modulation

The most common modulation methods for MMCs are classified as pulse-width modulation (PWM) based and nearest level control (NLC). The functionality of both types are reviewed.

2.1.2.2 Pulse-Width Modulation

PWM methods are based on continuously comparing a carrier (triangular) waveform against a (sinusoidal) reference waveform $m^{\text{ref}}(t)$. This technique has been conventionally used in 2-level VSCs and a sample is illustrated in Fig. 2.4. As shown, when $m^{\text{ref}}(t)$ is larger than

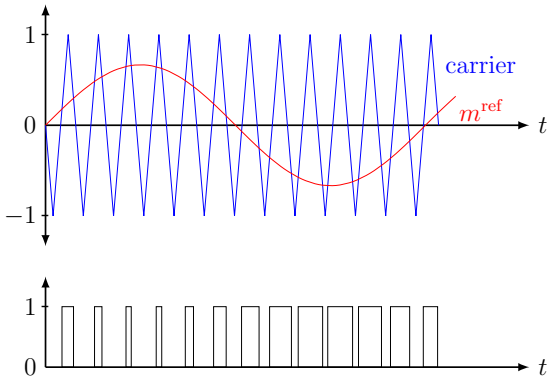

Fig. 2.4: Basis of PWM operation.

the carrier, an output signal of 1 is generated as shown in the lower graph. On the contrary, no signal is generated if $m^{\text{ref}}(t)$ is less than the carrier. The output signal is consequently a series of pulses with varying widths. These pulses dictate the configurations of the converter switches and, therefore, its operation at each instant of time. However, this strategy only applies to two SMs in a phase of an MMC: one SM in the upper arm and one SM in the lower arm. An extension is necessary in order to apply this concept in multi-SM MMC operation.

The most common class of PWM methods for MMCs is sub-classified as carrier-disposition PWM techniques (CD-PWM) [18]. Their basis is still on a comparison of a carrier and a reference waveform as above; however, instead of only having one carrier, there are N carriers in order to be able to account for all the N SMs in the MMC. Variations between these N carriers breaks CD-PWM into further subsets, but they will not be discussed in detail here.

PWM methods are typically used when there is a small number of SMs. This is mainly

because the switching occurs at a high frequency, so the associated losses become significant especially as the number of SMs increases. For an MMC with many SMs, a lower frequency modulation method is preferred.

2.1.2.3 Nearest Level Control

NLC is based on discretizing the reference waveform into levels that are integer multiples of the individual nominal SM voltage ($V_{\text{sm,nom}}$). Under normal operating conditions, each phase of the MMC is only able to provide an output that is a multiple of the SM voltage. This is due to the nature of its series-connected and balanced SMs. The discretization of the reference waveform, therefore, reflects the MMC output v^{out} more meaningfully. An example of discretizing an $m^{\text{ref}}(t)$ to v^{out} is illustrated in Fig. 2.5. Note that all values are per-unitized with respect to half of the DC-link voltage, $\frac{V_{\text{DC}}}{2}$. At each time instant, $m^{\text{ref}}(t)$

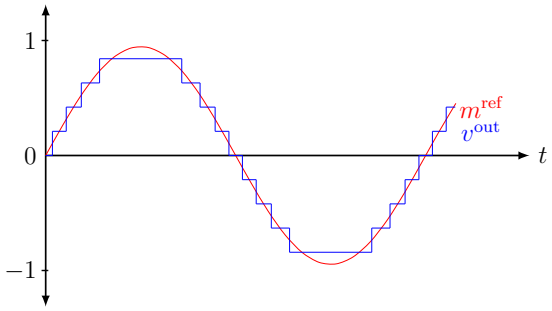

Fig. 2.5: Basis of NLC operation.

is rounded to the nearest available level. It is noted that not all of the possible levels may be used depending on $m^{\text{ref}}(t)$. In practice, there are reference waveforms for the upper and lower arms separately and the per-unitized representation explicitly determines the number of SMs that will be inserted in each arm at each instant in time. As shown, the resolution is $V_{\text{sm,nom}}$ and as per (2.1), there are $N+1$ possible levels for a range of 0 to $\frac{V_{\text{DC}}}{2}$.

The resolution is evidently dependent on N. A coarse resolution means that the discretization does not closely resemble the reference waveform, introducing significant low order harmonics, which may not be easily filtered out. NLC is therefore more practical when there are a large number of SMs. Further, its low frequency switching behaviour helps to minimize the switching losses. This is the method that will be used in this thesis.

2.1.2.4 Sorting and Balancing

The MMC functionality as described so far requires the SM voltages to be balanced and maintained close to their nominal values. When the SM is bypassed, it will not experience any voltage changes. However, when a SM is inserted, the capacitor voltage will charge or discharge depending on the current direction. This will deviate the SM voltage. Taking note that the arm currents are AC and will therefore be positive or negative at different time instances, it is possible to keep the SM voltages balanced.

When the current direction is positive, inserted SM capacitors will be charged. Only N of the $2N$ SMs in each phase are inserted at each time instant. Therefore the SMs with the lowest capacitor voltages must be inserted in order to minimize the imbalance [27]. On the other hand, when the current direction is negative, inserted SM capacitors will discharge. Therefore the highest capacitor voltages should be inserted. In order to determine the highest/lowest capacitor voltages, all the SM voltages must be measured and then sorted using a sorting algorithm. Efficient sorting algorithms would be necessary in order to not compromise the speed, especially with more SMs.

A simple sort and balance scheme has been shown to be able to keep the SM voltages well-balanced. This is the method that is used in this thesis. Further balancing schemes are not discussed further. The main point is that the SM voltages are maintained balanced

during operation; this assumption will be taken in the consequent work.

2.2 Conventional Control Methods

2.2.1 Direct Control

Direct control methods make use of the relationship between the AC- and DC-side voltages of the MMC that exists under ideal conditions via the modulation index m

$$V_{\mathrm{AC}} = m\frac{V_{\mathrm{DC}}}{2}, \tag{2.2}$$

where V_{AC} is the amplitude of the phase voltage, and V_{DC} is the DC-side voltage. This relationship neglects variations in the DC-side voltage and any losses within the converter (e.g., across the arm inductor and resistor). The modulation index is therefore a control variable for the AC voltage.

An MMC may be connected to an AC system in the view of an equivalent circuit as shown in Fig. 2.6. In this case, the active and reactive power transfers from the MMC to the

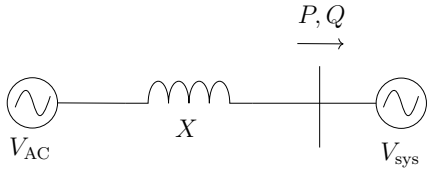

Fig. 2.6: Equivalent circuit of MMC connected to an AC system.

AC system are given by

$$P = \frac{V_{\mathrm{AC}}V_{\mathrm{sys}}}{X}\sin\delta \tag{2.3a}$$

$$Q = \frac{V_{\mathrm{AC}}V_{\mathrm{sys}}\cos\delta - V_{\mathrm{sys}}^2}{X}, \tag{2.3b}$$

where V_{sys} is the system voltage and X is the line reactance. The line resistance is neglected under the assumption that it is negligibly small compared to the reactance, which is typically the case in the interest of low-loss power transfer. From (2.3), it is evident that the two variables are V_{AC} and δ, since V_{sys} is usually a predetermined value. Furthermore, from (2.2), the value of V_{AC} is controlled by m. In other words, m and δ are the control variables and their usage depends on what type of bus the MMC is connected to at the point of common coupling (PCC). For a power-voltage (PV) bus, the real power and voltage must be maintained. For an active-reactive power (PQ) bus, the active power and reactive power must be maintained. The two respective quantities may be held close to their set reference points by the use of properly tuned PI controllers as shown in Fig. 2.7. The relatively

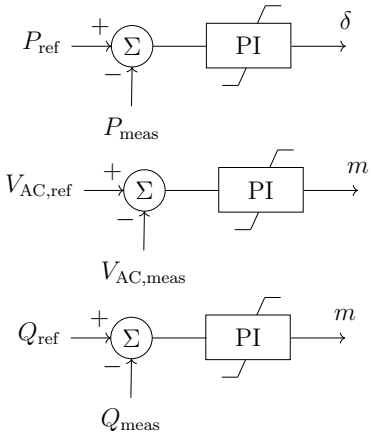

Fig. 2.7: Controllers used for PV/PQ control.

greater sensitivities of δ on P than Q, as well as m on V_{AC} or Q than P, are what dictate the illustrated implementations. However, it must be noted that the tuning of PI controllers may not be completely straightforward, because there is still coupling between the quantities to control. This can be addressed by a decoupled control scheme.

2.2.2 Decoupled Control

The basis for the decoupled control scheme is presented in this subsection. From the active and reactive powers, which are expressed as

$$P = v_{\text{sys},a} i_{\text{AC},a} + v_{\text{sys},b} i_{\text{AC},b} + v_{\text{sys},c} i_{\text{AC},c} \tag{2.4a}$$

$$Q = v_{\text{sys},bc} i_{\text{AC},a} + v_{\text{sys},ca} i_{\text{AC},b} + v_{\text{sys},ab} i_{\text{AC},c} \tag{2.4b}$$

in the *abc* domain, may be transformed to *dq*0 domain using Park's transformation as

$$P = \frac{3}{2}(V_{\text{sys},d} I_{\text{AC},d} + V_{\text{sys},q} I_{\text{AC},q}) + V_{\text{sys},0} I_{\text{AC},0} \tag{2.5a}$$

$$Q = \frac{3}{2}(V_{\text{sys},d} I_{\text{AC},q} - V_{\text{sys},q} I_{\text{AC},d}), \tag{2.5b}$$

here $V_{\text{sys},d}$, $V_{\text{sys},q}$, $V_{\text{sys},0}$ and $I_{\text{AC},d}$, $I_{\text{AC},q}$, $I_{\text{AC},0}$ are the d, q, and 0 components of the voltage and current respectively. Applying KVL along the path from the DC- to AC-side of the MMC yields

$$v_{\text{AC}} = v_{\text{sys}} + \left(\frac{R_{\text{arm}}}{2} + R_{\text{AC}}\right) i_{\text{AC}} + \left(\frac{L_{\text{arm}}}{2} + L_{\text{AC}}\right) \frac{\mathrm{d}i_{\text{AC}}}{\mathrm{d}t} \tag{2.6}$$

in the *abc* domain, which may also be transformed to the *dq*0 frame as

$$\begin{aligned} V_{\text{AC},dq0} = V_{\text{sys},dq0} + \left(\frac{R_{\text{arm}}}{2} + R_{\text{AC}}\right) I_{\text{AC},dq0} + \left(\frac{L_{\text{arm}}}{2} + L_{\text{AC}}\right) \frac{\mathrm{d}I_{\text{AC},dq0}}{\mathrm{d}t} \\ + \left(\frac{L_{\text{arm}}}{2} + L_{\text{AC}}\right) \omega \begin{bmatrix} 0 & 1 & 0 \\ -1 & 0 & 0 \\ 0 & 0 & 0 \end{bmatrix} I_{\text{AC},dq0}. \end{aligned} \tag{2.7}$$

By implementing two controllers to control, for example, the P and V_{sys} in the case of a PV bus, the d and q components of the current may be obtained and used in conjunction to compute and control the converter voltage. An example (neglecting the resistances because they are typically small compared to the impedance) is shown in Fig. 2.8. One benefit of

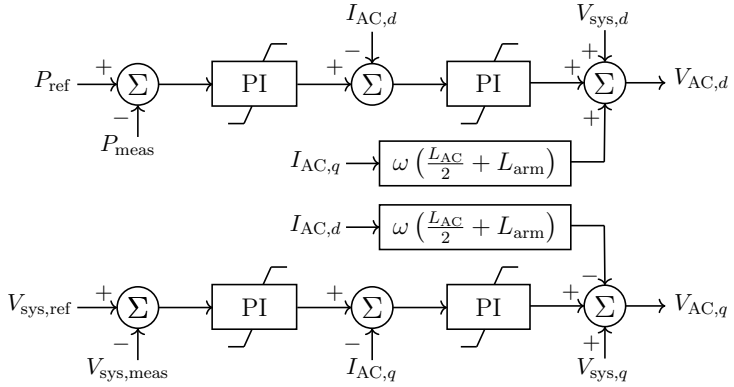

Fig. 2.8: Controllers used for decoupled AC active power and AC voltage control.

decoupled control which must be emphasized is that the converter current can be limited as enforced by the left-most PI controllers.

2.2.3 Circulating Current Suppression Control

A circulating current suppression control (CCSC) scheme is implemented to minimize the circulating currents in the MMC in [28]. The fundamentals of this scheme are reiterated here for convenience of the reader. The circulating current through phase j is expressed as

$$i_j^{\text{circ}} = \frac{i_j^{\text{up}} + i_j^{\text{low}}}{2}. \tag{2.8}$$

Assuming symmetric operation, the circulating current will only contain the DC and even-order harmonic components. Furthermore, only the components up to the second harmonic

are typically considered because it is the most prominent harmonic, and higher order harmonics are relatively small [15–17]. Therefore the circulating currents for each phase $j = a, b, c$ are expressed as

$$i_a^{\text{circ}} = \frac{I_{\text{DC}}}{3} + I_2 \sin(2\omega t + \varphi), \tag{2.9a}$$

$$i_b^{\text{circ}} = \frac{I_{\text{DC}}}{3} + I_2 \sin(2\omega(t - \frac{2\pi}{3}) + \varphi) = \frac{I_{\text{DC}}}{3} + I_2 \sin(2\omega t + \varphi + \frac{2\pi}{3}), \tag{2.9b}$$

$$i_c^{\text{circ}} = \frac{I_{\text{DC}}}{3} + I_2 \sin(2\omega(t + \frac{2\pi}{3}) + \varphi) = \frac{I_{\text{DC}}}{3} + I_2 \sin(2\omega t + \varphi - \frac{2\pi}{3}), \tag{2.9c}$$

where φ is the initial phase angle. It is indicated in (2.9) that the second-order harmonic is inherently in negative sequence. Additionally, applying KVL along the DC loop of the MMC yields

$$V_{\text{DC}} = v^{\text{up}} + 2L_{\text{arm}} \frac{\mathrm{d}}{\mathrm{d}t} i^{\text{circ}} + 2R_{\text{arm}} i^{\text{circ}} + v^{\text{low}}, \tag{2.10}$$

which may be rearranged to

$$\Big(L_{\text{arm}} \frac{\mathrm{d}}{\mathrm{d}t} + R_{\text{arm}}\Big) i^{\text{circ}} = \frac{1}{2}\Big(V_{\text{DC}} - \big(v^{\text{up}} + v^{\text{low}}\big)\Big). \tag{2.11}$$

The right-hand-side of (2.11), which will be used to control the circulating current, is denoted as

$$v_j = \frac{1}{2}\Big(V_{\text{DC}} - (v^{\text{up}} + v^{\text{low}})\Big) \tag{2.12}$$

for each phase j, and upon substitution of (2.9), is converted to the $dq0$ domain as

$$\begin{bmatrix} V_d \\ V_q \end{bmatrix} = L_{\text{arm}} \frac{\mathrm{d}}{\mathrm{d}t} \begin{bmatrix} I_d^{\text{circ}} \\ I_q^{\text{circ}} \end{bmatrix} + R_{\text{arm}} \begin{bmatrix} I_d^{\text{circ}} \\ I_q^{\text{circ}} \end{bmatrix} + \begin{bmatrix} 0 & -2\omega L_{\text{arm}} \\ 2\omega L_{\text{arm}} & 0 \end{bmatrix} \begin{bmatrix} I_d^{\text{circ}} \\ I_q^{\text{circ}} \end{bmatrix} \tag{2.13}$$

which is the basis of the CCSC scheme. It is noted that the 0 component has been neglected since it is zero due to the balanced three-phase system assumption. Similar to the decoupled control scheme, with I_d^{circ} and I_q^{circ} as the inputs and V_d and V_q as the outputs, the explicitly linear relationships can be implemented as they are, and PI controllers can be tuned to implement the non-linear terms of this control scheme. The outputs are second harmonic terms that are injected into the modulation reference waveform to manifest the effect of suppressed circulating currents.

2.2.4 Phase-Locked Loop

The MMC must be properly synchronized to the grid in order for its control schemes to fulfill their intended functionalities. Synchronization may be attained using a phase-locked loop (PLL) at the PCC in order to obtain a reference phase angle θ_{PLL}. The mathematical basis of a PLL is to bring

$$v_{\text{sys}} \sin(\omega t - \theta_{\text{PLL}}) = v_{\text{sys}} \sin(\omega t) \cos\theta_{\text{PLL}} - v_{\text{sys}} \cos(\omega t) \sin\theta_{\text{PLL}} \tag{2.14}$$

to zero at all times using θ_{PLL}. The PLL has successfully locked onto the grid voltage when this becomes true. A closed-loop control system can be implemented to enforce this control as shown in Fig. 2.9.

2.3 Frequency Support Methods

The capability of frequency support by MMCs is achieved by the use of control schemes and its inherently stored electrostatic energy. These are broadly based on the control of

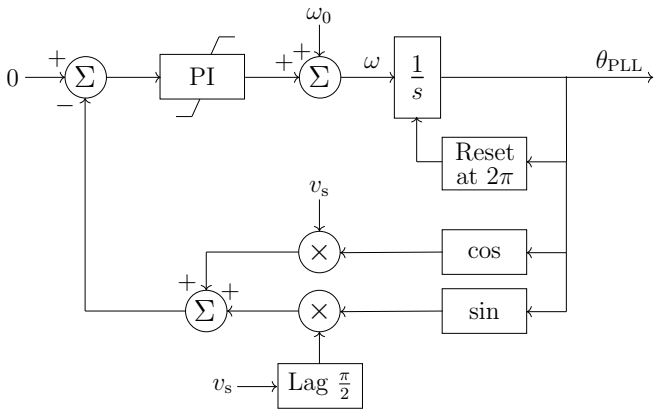

Fig. 2.9: Block diagram for phase-locked loop.

the MMC's internal energy to provide (or absorb) the necessary amount of power during a disturbance in order to minimize the frequency deviation. This controlled provision helps maintain the frequency near its nominal value in spite of the system having low inherent inertia. This response must be sufficiently fast in order to provide proper primary frequency support. The implementations in literature can be categorized into mainly two strategies: (i) emulation of the behaviour of an SG, and (ii) explicit maintenance of power balance.

2.3.1 Inertia Emulation Approach

A subset of frequency control implementations are based on the idea of controlling the converter such that it operates analogously to an SG. The intention is to emulate the mechanical inertia of the SG. The energy stored in the capacitors of the converter is deployed in a manner similar to the energy stored in the rotating masses of conventional SGs. These methods have been classified as inertia emulation control, which have also been referred as virtual/synthetic inertia [29]. Their key characteristic is their emulation of an SG; that their output power is directly proportional to the rate of change of frequency (ROCOF).

This way of operating the converter has been investigated in the virtual synchronous

machine (initially abbreviated VISMA [30] and then VSM in later works [31,32]). Controllers to accurately track the voltage at the PCC with the grid are required. In [33], synchronverters, which are inverters mimicing the operation of SGs, are introduced. Their concept is based on VISMA, but is not dependent on the tracking of the reference currents or voltages. This strategy has been implemented in an MMC in [34]. The emulation of SG behaviour is based on the swing equation, which is used to govern the control system [31–39]. The measurements are compared to a reference and processed through a series of controllers. These signals modify the reference waveform to change the operating point of the MMC.

A drawback to this swing equation-based control scheme is the dependency on the ROCOF measurement, which is sensitive to noise and may, therefore, compromise the intended functionality. Frequency control schemes that are not explicitly based on the swing equation have also been studied in literature.

2.3.2 Energy Control Approach

Another general frequency control approach uses energy-based control schemes to directly maintain power balance. Unlike inertia emulation control, the swing equation dependency is not necessarily explicit. This approach typically makes use of capacitors because they are most promising for inertia enhancement based on response speed and low cost, and include minimal hardware adjustments [40]. The property of a fast response speed is particularly important because the intention is to provide primary frequency support.

In [41], the MMC circulating currents are controlled to drive the MMC beyond its normal maximum power limits. The MMC is operated in overload for a few seconds to provide the additional power needed, effectively carrying out a primary frequency control. The thermal limits of the IGBTs of the MMC SMs were considered because of the overload conditions. It

was observed that sufficient support was provided by the MMC in overload in approximately five seconds with small temperature margins (~5°C). However, this approach requires oversizing the converter, which may not always be feasible.

In [42] it is observed that the energy stored in the MMC's SM capacitors for providing frequency support is significantly less than the contribution from the SGs. It is speculated, however, that the contribution of the energy stored in the MMC would be more significant in weak AC grids. Related studies continued despite the observed level of contribution from the MMC, because the implementation of more RESs would weaken the existing AC grid.

The MMC characteristic that the energy stored is not directly connected to the DC-link is used to an advantage in [43]. The capacitance seen by the DC-link is increased because of the inclusion of the capacitance from the MMC SMs, resulting in less DC voltage variations. The amount of DC voltage variation was also seen to be dependent on the tracking of the DC voltage by the controllers. The energy-based control scheme indicated an additional degree of freedom not otherwise available in a non-energy-based control scheme [28, 44]. This is because in the non-energy based control scheme, the energy and DC voltage are not separated. Another similar technique where the capacitance seen by the DC-link is varied to regulate the power balance is used to improve DC voltage quality in [45], and to improve the stability in MMC-HVDC systems with large DC reactors in [46]. An energy-based control strategy is used to calculate the required capacitance of the MMC, and the corresponding number of SMs that are inserted at each time instant. It is also noted that this technique does not affect the AC-side dynamics. Control schemes that also use the MMC's internally stored energy are implemented in [47] and [48]. In both, the limits on the energy that can be supplied from the MMC are based upon the SM capacitor voltages.

It is evident that the requirement of maintaining the SM capacitor voltages near their

nominal values is the limiting factor in the available energy that can be used for frequency support. However, an MMC may contain redundant SMs as a backup in case an SM fails during operation [49]. The voltage stress on the individual SMs is also relaxed with the increase in the total number of SMs. This comes at the cost of more SMs and an increase in switching and conduction losses. Nevertheless, the additional energy from the redundant SMs expands the capability for energy exchange of the MMC in the interest of frequency support. In [50, 51], the redundant SMs are used to provide more energy or absorb excess energy as required. The above schemes take a common assumption that the energy stored in each arm is evenly distributed among all of the SM capacitors in the arm. This is a consequence of assuming that a balancing method [27] is deployed with the MMC operation. The balanced nature of the SMs is a basis of the MMC operation because of the modularity [13].

It is also important to note that the SM capacitor has a key contribution to the energy exchange capacity of the MMC. For energy-based control strategies, the tracking of the energy is essential to proper performance. The work in [45, 46, 52] particularly places such emphasis. There is the requirement that the energy controller is sufficiently faster than the DC voltage dynamics. Otherwise, this assumption made in the control strategy is no longer valid, and the DC voltage variations from the energy exchange of the MMC capacitors may be compromised. An example of meeting this requirement is given in [45] for having its energy controller response speed as 30 ms if the DC voltage controller response speed is 100 ms. It is also noted that with smaller SM capacitances, the response speed of the energy controller must be faster because there would be more variation in the DC voltage dynamics.

In [53], the response delay, ramp up rate, and capacity of the energy control were investigated. However, the duration of the energy control was not limited. One of the conclusions made was that the ramp up rate was the most important factor in achieving an effective

energy control, and a large capacity was only effective if the ramp up rate was sufficient. The amount of energy is dependent on the total energy storage capacity of the MMC, which is dominantly sized based on its SM capacitances. At the same time, as the RES penetration level increases, this energy storage also increases with the connection of more MMCs. This may limit the required energy storage of a single MMC. The inherent property of energy storage elements also means that with higher capacitances, the ramp up rate may slow down.

As observed in the literature above, there is an evident relationship between the DC voltage dynamics, the available internal energy, and SM capacitor voltage of the MMC, which define the required response speed of the frequency control support scheme. Accordingly, the size of the SM capacitors of the MMC should also have a significant contribution [52, 54–62].

2.4 Capacitor Sizing Methods

The optimal sizing of the MMC SM capacitors is important for proper performance and minimization of cost and size. A lower limit for the SM capacitance considering only voltage limits is provided in [55]. In [56, 57], an energy-based analysis is conducted and an analytic expression for the minimum SM capacitance is derived based on the maximum allowable energy and capacitor voltage deviations. A graphical analysis of the range of the capacitor voltages, the number of SMs, and power of the MMC is presented in [58]. The analyses in [59–61] also conclude that the SM capacitance is the main factor contributing to the SM capacitor voltage ripple reduction. While none of these studies included schemes for frequency support, it is consistently evident that the SM capacitor voltage ripple and available energy of the MMC are dependent on the SM capacitance. In [52], an analytic expression is derived based on its specific control scheme to calculate the required equivalent capacitance for an

MMC operating with energy exchange for frequency support at a given time instant. The capacitor was sized to limit the voltage deviation within a specified range (5%).

Since the response speed of a control scheme has been shown to be dependent on a variety of factors, the implications of the SM capacitance on the MMC operation beyond the SM capacitor voltage ripple must be considered. In [63], the Floquet-Lyapunov Theorem was applied to linearize the dynamic state equations of the MMC. Around an initial operating point, the eigenvalues were obtained for different cases of component sizes as a means of iterative design. The eigenvalues were used to observe the damping of transients. In [64], an analytic expression for a time constant related to the time required for the upper and lower arms of the MMC to become balanced again after an unbalanced disturbance is derived. Natural operation was considered and the SM capacitance is seen to have an effect on the time constant. With larger capacitance, this time became longer, which is undesirable. However, the time for the voltages to become balanced again is not necessarily the only condition to determine if the MMC has settled to a new operating point, and therefore may not provide full information about the response speed of the MMC upon a disturbance.

2.5 Summary

Unlike SGs, RESs do not inherently possess inertia to provide primary frequency support during power imbalances. Consequently, the overall inertia of the system decreases as the proportion of RESs in the network continues to increase. To resolve this, the enabling of frequency support by MMCs is being studied.

This capability is realized using control schemes that make use of the internally stored energy from the SM capacitors of the MMC. However, the controllers are typically restricted

to meet a specified response speed in order for the control scheme to function as intended. The challenge arises from the fact that the required response speed is dependent on the MMC operation and its parameters. At the same time, the components of the MMCs are typically desired to be minimally sized in the interest of both cost and space.

Previous studies have shown the frequency control schemes being limited by the SM capacitances. Although the limitation may be alleviated with larger capacitances, in addition to the increased cost and space, increasing the capacitance slows down the response time of the MMC. For energy control, the response speed must be fast in order to emulate the primary frequency response. It is therefore necessary to understand the trade-offs between the SM capacitance and MMC response time to disturbances.

Chapter 3

Control of the Energy Stored in MMCs

An MMC inherently stores energy within its SM capacitors. This energy level is conventionally maintained at the nominal value, because the SMs are kept at their nominal voltage using a sorting and balancing control scheme. The capacitor voltage ripple and energy stored in the arm inductors are typically negligible, so the nominal energy level is given by

$$E_{\mathrm{MMC}} = 6 \times N \times \frac{1}{2} C_{\mathrm{sm}} V_{\mathrm{sm,nom}}^2, \tag{3.1}$$

which is the sum of the energy stored in all of the SMs in each arm (N) of the MMC. This expression shows that the energy stored in the MMC can be dynamically changed through the voltage of the SM capacitors. While this energy is not conventionally changed, it is possible to do so and its effects are investigated in this chapter.

3.1 Concepts and Implementation of Energy Control

When a perturbation disturbs the power balance between electrical generation and demand in the power system, frequency deviations occur as per the swing equation [1]. As power is a change in energy over time, i.e.,

$$P_{\mathrm{MMC}} = \frac{\Delta E_{\mathrm{MMC}}}{\Delta t}, \tag{3.2}$$

where

$$\Delta E_{\mathrm{MMC}} = 6 \times N \times \frac{1}{2} C_{\mathrm{sm}} \left(V_{\mathrm{sm}}^2 - V_{\mathrm{sm,nom}}^2 \right) \tag{3.3}$$

is the difference in energy from nominal, the energy stored in the MMC can be used to compensate, at least in part, such power imbalances. For example, if there is a shortage of power, some energy may be released from the MMC SMs to provide additional power. Similarly, if there is an excess of power, some energy may be absorbed by the SMs. The intended merit of dynamically controlling the energy stored in an MMC is to minimize this power imbalance, so that the effective power imbalance seen by the SGs, and therefore the frequency deviations, will be less drastic.

A control system must be implemented to vary the energy stored in an MMC, as this is not an inherent feature. This is done by augmenting the conventional control system with an energy controller as shown in Fig. 3.1. The conventional PQ and CCSC schemes are present and implemented as usual, except the zero-sequence component of the generated modulation signals from CCSC that is conventionally unused is now controlled by the energy controller. The energy controller is responsible for controlling the energy stored in the MMC at any instant of time through the average value of the SM voltages. This enables controlled changes

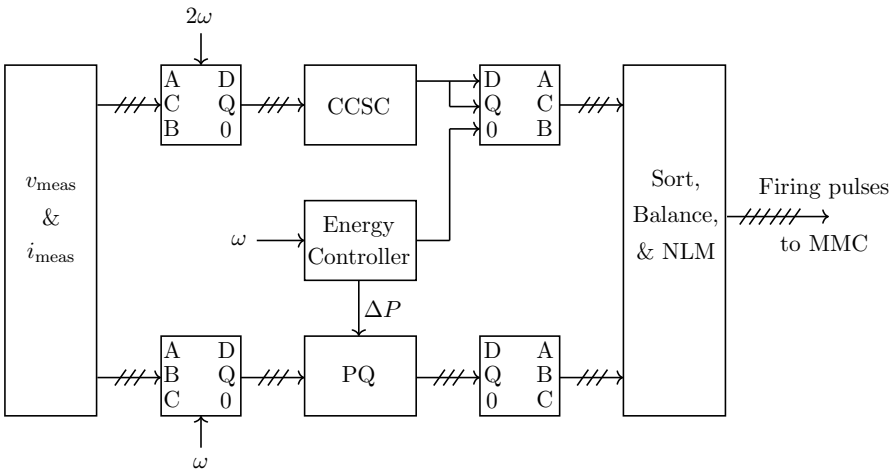

Fig. 3.1: Energy controller integrated with conventional control schemes.

in energy and, therefore, release or absorption of power as per (3.2). The increase (or decrease) in the expected power output of the MMC (ΔP) is input to the PQ control to adjust the power reference. It should also be noted that each SM will still have approximately the same average voltage as enforced by the sorting and balancing scheme. However, the value of the average voltage will be slightly higher or lower than the nominal value based on whether energy control has been used to discharge or further charge the SM capacitors.

In Fig. 3.2, the implementation details for the energy controller are presented. As shown,

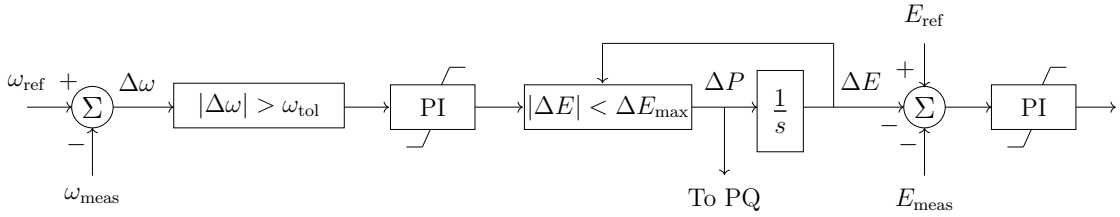

Fig. 3.2: Energy controller scheme to vary the energy stored in an MMC.

the power imbalance that the energy controller should try to compensate for is defined by the frequency deviation. This is because in the power system, the frequency is defined by the

speed of the rotating shafts of the SGs. This frequency is the value that must be maintained and varies according to power imbalances as per the swing equation. By compensating the power imbalances, the frequency deviations can be minimized. If the frequency is within the accepted tolerance, as might be defined by grid codes, there is no need to trigger the energy control as enforced by the first logic block. But if the frequency has deviated outside of the tolerated bounds, then the mapping from frequency to power is realized by the PI controller. This power compensation signal output from the PI controller would ideally be used immediately, but the limitation on the amount of energy deviation the MMC can tolerate places a second logic condition. The maximum energy deviation $\Delta E_{\max}$ may be defined by the tolerance that the average voltage of the SM must remain within (e.g., $\pm 5\%$); otherwise, the operation of an MMC may be compromised. The amount of energy that can be used for power compensation given by (3.3) is, therefore, limited by this tolerance. The instantaneous energy deviation required for power compensation ΔE is obtained from the integration of the power compensation ΔP signal and constantly checked. If there is already too much energy deviation, ΔP is zero as forced by the logic condition, so that ΔE cannot deviate further. The ΔP signal is sent to modify the power reference in PQ control. The ΔE signal is compared with E_{ref}, which represents the nominal energy stored in the MMC given by (3.1) and E_{meas}, which is the measured energy stored in the MMC given by

$$E_{\text{meas}} = 6 \times N \times \frac{1}{2} C_{\text{sm}} V_{\text{sm}}^2, \tag{3.4}$$

so that the signal sent through the PI controller to the zero-sequence component along with the signals from CCSC represents the required energy deviation that has taken the error between the expected and measured energy values into account.

An example of using energy control is now conceptually demonstrated. The frequency, SM voltage, and power, responses will be observed. A sample frequency response upon a load increase perturbation is illustrated in Fig. 3.3. The dashed line is when energy control is not used, and the solid line is when energy control is used. For frequency, the properties of interest are t_{nadir} and f_{nadir}. The time t_{nadir} is defined as the time between the instant of perturbation and the time at which the frequency nadir f_{nadir} is reached. This is because the former defines the maximum frequency deviation, and the latter defines the ROCOF. As indicated, at $t = 20$ s, the system is subjected to a perturbation. Correspondingly, the frequency begins to drop and at around $t = 21$ s the frequency deviates beyond the tolerated deviation of 0.2 Hz. At this point, the energy controller is triggered and its effect is shown by the increase in frequency, heading back to the nominal 60 Hz value. It does not last indefinitely, however, because soon after, the frequency begins to drop again as the energy control has terminated. Despite this brief momentary action, it can be seen that the frequency nadir is less deviated from nominal when energy control is used. Additionally, it takes a longer time after the perturbation to reach the frequency nadir. These beneficial effects are not manifested without energy control. With energy control, the SGs do not need to change their operating point as rapidly or as much, which results in less frequency excursions as expected.

The action of energy control can also be seen through the discharge of SM voltages in Fig. 3.4. The dashed line is when energy control is not used, and the solid line is when energy is used. As previously stated, the perturbation occurs at $t = 20$ s and energy control is triggered around $t = 21$ s. The solid line consistently illustrates the capacitor voltage discharge starting around $t = 21$ s. The discharge terminates shortly after, when the capacitor voltage has deviated close to 5% from its nominal value since this was the set tolerance. The

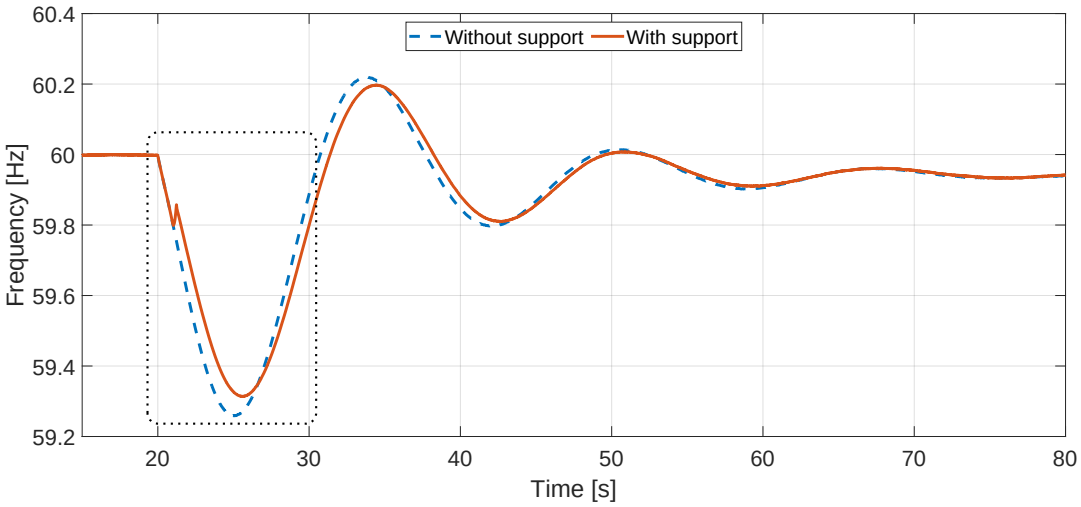

(a)

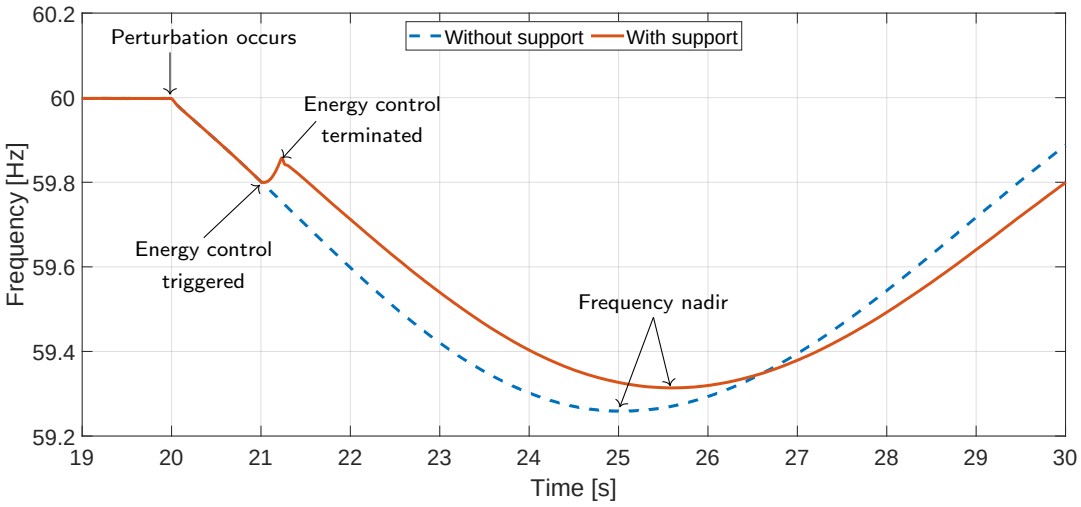

(b)

Fig. 3.3: Example frequency response with and without energy control; (b) is a zoom in of (a) on the dotted boxed region.

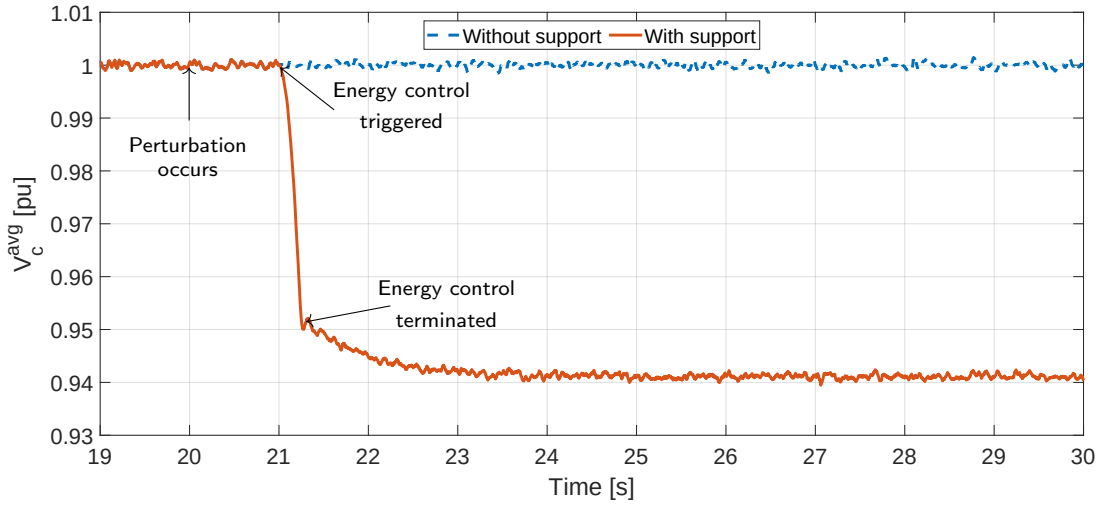

Fig. 3.4: Example capacitor voltage response with and without energy control.

small difference in the settling voltage in this example may be attributed to the measurement delay of the average SM voltage. Due to SM voltage ripple, this difference is reasonably small and does not significantly impact the capabilities of energy control. On the other hand, the dashed line does not show any voltage deviation as per the conventional control of an MMC.

The discharge of the SM capacitors is manifested as a power compensation. In Fig. 3.5, the power responses of the MMC and SG are compared when energy control is and is not implemented. As before, the dashed and solid lines indicate whether energy control is used. P_{AC}, P_{DC}, P_{MMC}, and P_{SG} are the AC- and DC-side powers of the MMC, the power from the SM capacitors resulting to energy control, and the power from the SGs respectively. Without energy control, the SG takes on the full perturbation. The SM capacitors do not provide any additional power, and the AC and the DC powers of the MMC remain the same because they do not contribute to the perturbation. This is because the references set by the conventional control schemes remain fixed. However, with energy control, once the frequency has deviated outside accepted levels, the SMs provide the excess power, which is reflected in

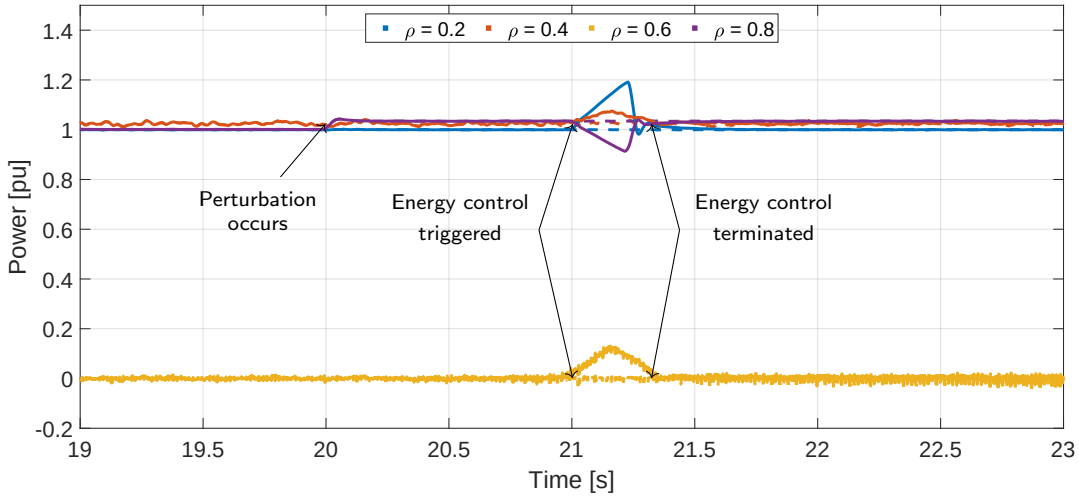

Fig. 3.5: Example power responses with (solid lines) and without (dashed lines) energy control.

the overall increase in the AC side of the MMC. In other words, the AC power of the MMC increases without increases in the DC power. This is important because the DC-side of the MMC is where the RESs are connected, and they may not be able to sustain large power perturbations. Their output demand should be kept relatively constant. It is also important to note that energy control is not limited to load increases. For example, in the case of a load decrease, the reverse is true in which the SMs absorb power.

In the provided example, it has become evident that there may be merit in implementing energy control in MMCs. The energy storage capacity of the MMC is a particularly important design parameter. The number of SMs in the initial MMC design is determined by the DC-side voltage and individual capacitor ratings. This means that in order to increase the energy storage capacity of an MMC and, therefore the amount of usable energy, the SM capacitance C_{sm} should be the factor that is increased. Furthermore, in low system penetration levels, the contribution of power from SGs dominates the response compared to the contribution from the MMC. However, it is expected that more RESs will be integrated into the power

system. This means that the penetration levels are expected to rise. As a result, there may be more MMCs in the system, and therefore a larger amount of usable energy. A simulation case study is conducted to investigate the relationships between the MMC energy storage, system penetration level and inertia, as well as the frequency response.

3.2 Test System

A simulation case in PSCAD/EMTDC is designed and set up in order to study the relationships between different energy storage capacities, system penetration levels, machine inertia, system perturbations, and their impact on the level of improvement in the frequency response due to energy control. The test system is illustrated in Fig. 3.6. The parameters for each

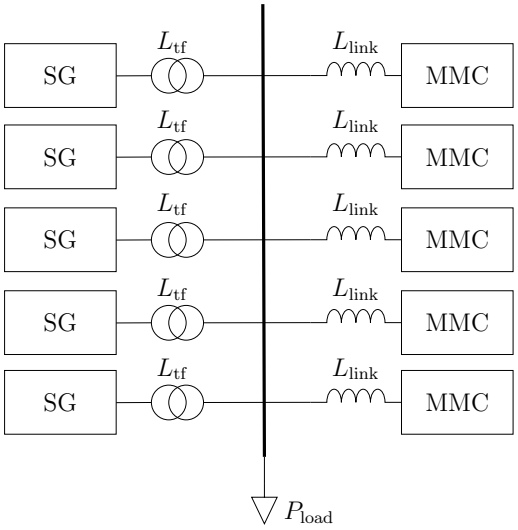

Fig. 3.6: Test system for MMC with energy control connected with SGs.

unit are outlined in Table 3.1 and 3.2, respectively. Note that the number of SMs (N), SM capacitance (C_{sm}), arm inductance (L_{arm}), and AC-side inductance (L_{link}) are not specified in Table 3.2. This is because different MMC designs are tested and these parameters are

Table 3.1: Synchronous Generator Parameters

Parameter	**Value**
Rated capacity S	200 [MVA]
Output power P_{SG}	150 [MW]
Fundamental frequency f_0	60 [Hz]
Inertia constant H	4 [s]
Transformer inductance L_{tf}	6%
Transformer winding	20 [kV] : 110 [kV]
Power-frequency droop R_{droop}	4%

Table 3.2: MMC Parameters

Parameter	**Value**
Output power P_{AC}	150 [MW]
Rated DC voltage V_{DC}	200 [kV]
Arm resistance R_{arm}	1 [Ω]

specified in their respective sections.

The SGs and MMCs are connected to a frequency independent constant power load. The frequency dependence is not included for simplicity to allow the study to focus on the aforementioned parameters and their relationships. This is acceptable since the perturbations that are applied in the study are load increases, in which the system has a frequency drop, so the case being considered is stricter.

It is first noted that in order to test different system penetration levels, the power contribution from the SGs and the MMCs must be varied, since the penetration level ρ of this test system is given by

$$\rho = \frac{\text{Total power from MMCs}}{\text{Total load power}}. \tag{3.5}$$

However, this is not feasible by simply considering a single SG and MMC, because there would be too much deviation from their rated operating points. This would compromise their operation and, therefore, the acquired results. Consequently, both the SG and MMC are equivalently represented by smaller, identical units connected in parallel. This way, the total contribution from SGs and MMCs can vary over a wide range without any individual unit deviating too far from its rated operating point. The penetration level is varied based on how many of each unit is connected to the constant power load. For example, to generate a system with a penetration level of 60%, two of the SGs and three of the MMCs are connected. Similarly, for a penetration level of 80%, one SG and four MMCs are connected.

The MMC has the conventional PQ and circulating current controls implemented, as well as the energy control and sorting and balancing schemes. It is assumed that the DC-side voltage of the converter is kept constant. Energy control is not activated unless the frequency exceeds the tolerance bounds of ± 0.2 Hz, and is terminated when the SM voltages deviate more than 5% from their nominal value. The former is because it is not necessary to change the frequency response when it is still within an acceptable range from the nominal value, and the latter is to ensure that the fundamental operation of the MMC is maintained.

It is noted that energy control may show greater improvements in the inertial response if it is allowed to be triggered sooner, because it would mean a faster response and therefore emulate the primary frequency response more closely. However, from a practical perspective, energy control cannot be triggered at the instant of perturbation, because such events are typically not known exactly beforehand. Furthermore, the system frequency is constantly deviating around its nominal value, which sets the requirement to use a threshold to detect the perturbation. Taking these into consideration, this is why the trigger condition for energy control has used a tolerance bound.

3.3 Parametric Study on Energy Control

In this section, parametric analyses are conducted to investigate the merits of energy control in MMCs under different sizing and system conditions. These merits are related to the level of improvement in the frequency response. They specifically consider the severity of the frequency nadir and how long it takes to reach this point after the system is subjected to a perturbation (i.e., the duration of the arresting period). The design variables include the SM capacitance (C_{sm}), the system penetration level (ρ), and the inertia constant (H_{SG}) of the SG. Two MMCs with different ranges of energy storage are considered and subjected to two different perturbations. For each, the parametric analyses are described in this section.

3.3.1 MMC with Small Energy Storage

An MMC with a small energy storage, referred as MMC 1 henceforth, is first investigated. It has the same parameters as previously described in Table 3.2, with $N = 80$ SMs and a base SM capacitance of $C_{\text{sm}} = 4000$ μF. The inductances are $L_{\text{arm}} = 15$ mH and $L_{\text{link}} = 6$ mH (0.093 pu and 0.037 pu, respectively, using base values of 200 MVA and 110 kV). A parametric study is conducted by varying C_{sm} and the system RES penetration level ρ with the values listed in Table 3.3. This allows the frequency response improvement under different energy storage and penetration levels to be analyzed.

Table 3.3: Values used in SM Capacitance and RES Penetration Parametric Analysis for MMC 1

C_{sm}	[μF]	4000	4800	5600	6400	7200	8000
	[kJ/MW]	40	48	56	64	72	80
ρ		0.2	0.4	0.6	0.8		

Using the described test system, at $t = 40$ s, a perturbation of a 2% and 5% increase

in the load are individually applied. Since a wide variety of RES penetrated systems are involved in the case study, the perturbation is restricted from being too large to ensure that all cases remain stable for analysis. The transient behaviour of the frequency and SM voltages are observed for the 2% perturbation cases first.

Fig. 3.7 shows a sample of the time-domain frequency responses under varying RES penetration levels. Each curve represents a different penetration level, and the dashed and

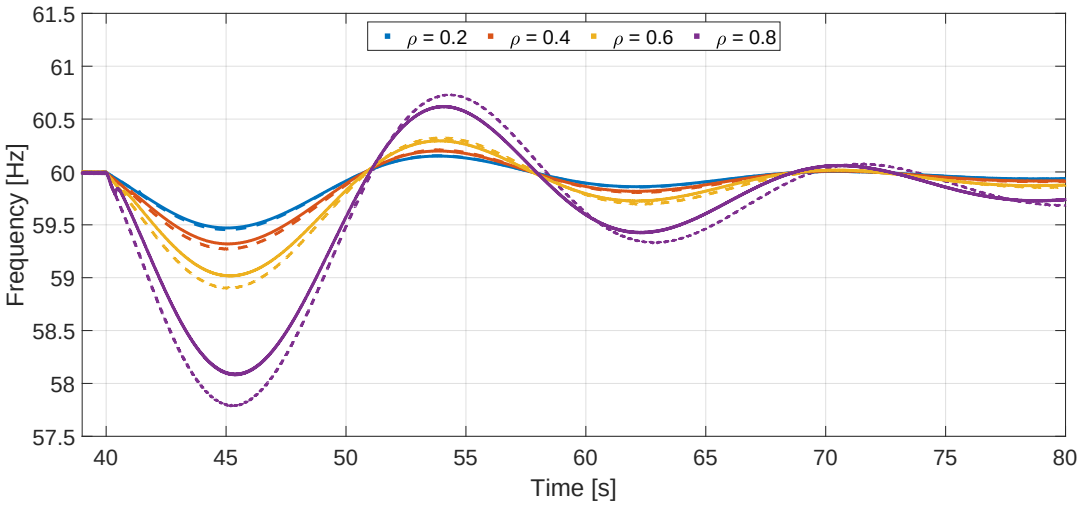

Fig. 3.7: Sample result of the system frequency responses under varying RES penetration levels with (solid lines) and without (dashed lines) energy control.

solid lines are to compare between when energy is not and is included, respectively. Similar to expectations, the frequency nadir is not as far deviated from the nominal value when energy control is included. However, it can also be seen that with increasing penetration levels, the frequency nadir becomes more severe. This is consequent of the decreasing system inertia, which makes the system more susceptible to frequency excursions.

Regardless of whether or not there is energy control, the frequency nadir is a larger deviation as the penetration level increases. In other words, while energy control does help

lower the frequency excursions, it does not fully compensate for the effect of decreasing inertia. Furthermore, the amount of improvement in the frequency nadir with energy control varies with the penetration level. This is later analyzed in a quantitative manner. Another point of emphasis is that the difference in the time duration of the arresting period due to energy control varies for each penetration case. This is because in higher RES penetrated systems, there are relatively more MMCs and, therefore, more energy available for frequency support. The duration of energy control is therefore longer, so the duration of the arresting period can be extended longer. A quantitative analysis on the time to the frequency nadir is also conducted later.

Fig. 3.8 shows a sample of the time-domain SM voltage responses under varying RES penetration levels. The observation from these waveforms is to help explain some of the

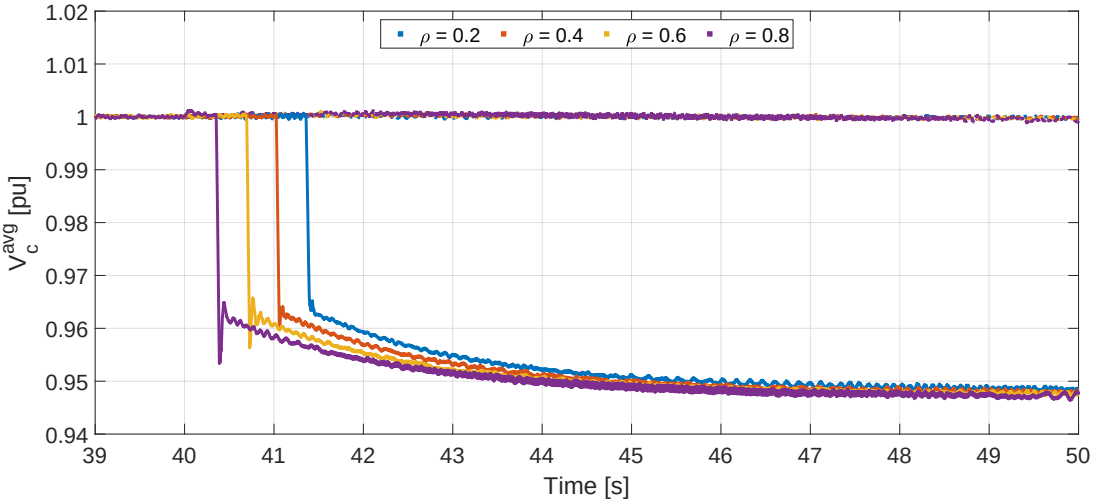

Fig. 3.8: Sample result of the SM voltage responses under varying RES penetration levels with (solid lines) and without (dashed lines) energy control.

behaviours seen in the frequency responses. As before, each curve represents a different penetration level, and the dashed and solid lines are to compare between when energy is

not and is included, respectively. In this case study, the system load is increased and is, therefore, in a power shortage. When there is no energy control, the SM voltages remain at their nominal values as per conventional control as illustrated. On the contrary, when there is energy control, all of the MMC capacitors are discharged from their nominal value to make up for the power imbalance to provide the excess power as reflected in the waveforms. After the capacitor voltage has dropped to a specified threshold (e.g., 0.95 pu as shown), energy control is deactivated because the SM capacitors must maintain a minimum charge in order for the MMC to function normally. This is enforced by the trigger conditions of the energy controller. It is noted that depending on the implementation, there may be small differences in the settling voltage, which may be attributed to the measurement of the average SM voltage. Due to SM voltage ripple, this difference is reasonable. It is small and does not impact the capabilities of energy control. Another behaviour of note is that the time instant at which the SM capacitors begin to discharge varies across the different penetration cases. As the penetration level increases, energy control is triggered sooner since the frequency violates the acceptable tolerance range due to the larger frequency excursions in lower inertia systems. This is consistent with the previously observed frequency responses.

With the behaviours of the responses observed in the time domain, it is useful to quantitatively evaluate the frequency improvement. This includes the frequency nadir and the time at which it occurs after the perturbation. In Fig. 3.9a, the frequency nadir with and without energy control is plotted against different energy storage levels on the horizontal axis and different penetration levels by different coloured lines. This is to observe the magnitudes of the frequency nadirs. In Fig. 3.9b, the percent improvement in the frequency nadir is plotted in a similar manner to show the quantitative comparison. There are three particular observations that should be noted from Fig. 3.9. First, increasing the penetration level generally shows

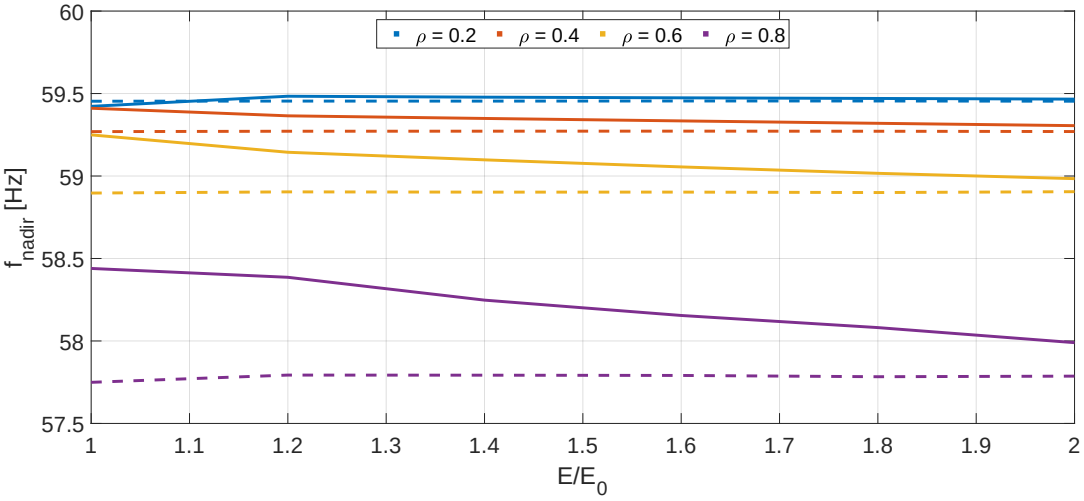

(a)

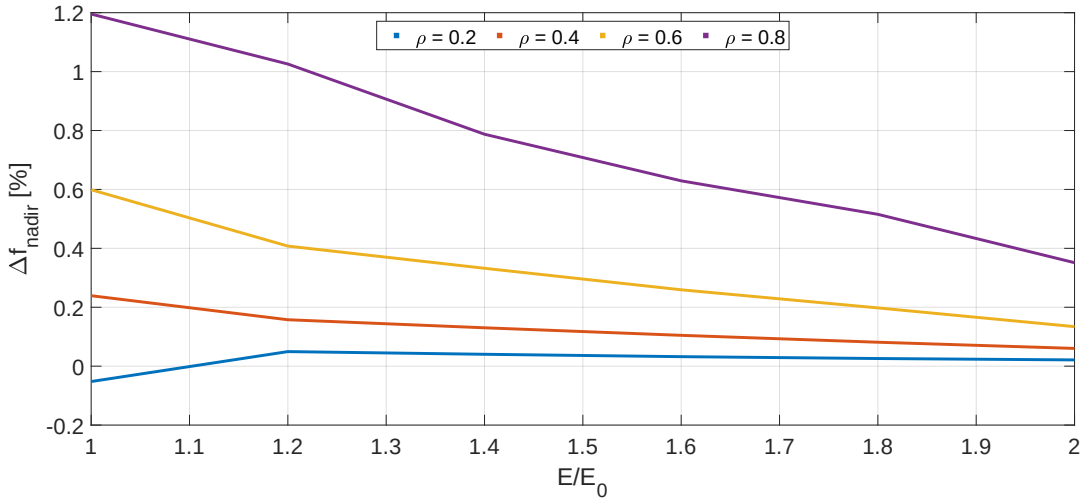

(b)

Fig. 3.9: Comparison of frequency nadirs by (a) magnitude for with (solid lines) and without (dashed lines) energy control, and by (b) percent improvement under varying energy storage capacities and RES penetration levels with MMC 1 subjected to a 2% increase in load.

greater improvement, but has diminishing returns. In this particular system, increasing the energy storage (via the SM capacitance) of the system decreased the level of improvement in the frequency nadir. Nevertheless, the frequency nadir when energy control is included still shows an improvement in the frequency nadir. Second, the energy storage capacity appears to have a larger effect on the frequency nadir improvement at higher penetration levels than at lower penetration levels. This may have to do with the fact that the load contribution is dominated by the MMCs, so their individual behaviour accumulates a greater overall effect. Lastly, regardless of the energy storage capacity or RES penetration level, the improvement in the frequency nadir is small. This may be because there is not enough energy available for use by energy control, or the discharge rate is too slow to manifest the necessary power. Both would have implications on the merits of energy control. It is important to note that this may also be due to the control parameters, which have a significant impact on the operation of energy control.

In Fig. 3.10, the time duration that the arresting period is extended by as a result of energy control is illustrated. Again the graph has the energy storage increasing along the horizontal axis, and different lines representing different penetration levels. The dashed and solid lines are to compare between when energy is not and is included, respectively. The percentage of improvement is also included. The duration of frequency control, and therefore the time extended to reach the frequency nadir, is theoretically directly proportional to the energy available for use. In this study, the rest of the parameters and the controls are the same across all cases, so as the energy storage of the MMC increases, this proportional relationship is expected to be observed. However, it can be seen from the graph that there are non-linearities in the time gained by energy control. At the base energy storage level, there are two inconsistencies to the expected results from theory to mention. The first is that the

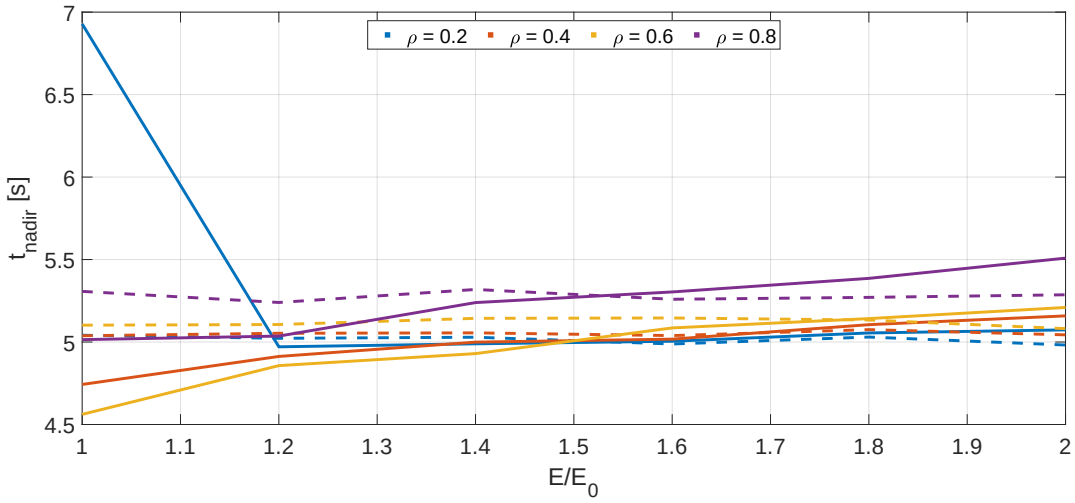

(a)

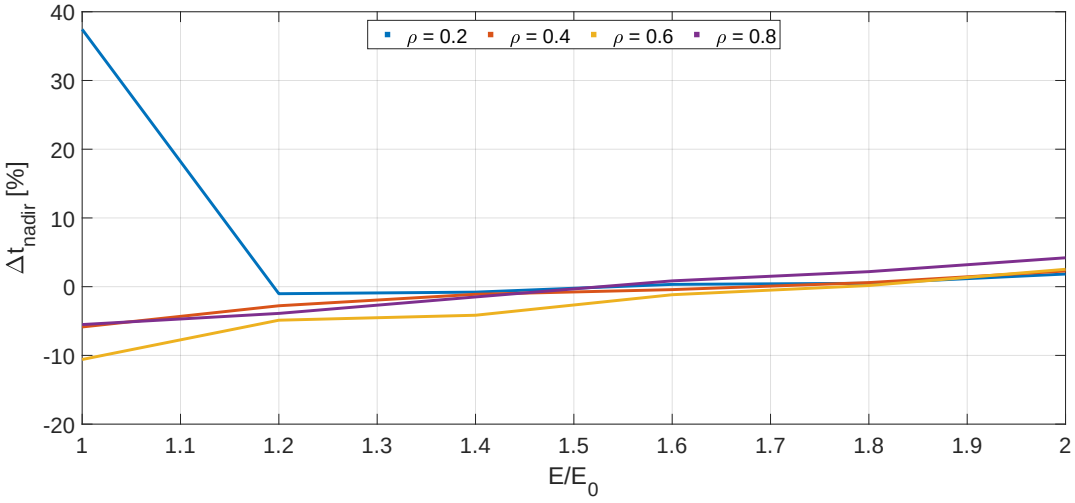

(b)

Fig. 3.10: Comparison of times to reach the frequency nadir after the perturbation occurs by (a) magnitude for with (solid lines) and without (dashed lines) energy control, and by (b) percent improvement under varying energy storage capacities and RES penetration levels with MMC 1 subjected to a 2% increase in load.

time gained by energy control is largest in the lowest RES penetrated system, and a system with a penetration level of 40% had a greater time gain than a system with a penetration level of 60%. The former is especially high compared to expectations. However, from the previous graph (Fig. 3.9) it must also be noted that this came at the cost of a slightly lower frequency nadir, which is undesirable. Furthermore, contrary to theoretical expectations, energy control does not always result in a time gain. The observed non-linearities may be attributed to controller parameters of the control systems. It is possible that the controllers could be better tuned for an improved response, however, all controller parameters were kept constant across all cases to preserve consistency. Nevertheless, as the energy storage levels increases, the general trend is that the amount of time bought by energy control when it is implemented increases. When there is no energy control, the time at which the frequency nadir occurs remains constant as expected. It must also be noted that the time at which the nadir occurs is earlier than when there is no energy control for the lower energy storage levels. These observations highlight the importance of such analyses due to the differences between theory and results.

Using the same system and parametric values, the study is now conducted for a larger perturbation of 5% load increase. The frequency nadir results are presented in Fig. 3.11. It is noted that the frequency nadir is lower than in the 2% perturbation study for all parametric cases. This is expected because the magnitude of the perturbation increased while all other parameters remained unchanged. Without energy control, this is the main difference between these two cases. On the other hand, with energy control, it is observed that there is generally less improvement in the frequency nadir as the energy storage capacity increases as before. The trends as observed in the 2% perturbation case are seen again here. As the improvement is still small, but the frequency nadir itself is more significant, it shows that the energy

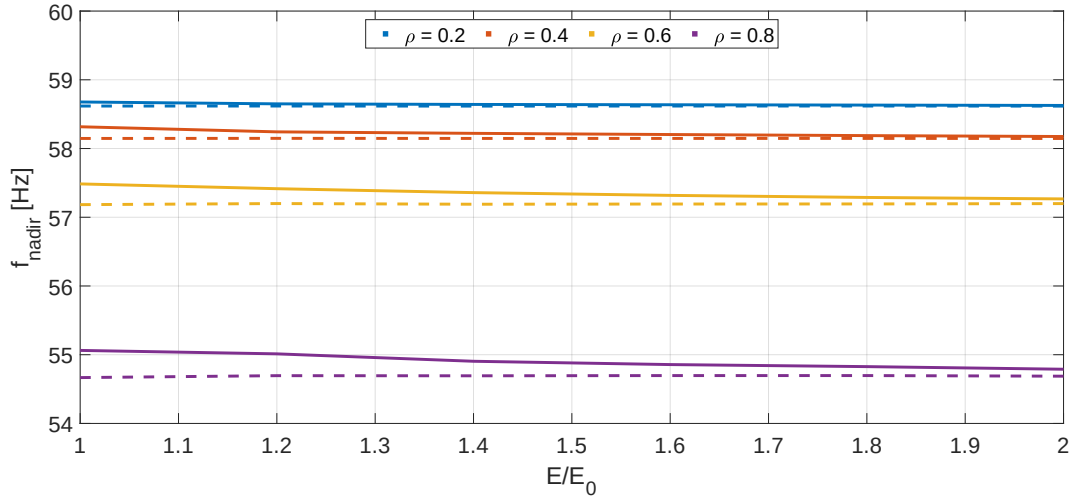

(a)

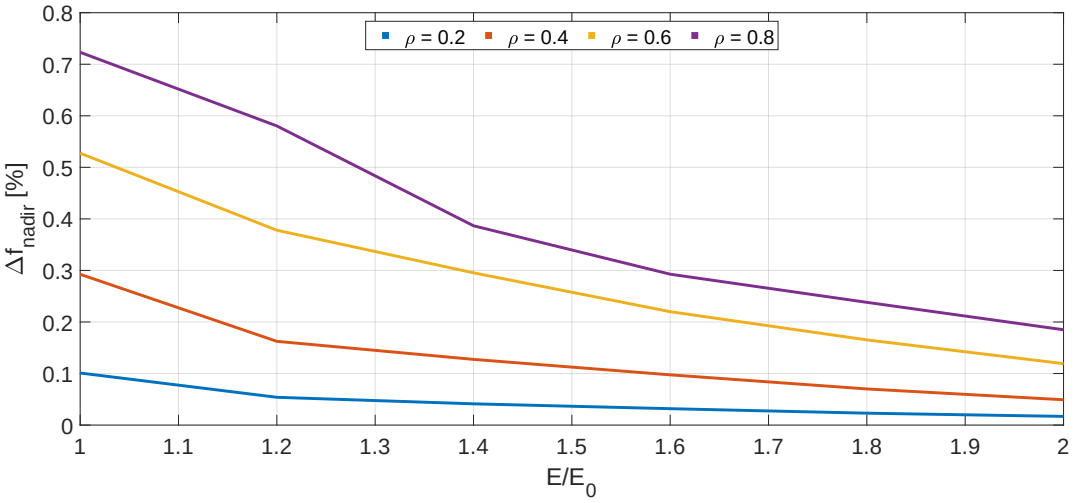

(b)

Fig. 3.11: Comparison of frequency nadirs by (a) magnitude for with (solid lines) and without (dashed lines) energy control, and by (b) percent improvement under varying energy storage capacities and RES penetration levels with MMC 1 subjected to a 5% increase in load.

control alone does not sufficiently improve the frequency response. Furthermore, it appears that the percentage improvement in the higher RES penetrated systems are impacted more by the increased perturbation than the lower RES penetrated systems. This observation is quantitatively analyzed next.

The improvement in the frequency nadir is explicitly compared between the two perturbation cases as a percent improvement in Fig. 3.12. The comparison is done with respect to

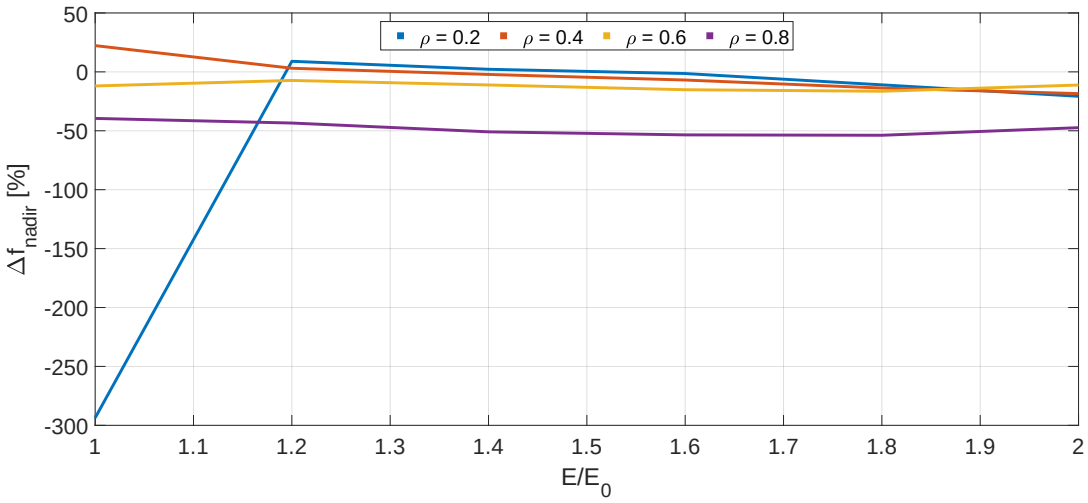

Fig. 3.12: Comparison of the percent improvement in the frequency nadir due to energy control between a 2% and 5% increase in load under varying energy storage capacities and RES penetration levels with MMC 1.

the 2% perturbation case. In other words, a positive percent improvement means that the 5% perturbation case showed greater merit, and a negative percent improvement means that the 2% perturbation case showed greater merit. With the lowest RES penetration level at base energy storage, the result is significantly different than the other parametric cases as observed before, and is attributed to the controller parameters. It is generally seen that the improvement in the frequency nadir is larger than in the 2% perturbation case with the lower RES penetration levels (20% and 40%), but is often larger with higher RES penetration levels

(60% and 80%). The latter directly corresponds to the increasing concern that higher RES penetrated systems are more prone to perturbations than lower RES penetrated systems, and therefore demonstrates the importance of energy control. As the energy storage capacity increases, these differences become less significant. In other words, the diminishing returns in the smaller perturbation case with higher RES penetration levels is more prominent. This means that when the system is subjected to a small perturbation, it is important to take the RES penetration level into account to evaluate whether energy control should be triggered. It is noted, however, that the percent changes in the frequency nadir are still low.

The time after the perturbation at which it occurs are presented in Fig. 3.13 respectively. Again, not all cases result in an improvement in the time to reach the frequency nadir for when the energy storage capacity is low, and differences from theory in the time gained to reach the frequency nadir due to energy control are observed. The largest RES penetrated system, which should have the largest time gain, has the least of all the RES penetration levels in magnitude. In terms of percent improvement, however, the largest RES penetrated system generally reflects what is expected from theory. There are also generally more cases with an improvement in the time to reach the frequency nadir after the perturbation occurs than the 2% perturbation case. The results are impacted by the magnitude of the perturbation, which places the MMC in a different operating point. This affects whether its controller parameters result in beneficial or adverse effects.

The times to reach the frequency nadir are compared between the 2% and 5% perturbation cases as a percent improvement in Fig. 3.14. As shown, when the energy storage capacity of the MMC is increased by 80%, the 5% perturbation case shows significantly more merit than the 2% case. On the other hand, while not as significant, the 2% perturbation case shows notable more merit than the 5% case. Almost all of the cases show that the 2% per-

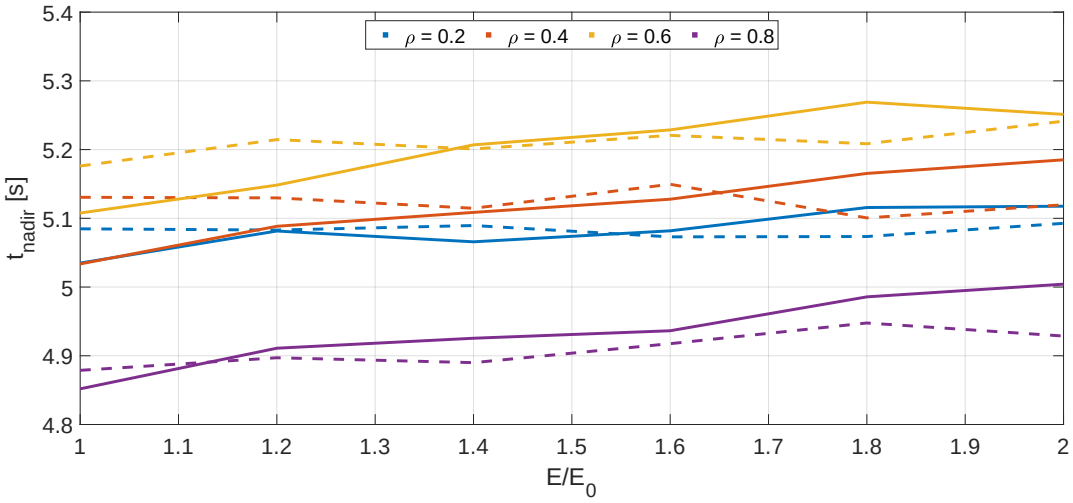

(a)

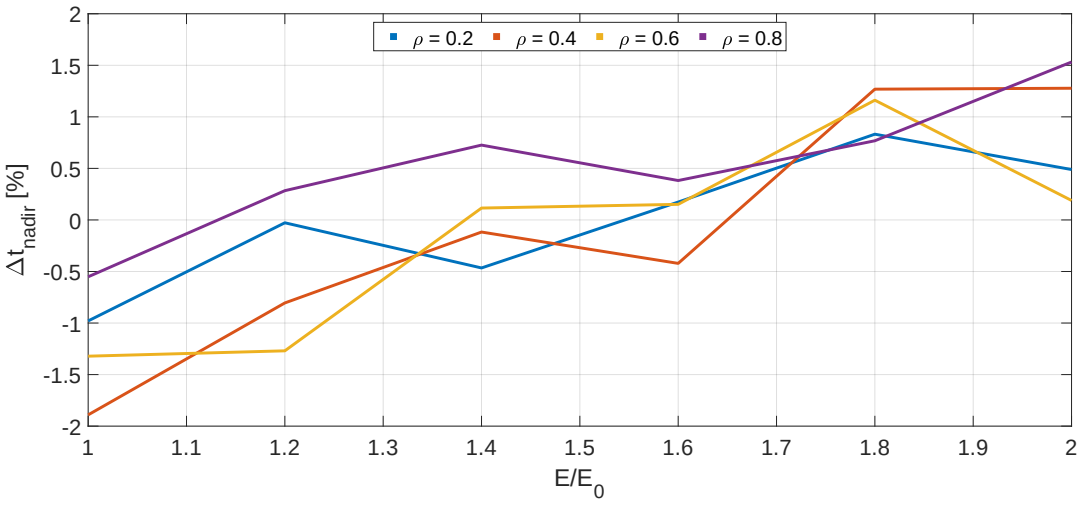

(b)

Fig. 3.13: Comparison of times to reach the frequency nadir after the perturbation occurs by (a) magnitude for with (solid lines) and without (dashed lines) energy control, and by (b) percent improvement under varying energy storage capacities and RES penetration levels with MMC 1 subjected to a 5% increase in load.

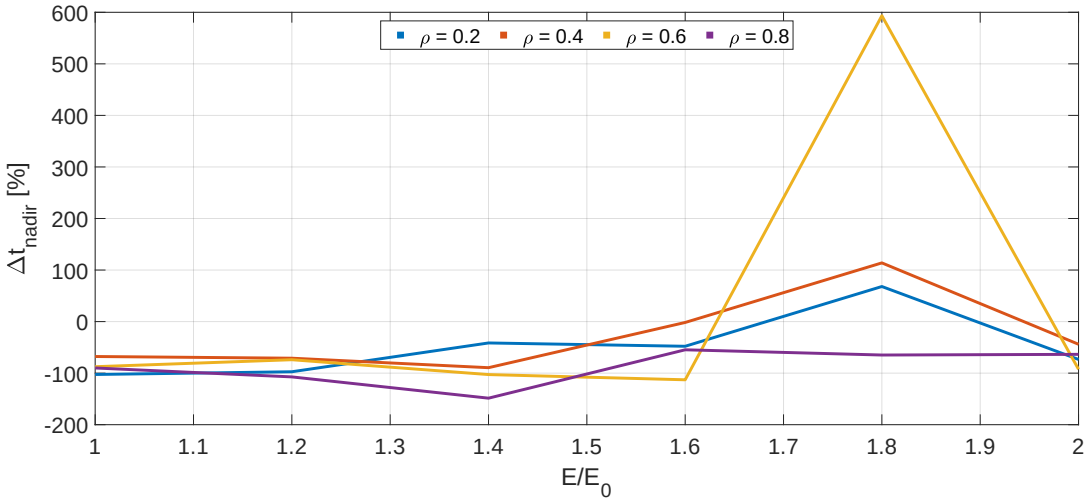

Fig. 3.14: Comparison of the percent improvement in the time to reach the frequency nadir after the perturbation occurs due to energy control between a 2% and 5% increase in load under varying energy storage capacities and RES penetration levels with MMC 1.

turbation case had greater merit. This is because energy control is expected to terminate earlier with larger perturbations due to the faster release rate of energy.

3.3.2 MMC with Large Energy Storage

An MMC with a large energy storage, referred as MMC 2 henceforth, is investigated in this section. It has $N = 12$ SMs with a base SM capacitance $C_{\text{sm}} = 4000$ μF. The inductances are $L_{\text{arm}} = 4.7$ mH and $L_{\text{link}} = 11$ mH (0.03 pu and 0.069 pu, respectively, using base values of 200 MVA and 110 kV). The SM capacitance and RES penetration levels are varied in a parametric manner. The same values are used as with MMC 1, but the kJ/MW conversion has been updated as shown in Table 3.4. The control system also remains the same, except the controller gains have been adjusted for MMC 2.

The first difference between MMC 1 and MMC 2 is the number of SMs. The number of

Table 3.4: Values used in SM Capacitance and RES Penetration Parametric Analysis for MMC 2

$C_{\mathbf{sm}}$	$[\mu\mathbf{F}]$	4000	4800	5600	6400	7200	8000
	$[\mathbf{kJ/MW}]$	267	320	373	427	480	533
$\boldsymbol{\rho}$		0.2	0.4	0.6	0.8		

SMs affects the nominal SM voltage (since both MMCs have the same rated DC voltage), which affects the total energy storage. MMC 2 has a larger nominal SM voltage and therefore more energy available for frequency support. The other difference is that they have different controller parameters for the same control system. It is noted that the energy storage of MMC 2 is relatively significant. In MMC 1, the operation of energy control was limited by the amount of energy that was available for use. MMC 2 has this energy increased relative to MMC 1, which allows the study to investigate the effectiveness of energy control when it is able to (theoretically) operate for a longer time duration. From an alternative perspective, the available energy could also be supplied from other energy reserves, such as battery energy storage systems, and not solely from the SMs of the MMC. A parametric study is conducted by varying C_{sm} and the ρ in the same manner as MMC 1. The frequency nadirs and the time at which they occur after the perturbation are analyzed (i.e., the duration of the arresting period) for MMC 2 and compared against those obtained with MMC 1.

In Fig. 3.15, the frequency nadir with and without energy control is plotted against different energy storage levels on the horizontal axis and different penetration levels by different coloured lines. The dashed and solid lines are to compare between when energy is not and is included, respectively. The percent improvement is included for a quantitative observation. Once again, there is not much improvement in the frequency nadir, but energy control does have a nadir closer to the nominal frequency nonetheless. MMC 1 had an almost monotonically decreasing trend for the percent improvement in the frequency nadir. This is not the

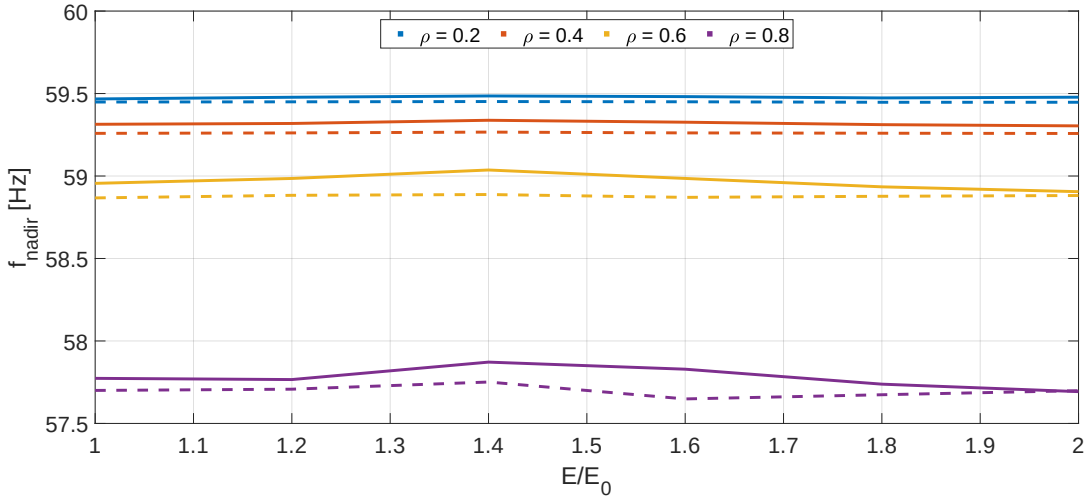

(a)

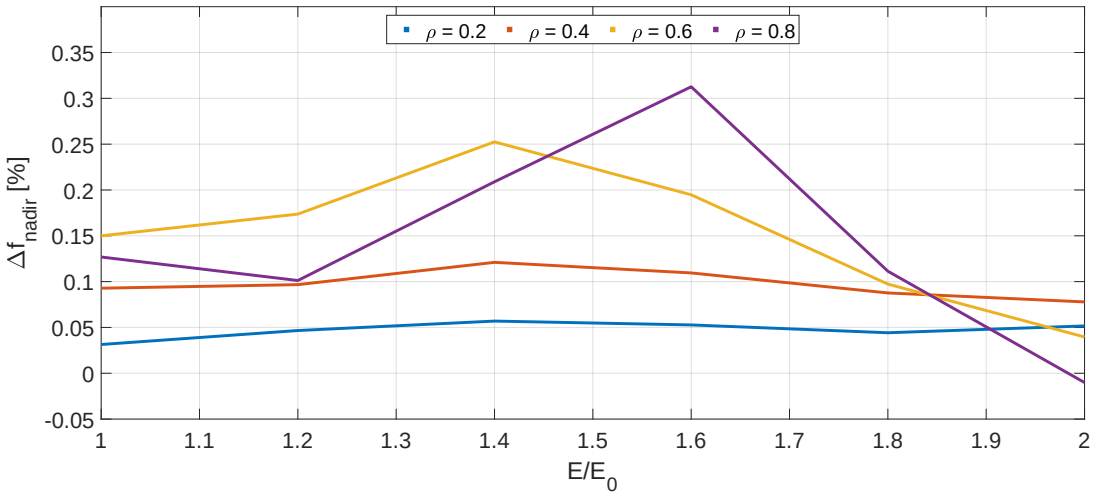

(b)

Fig. 3.15: Comparison of frequency nadirs by (a) magnitude for with (solid lines) and without (dashed lines) energy control, and by (b) percent improvement under varying energy storage capacities and RES penetration levels with MMC 2 subjected to a 2% increase in load.

case in MMC 2. In MMC 2, the frequency nadir improvement level is relatively constant across varying energy storage levels for low penetration levels. For higher penetration levels, the diminishing returns becomes evident after around a $40-60\%$ increase in the energy storage as shown. These are attributed to the differences in their controller parameters, which means that the observed behaviour can be affected by the controller parameters. The level of improvement could be either increased or decreased depending on the controller tuning. However, all controller parameters have been kept constant across all parametric cases to maintain consistency. In theory, both MMCs were expected to show an improved frequency nadir with their increasing energy capacities which allow for greater power compensation.

In Fig. 3.16, the time duration that the arresting period is extended by as a result of energy control is illustrated in the same manner as the previous graphs. It can be seen that as the energy storage levels increase, the time extended to reach the frequency nadir increases. Furthermore, the effect is amplified with higher penetration levels. These are all due to the increasing levels in the energy storage, and therefore the time duration that energy control can be active for. It is emphasized that the time extension is more sensitive to the increasing penetration level than the energy storage level. This is because there is a greater increase in the available energy when the penetration level increases. However, this improvement is not linear as shown. It is also implied that at high penetration levels, the energy storage rating does not need to be as large to achieve the same effect. This makes energy control more practical. For MMC 2, while energy control may not have improved the nadir, it still extended the duration of the arresting period and, therefore, effectively improved the ROCOF. Compared to MMC 1, the time extension is larger due to the larger total energy storage MMC 2 has. Furthermore, all of the cases showed an improvement in the time extension. This is a consequence of having a larger nominal SM voltage. In this

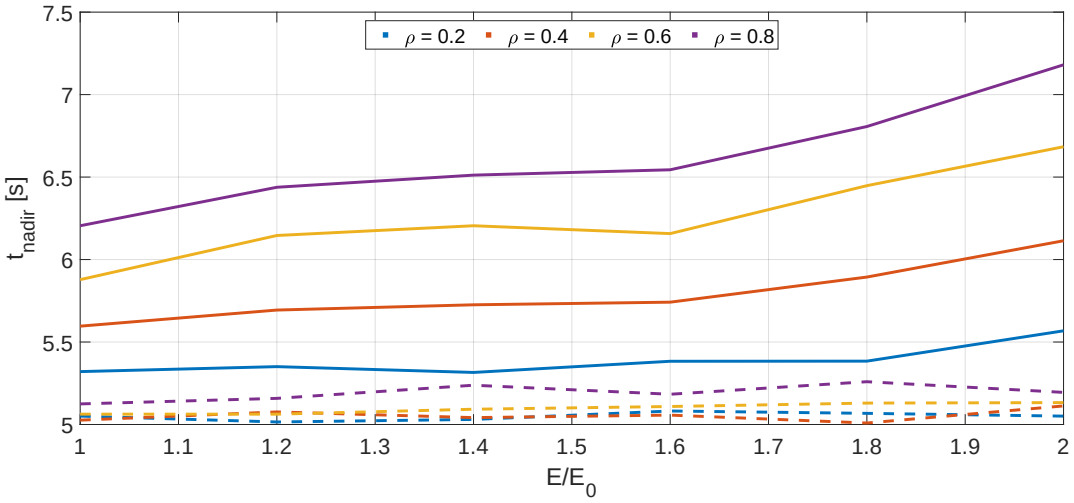

(a)

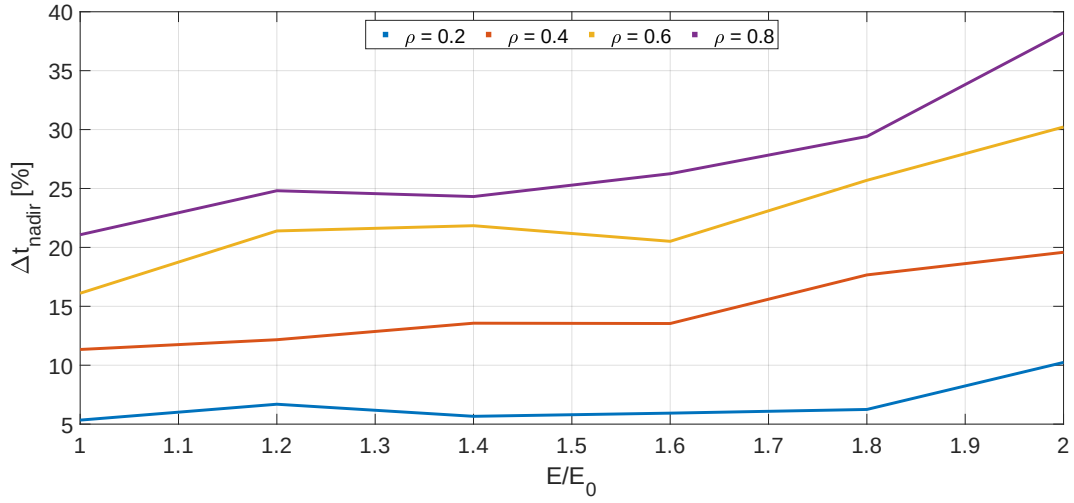

(b)

Fig. 3.16: Comparison of times to reach the frequency nadir after the perturbation occurs by (a) magnitude for with (solid lines) and without (dashed lines) energy control, and by (b) percent improvement under varying energy storage capacities and RES penetration levels with MMC 2 subjected to a 2% increase in load.

particular case, the increase in the nominal SM voltage is more significant than the number of SMs decreased. However, increasing the energy storage capacity does not necessarily have a linear effect on the time extension. This must be taken into account when sizing the SM capacitors for energy control. Furthermore, from a practical perspective, it is not necessarily the case that the the MMC will have a large energy storage due to a relatively high nominal SM voltage. It is the SM capacitance that needs to be high because the nominal SM voltage is typically limited by the switch ratings. Conventionally, the SM capacitance is sized by the SM voltage ripple and in the interest of cost and volume. With energy control, the implications on the MMC response speed need to be considered.

When the perturbation is increased to 5%, the frequency nadirs are observed and shown in Fig. 3.17. There is still not much improvement in the magnitude of the frequency nadir, but it can be seen through the percent improvement that there are variations compared to the 2% perturbation case. As shown, the largest RES penetration level does not have as much improvement compared to before. Instead, there is more improvement in the 60% RES penetrated system. The observations are attributed to the controller parameters. The controller parameters are optimized for the normal operating point of the MMC. However, after the perturbation occurs, the MMC is at a different operating point which may impact energy control in a non-linear manner. As with MMC 1, while it is possible that the controllers could be better tuned for an improved response, all controller parameters were kept constant across all cases to preserve consistency.

The percent improvements in the frequency nadir are compared between the 2% and 5% perturbation cases as a percent improvement in Fig. 3.18 to quantitatively show the effect of the perturbation magnitude. As before, a positive percent improvement means greater merit in the 5% perturbation case, and a negative percent improvement means greater merit in

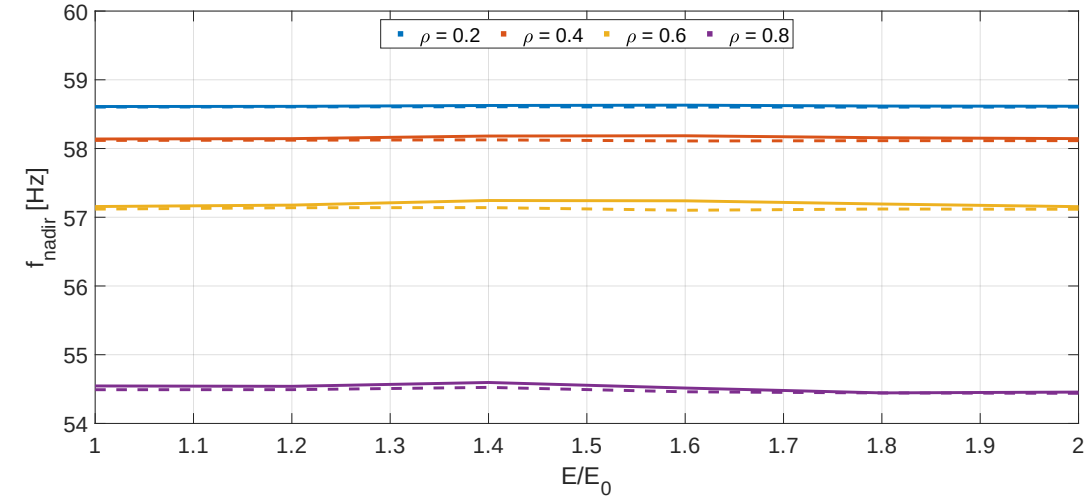

(a)

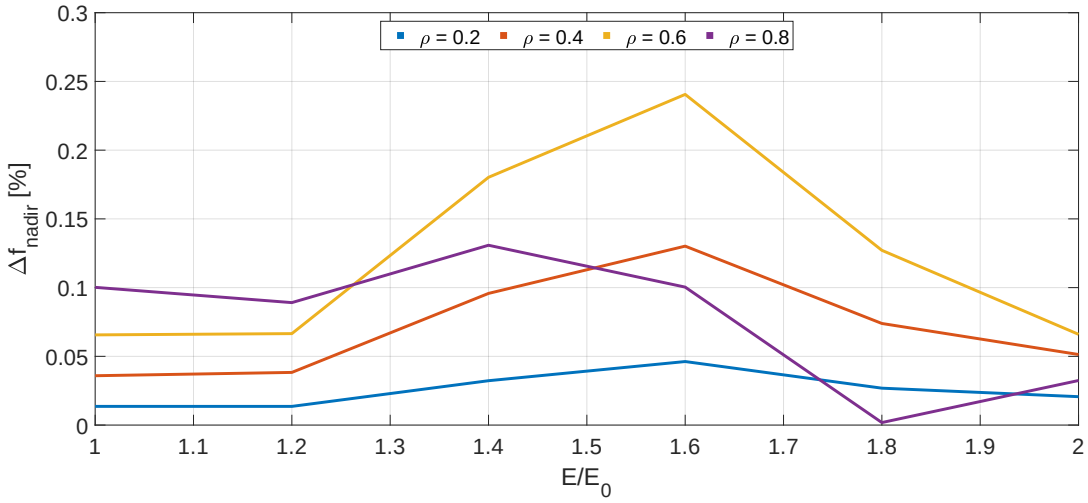

(b)

Fig. 3.17: Comparison of frequency nadirs by (a) magnitude for with (solid lines) and without (dashed lines) energy control, and by (b) percent improvement under varying energy storage capacities and RES penetration levels with MMC 2 subjected to a 5% increase in load.

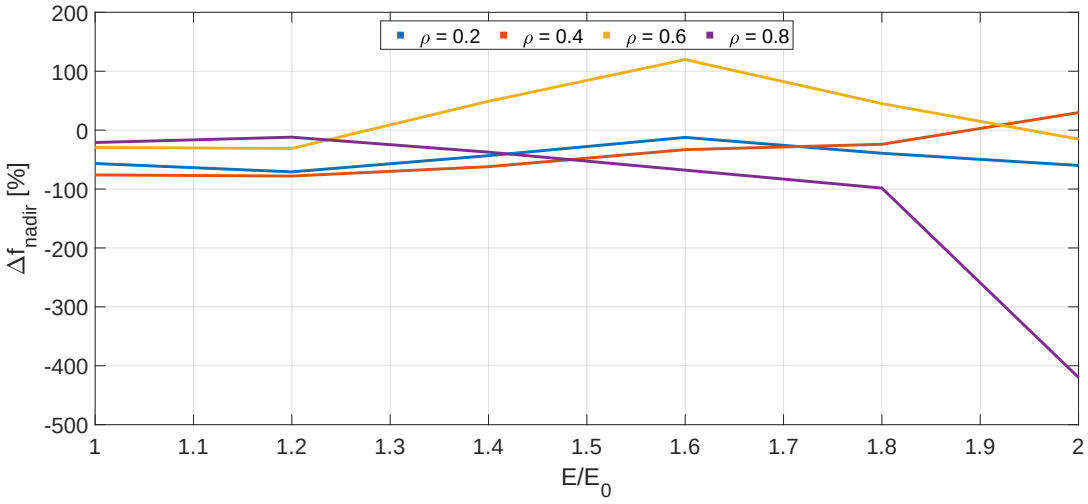

Fig. 3.18: Comparison of the percent improvement in the frequency nadir due to energy control between a 2% and 5% increase in load under varying energy storage capacities and RES penetration levels with MMC 2.

the 2% perturbation case. It is evident that for almost all cases, the 2% perturbation case had a greater percent improvement in the frequency nadir. This trend is similar to MMC 1 and is attributed to the fact that more energy is required for energy control to provide the same level of improvement when the system is subjected to a larger perturbation.

The duration of the arresting period is also observed as shown in Fig. 3.19. It can be seen that the time after the perturbation at which the frequency nadir occurs is not always longer with energy control as with the 2% perturbation case. More significantly, the 80% RES penetrated system now has the least merit in terms of magnitude instead of the greatest. However, it still has the largest percent improvement. The percent improvement is also increasing in close accordance with theory. It is particularly evident in this graph that the percent improvement in the time is less than for the 2% perturbation because of the higher energy demand rate. As an example, for the 80% RES penetrated system, the largest percent improvement obtained was close to 40% with the 2% perturbation, but is less than 20% with

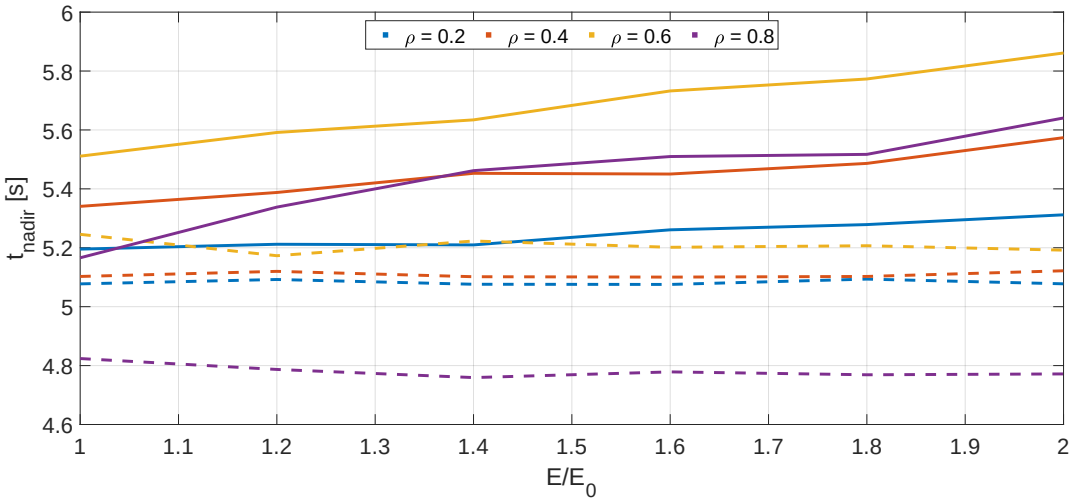

(a)

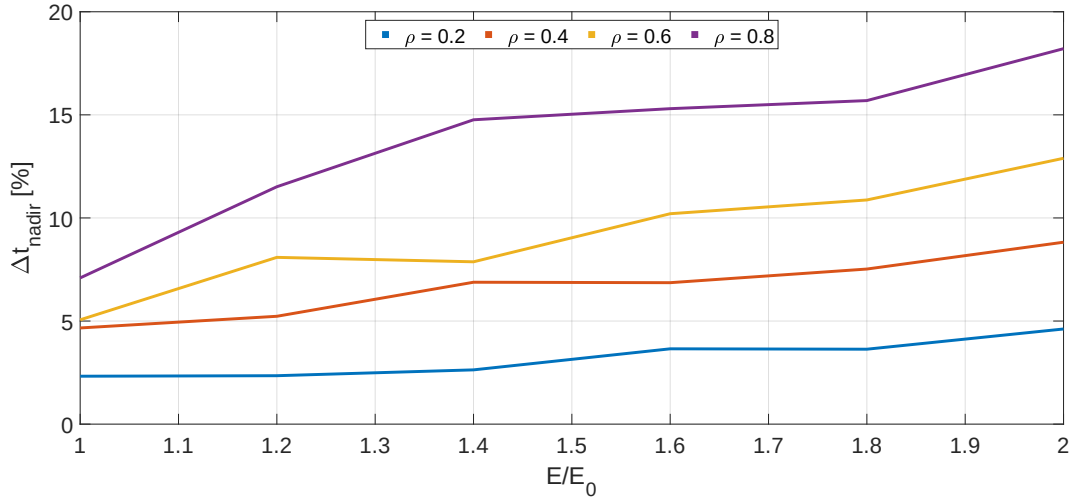

(b)

Fig. 3.19: Comparison of times to reach the frequency nadir after the perturbation occurs by (a) magnitude for with (solid lines) and without (dashed lines) energy control, and by (b) percent improvement under varying energy storage capacities and RES penetration levels with MMC 2 subjected to a 5% increase in load.

the 5% perturbation.

The times to reach the frequency nadir are compared between the 2% and 5% perturbation cases as a percent improvement in Fig. 3.20. The 2% perturbation case has greater merit

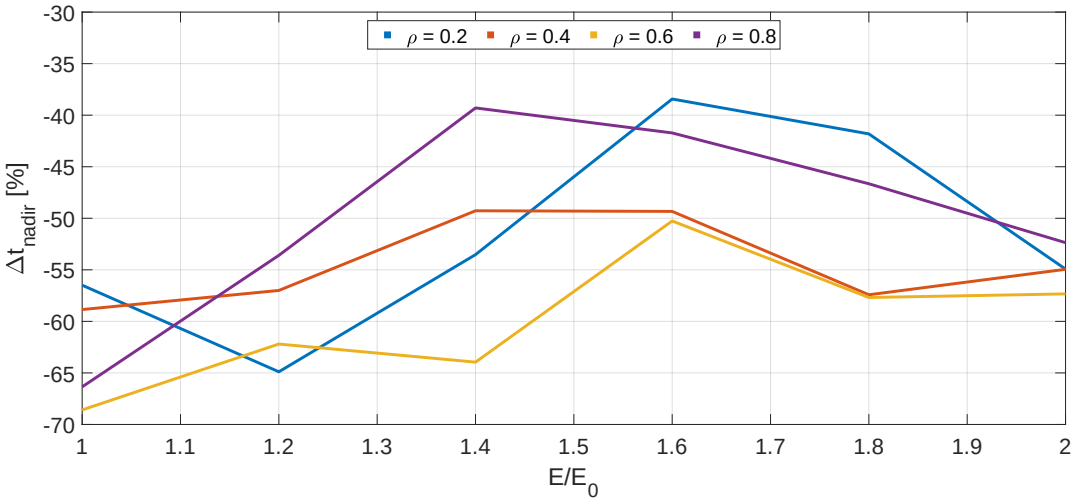

Fig. 3.20: Comparison of the percent improvement in the time to reach the frequency nadir after the perturbation occurs due to energy control between a 2% and 5% increase in load under varying energy storage capacities and RES penetration levels with MMC 2.

for all the presented cases. This is consistent with the MMC 1. The need for more energy as the perturbation levels increase appears to be emphasized once again. This may not be the only case, however. As MMC 2 already has a relatively large energy storage capacity, it is more likely that the performance is impacted by the release rate ability of the SM capacitors. The capacitors may not be able to discharge as fast as the energy controller demands of it, especially since the perturbation and therefore necessary discharge rate has increased. This is a limitation of energy control that must be considered during design.

3.3.3 Inertia of Synchronous Generators

As the system penetration level increases, the total system inertia decreases as a result of the SGs having less total contribution to the load. This results in the increasing severity of frequency excursions. In the previous two examples (MMC 1 and MMC 2), while energy control could beneficially alter the frequency response, it was clear that the inertia of the system had an impact on how well the frequency response was improved. The system inertia was previously decreased by varying the system penetration level. However, it is also possible to decrease the system inertia through the inertia constant of the SGs. To test this, the same test system with MMC 1 is run at a fixed penetration level of 60%, and SM capacitance and the inertia constant of the SGs is varied according to Table 3.5.

Table 3.5: Values used in SM Capacitance and Inertia Constant Parametric Analysis

$C_{\mathbf{sm}}$	[μ**F**]	4000	4800	5600	6400	7200	8000
	[**kJ/MW**]	40	48	56	64	72	80
$H_{\mathbf{SG}}$	[**s**]	3	4	5	6		

MMC 1 is selected because it has more SMs as is typical in HVDC applications and the perturbation of a 2% increase in load is used. In Fig. 3.21, the frequency nadir is plotted against different values of SG inertia constants on the horizontal axis and different MMC energy storage levels by different coloured lines. The frequency nadir remains constant across different energy storage levels when energy control is not active as before and expected. With energy control, MMC 1 previously showed diminishing returns in the frequency nadir improvement and the same is seen again. Each curve represents a case with a different SG inertia constant, and it is evident that the frequency nadir improvement is not much affected across different SG inertia values. While the values of the frequency nadirs is decreasing with

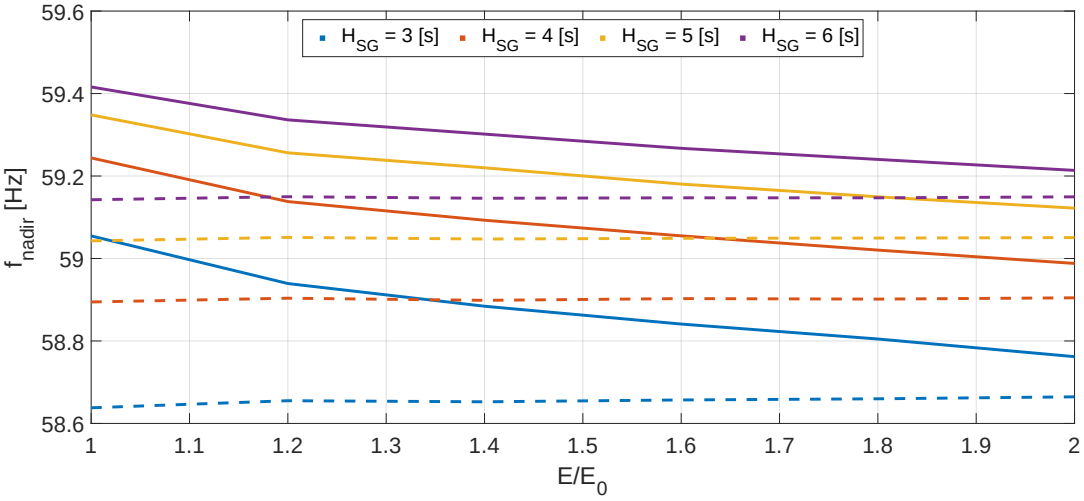

(a)

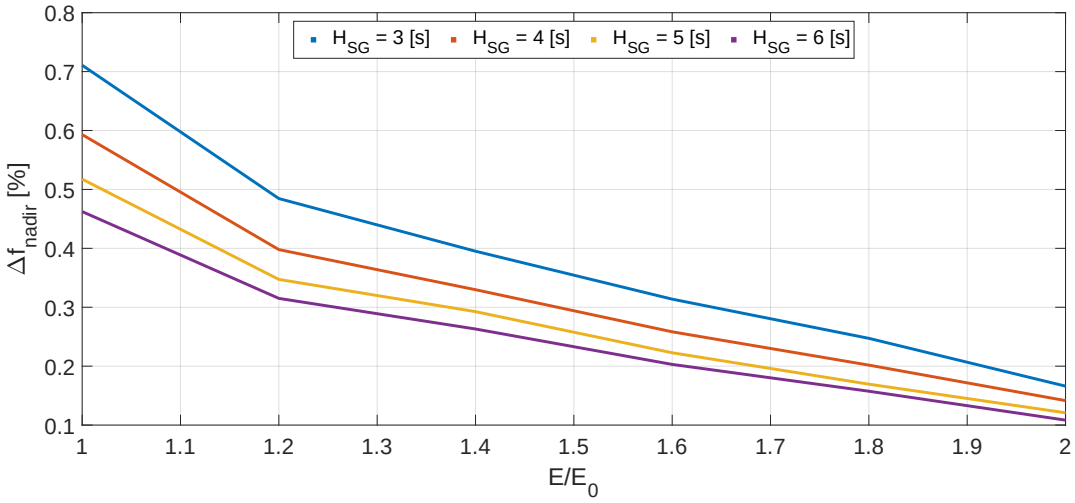

(b)

Fig. 3.21: Comparison of frequency nadirs by (a) magnitude for with (solid lines) and without (dashed lines) energy control, and by (b) percent improvement under varying energy storage capacities and SG inertia constants with MMC 1.

the decreasing inertia as per theory, there is relatively less improvement in the frequency. These are all consistent and similar with the parametric study on varying RES penetration levels, because both of these studies relate to the decreasing inertia of the system. The importance of this graph is to emphasize that energy control does not fully compensate the increased frequency excursions with the decreasing inertia of the system due to using SGs with smaller inherent inertia.

In Fig. 3.22, the times to reach the frequency nadir due to energy control are plotted against different values of the inertia constant of the SGs on the horizontal axis and different energy storage levels by different coloured lines. As shown, the results are consistent from the previously obtained results. There is no improvement in the time to the frequency nadir when energy control is not active, and energy control does not always improve the duration of the arresting period. This emphasizes the importance of sizing the SM capacitors correctly and selecting the corresponding controller parameters properly. However, similar to the parametric study on varying RES penetration levels, the improvement in the time increases with increasing energy storage levels. This is true with the decreasing inertia of the SGs as well, because it equivalently corresponds to increasing RES penetration levels as the load contribution becomes more dominated by the RESs. This graph provides a different perspective on how different system parameters impact the effects of energy control.

3.4 Summary

In this chapter, the basis of energy control was reviewed and implemented in a system with SGs and MMCs. Parametric analyses were conducted with varying SM capacitances, RES penetration levels, and SG inertia constants through detailed PSCAD/EMTDC simulations

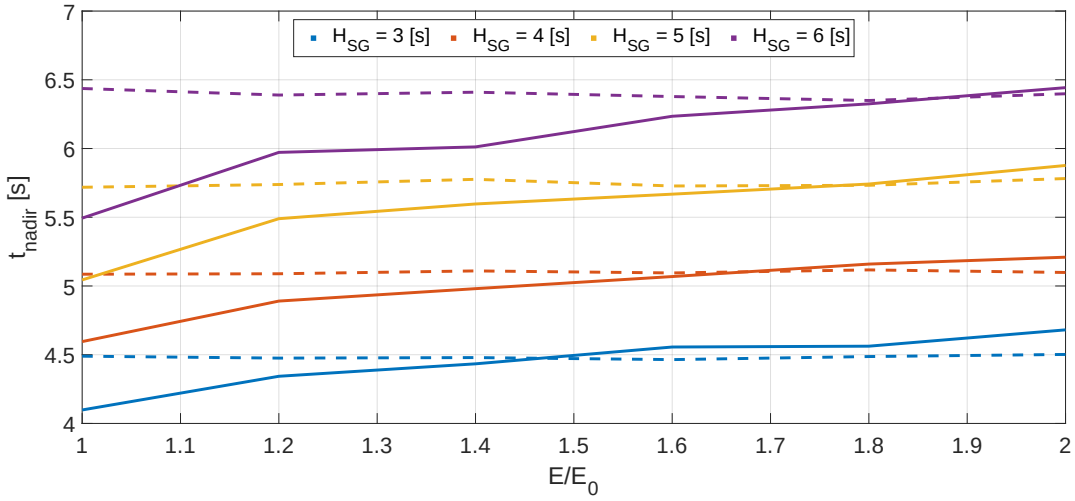

(a)

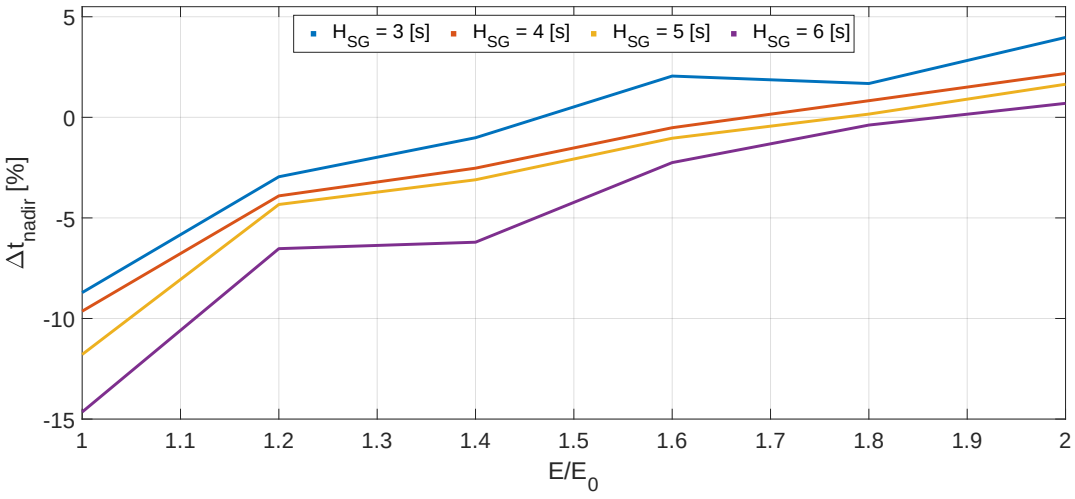

(b)

Fig. 3.22: Comparison of the times to frequency nadirs by (a) magnitude for with (solid lines) and without (dashed lines) energy control, and by (b) percent improvement under varying energy storage capacities and SG inertia constants with MMC 1.

to investigate their impact on the effectiveness of energy control to improve the frequency response. Two MMCs with a different number of SMs and controller parameters were tested and subjected to two different perturbations.

Results showed that increasing the energy storage of the MMC by increasing the SM capacitance showed improvements in the frequency nadir and arresting period duration, but also showed diminishing returns. In other words, there is an upper limit on SM capacitance. The usage of energy control in systems with higher RES penetration levels generally showed greater improvements because of the greater total energy available. The improvements in the frequency nadir can partially compensate for the increasing frequency deviations due to increasing penetration levels and decreasing SG inertia. It was also seen that the level of improvement decreased with larger perturbations, because either faster controllers or a larger energy storage is needed for the energy controller to have the same level of improvement. Furthermore, the controller parameters introduced non-linearities in the results that caused them to deviate from those expected from theory, and there was not always an improvement in the inertial response. This highlights the importance of conducting detailed studies.

Energy control is implemented as an additional functionality to the fundamental operation of an MMC that does not require additional electrical components to the system. In other words, its operation is dependent on the MMC design, so different operating and MMC sizing parameters affect how well it improves the frequency response. It must also be ensured that energy control does not compromise the conventional operation of the MMC.

Chapter 4

Response Speed Modelling and Sizing Considerations of MMCs

The level of improvement in the frequency response contributed by energy control is dependent on the MMC's ability to charge/discharge its SM capacitors within a sufficient amount of time. As power is the derivative of energy with respect to time, if the SM voltages cannot change fast enough, the power contributions expected by energy control to counter the power imbalances from a perturbation may be compromised. This means that even if the MMC has a large energy storage capacity available for use by energy control, there may not be improvements in the frequency response because the MMC is not capable of absorbing/releasing the energy at the rate demanded by energy control.

In this chapter, parametric analyses on various MMC parameters are conducted. These parametric analyses are conducted through a developed mathematical model that is validated against detailed simulations in PSCAD/EMTDC. The model development will first be discussed, followed by its validation and investigation of the results.

4.1 Derivation of Mathematical Model

In this section, the derivation of the model is presented. The model is a 2 x 2 state-space representation of the DC components of the SM voltages and arm currents of an MMC. From this model, a closed-form expression is derived from which the settling time of these waveforms can be approximated. The explicit construction of these waveforms is not necessary, which makes the model computationally efficient for this purpose. The two state equations of the model are derived with the MMC's operating point and their individual differential equations as the basis. While the DC components of the SM voltages and arm currents are the state variables, the derivation for each involves the AC components as well.

The first state variable that is defined in this section is the DC component of the SM capacitor voltage. The dynamics of the capacitor voltage of a SM in the upper arm of the converter are governed by the following differential equation:

$$\frac{\mathrm{d}}{\mathrm{d}t} v_{\mathrm{c}}^{\mathrm{up}} = \frac{1}{C_{\mathrm{sm}}} m^{\mathrm{up}} i^{\mathrm{up}}, \tag{4.1}$$

where m^{up} is the modulation reference waveform for the upper arm and i^{up} is the upper arm current. The modulation reference waveform is based on m^{ref} which defines the operating point of the MMC. This derivation will consider its fundamental component and an optional second-harmonic injection (when CCSC is included, for example), expressed as

$$m^{\mathrm{ref}} = m_1 \sin(\omega t + \alpha_1) + m_2 \sin(2\omega t + \alpha_2), \tag{4.2}$$

where m_1 is the modulation index and α_1 is the phase shift for the fundamental frequency component, and m_2 is the modulation index and α_2 is the phase shift for the second order

frequency component. Then for the upper arm of phase a,

$$m^{\mathrm{up}} = \frac{1}{2}\Big(1 - m^{\mathrm{ref}}\Big). \tag{4.3}$$

The arm current may be represented as a Fourier series

$$i^{\mathrm{up}} = I_0 + \sum_{n=1}^{\infty} I_n \sin(n\omega t + \varphi_n). \tag{4.4}$$

To simplify the analysis, only the current harmonics up to the second one are considered. This is because higher-order current harmonics are typically of much smaller magnitude and may therefore be neglected without compromising accuracy in typical cases [15–17]. Then (4.4) may be reduced to

$$i^{\mathrm{up}} = I_0 + I_1 \sin(\omega t + \varphi_1) + I_2 \sin(2\omega t + \varphi_2). \tag{4.5}$$

Equation (4.2) is substituted into (4.3), and then with (4.5) into (4.1). Expanding the terms, applying basic trigonometric identities, and then simplifying yields

$$\frac{\mathrm{d}}{\mathrm{d}t} v_{\mathrm{c}}^{\mathrm{up}} = \frac{\mathrm{d}}{\mathrm{d}t} V_{\mathrm{c0}} + \frac{\mathrm{d}}{\mathrm{d}t} v_{\mathrm{c1}} + \frac{\mathrm{d}}{\mathrm{d}t} v_{\mathrm{c2}} + \frac{\mathrm{d}}{\mathrm{d}t} v_{\mathrm{c3}} \tag{4.6}$$

where

$$\frac{\mathrm{d}}{\mathrm{d}t} V_{\mathrm{c0}} = \frac{1}{2C_{\mathrm{sm}}} I_0 - \frac{m_1}{4C_{\mathrm{sm}}} I_1 \cos(\alpha_1 - \varphi_1) - \frac{m_2}{4C_{\mathrm{sm}}} I_2 \cos(\alpha_2 - \varphi_2) \tag{4.7a}$$

$$\frac{\mathrm{d}}{\mathrm{d}t}v_{\mathrm{c1}} = \frac{1}{2C_{\mathrm{sm}}}I_1\sin(\omega t+\varphi_1) - \frac{m_1}{2C_{\mathrm{sm}}}I_0\sin(\omega t+\alpha_1) - \frac{m_1}{4C_{\mathrm{sm}}}I_2\cos(\omega t-\alpha_1+\varphi_2) - \frac{m_2}{4C_{\mathrm{sm}}}I_1\cos(\omega t+\alpha_2-\varphi_1) \quad (4.7b)$$

$$\frac{\mathrm{d}}{\mathrm{d}t}v_{\mathrm{c2}} = \frac{1}{2C_{\mathrm{sm}}}I_2\sin(2\omega t+\varphi_2) + \frac{m_1}{4C_{\mathrm{sm}}}I_1\cos(2\omega t+\alpha_1+\varphi_1) - \frac{m_2}{2C_{\mathrm{sm}}}I_0\sin(2\omega t+\alpha_2) \quad (4.7c)$$

$$\frac{\mathrm{d}}{\mathrm{d}t}v_{\mathrm{c3}} = \frac{m_1}{4C_{\mathrm{sm}}}I_2\cos(3\omega t+\alpha_1+\varphi_2) + \frac{m_2}{4C_{\mathrm{sm}}}I_1\cos(3\omega t+\alpha_2+\varphi_1). \quad (4.7d)$$

That is, each frequency component being considered in the SM capacitor voltage in (4.6) has been separated. Integrating (4.7b), (4.7c), and (4.7d) respectively yields

$$v_{\mathrm{c1}} = \frac{-1}{2\omega C_{\mathrm{sm}}}I_1\cos(\omega t+\varphi_1) + \frac{m_1}{2\omega C_{\mathrm{sm}}}I_0\cos(\omega t+\alpha_1) - \frac{m_1}{4\omega C_{\mathrm{sm}}}I_2\sin(\omega t-\alpha_1+\varphi_2) - \frac{m_2}{4\omega C_{\mathrm{sm}}}I_1\sin(\omega t+\alpha_2-\varphi_1) \quad (4.8a)$$

$$v_{\mathrm{c2}} = \frac{-1}{4\omega C_{\mathrm{sm}}}I_2\cos(2\omega t+\varphi_2) + \frac{m_1}{8\omega C_{\mathrm{sm}}}I_1\sin(2\omega t+\alpha_1+\varphi_1) + \frac{m_2}{4\omega C_{\mathrm{sm}}}I_0\cos(2\omega t+\alpha_2) \quad (4.8b)$$

$$v_{\mathrm{c3}} = \frac{m_1}{12\omega C_{\mathrm{sm}}}I_2\sin(3\omega t+\alpha_1+\varphi_2) + \frac{m_2}{12\omega C_{\mathrm{sm}}}I_1\cos(3\omega t+\alpha_2+\varphi_1). \quad (4.8c)$$

In the rotating reference frame, (4.7a) is expressed as

$$\frac{\mathrm{d}}{\mathrm{d}t}V_{\mathrm{c0}}^{\mathrm{up}} = \frac{1}{2C_{\mathrm{sm}}}I_0 - \frac{m_{1q}}{4C_{\mathrm{sm}}}I_{1q} - \frac{m_{1d}}{4C_{\mathrm{sm}}}I_{1d} - \frac{m_{2q}}{4C_{\mathrm{sm}}}I_{2q} - \frac{m_{2d}}{4C_{\mathrm{sm}}}I_{2d} \quad (4.9)$$

and will be used later in this derivation.

The second state variable is the DC component of the arm current. The dynamics of the current in the upper arm are governed by its differential equations. These are obtained upon consideration of KVL applied to the DC and AC loops of the MMC as illustrated in Fig. 4.1. It is assumed that the AC-side of the MMC consists of an R-L load. Applying KVL along

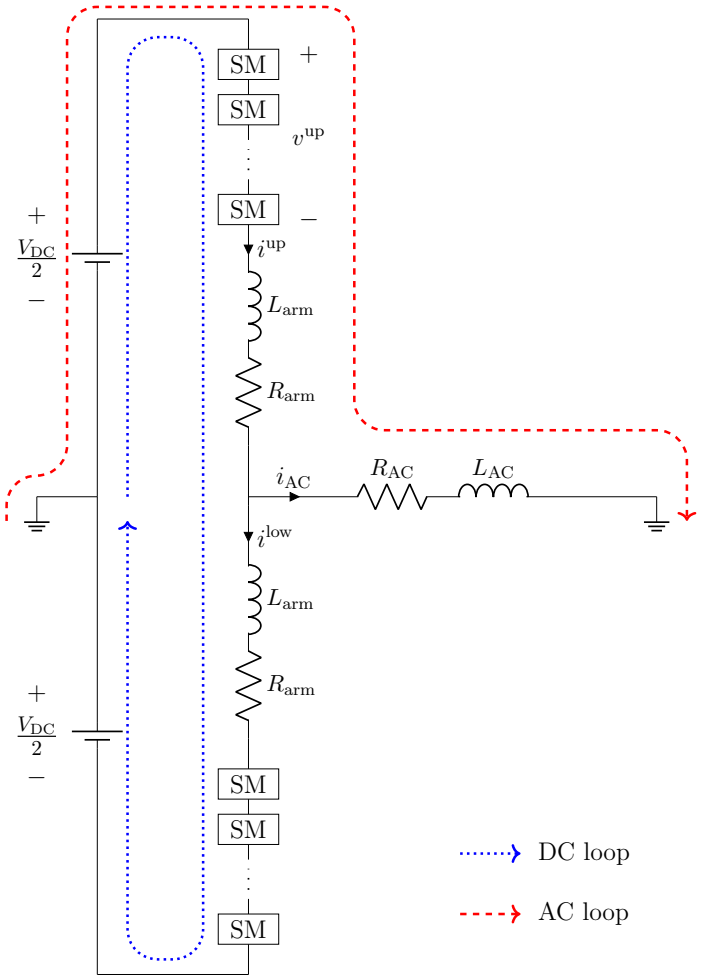

Fig. 4.1: MMC KVL paths.

the DC loop (dotted line path) yields

$$V_{\text{DC}} = v^{\text{up}} + L_{\text{arm}}\frac{\mathrm{d}}{\mathrm{d}t}i^{\text{up}} + R_{\text{arm}}i^{\text{up}} + L_{\text{arm}}\frac{\mathrm{d}}{\mathrm{d}t}i^{\text{low}} + R_{\text{arm}}i^{\text{low}} + v^{\text{low}}, \tag{4.10}$$

and applying KVL along the AC loop (dashed line path) yields

$$\frac{V_{\text{DC}}}{2} = v^{\text{up}} + L_{\text{arm}}\frac{\mathrm{d}}{\mathrm{d}t}i^{\text{up}} + R_{\text{arm}}i^{\text{up}} + R_{\text{AC}}i_{\text{AC}} + L_{\text{AC}}\frac{\mathrm{d}}{\mathrm{d}t}i_{\text{AC}}. \tag{4.11}$$

Assuming symmetric MMC operation, the upper and lower arm currents are equally distributed, so that for the even-order components [16],

$$v^{\mathrm{up}} = v^{\mathrm{low}} \tag{4.12a}$$

$$i^{\mathrm{up}} = i^{\mathrm{low}} \tag{4.12b}$$

and the load current may be expressed as

$$i_{\mathrm{AC}} = \frac{i^{\mathrm{up}}}{2}. \tag{4.13}$$

Then (4.10) can be rewritten as

$$V_{\mathrm{DC}} = 2v^{\mathrm{up}} + 2L_{\mathrm{arm}}\frac{\mathrm{d}}{\mathrm{d}t}i^{\mathrm{up}} + 2R_{\mathrm{arm}}i^{\mathrm{up}} \tag{4.14}$$

and (4.11) can be rewritten as

$$V_{\mathrm{DC}} = v^{\mathrm{up}} + L_{\mathrm{eq}}\frac{\mathrm{d}}{\mathrm{d}t}i^{\mathrm{up}} + R_{\mathrm{eq}}i^{\mathrm{up}} \tag{4.15}$$

with the equivalent inductance and resistance defined as

$$L_{\mathrm{eq}} = L_{\mathrm{arm}} + 2L_{\mathrm{AC}} \tag{4.16a}$$

$$R_{\mathrm{eq}} = R_{\mathrm{arm}} + 2R_{\mathrm{AC}}. \tag{4.16b}$$

Each frequency component in the governing differential equations for the SM voltages and arm currents is now considered separately. It must be noted that a set of λ and ξ equations

as defined in Appendix A.1 and A.2, respectively, is used to simplify the representation of the formulas in this mathematical model in the rotating reference frame throughout the rest of this derivation.

Considering only the fundamental components of (4.15) yields

$$0 = v_1^{\mathrm{up}} + L_{\mathrm{eq}} \frac{\mathrm{d}}{\mathrm{d}t} i_1^{\mathrm{up}} + R_{\mathrm{eq}} i_1^{\mathrm{up}}. \tag{4.17}$$

With balanced SM voltages and N SMs inserted at each time instant,

$$v_1^{\mathrm{up}} = \{ N m^{\mathrm{up}} (V_{c0} + v_{c1} + v_{c2} + v_{c3}) \}_1 \tag{4.18}$$

where the $\{\}_1$ notation denotes that only the fundamental-frequency components inside the $\{\}$ brackets are taken. Equation (4.2) is first substituted into (4.3), then with (4.8a), (4.8b), and (4.8c) into (4.18), and lastly into (4.17). Applying standard trigonometric identities, equating the $\sin(\omega t)$ and $\cos(\omega t)$ terms and simplifying yields two equations of the form

$$\lambda_1 V_{c0} + \lambda_2 I_0 + \lambda_3 I_{1q} + \lambda_4 I_{1d} + \lambda_5 I_{2q} + \lambda_6 I_{2d} = 0 \tag{4.19a}$$

$$\lambda_7 V_{c0} + \lambda_8 I_0 + \lambda_9 I_{1q} + \lambda_{10} I_{1d} + \lambda_{11} I_{2q} + \lambda_{12} I_{2d} = 0 \tag{4.19b}$$

in the $dq0$ domain where (4.19a) are from the $\sin(\omega t)$ terms and (4.19b) are from the $\cos(\omega t)$ terms.

In a similar manner, considering only the second harmonic components in (4.14)

$$0 = 2v_2^{\mathrm{up}} + 2L_{\mathrm{arm}} \frac{\mathrm{d}}{\mathrm{d}t} i_2^{\mathrm{up}} + 2R_{\mathrm{arm}} i_2^{\mathrm{up}}. \tag{4.20}$$

With balanced SM voltages and N SMs inserted at each time instant,

$$v_2^{\text{up}} = \{Nm^{\text{up}}(V_{c0} + v_{c1} + v_{c2} + v_{c3})\}_2 \tag{4.21}$$

where the $\{\}_2$ notation denotes that only the second-order frequency components inside the $\{\}$ brackets are taken. Equation (4.2) is first substituted into (4.3), then with (4.8a), (4.8b), and (4.8c) into (4.21), and lastly into (4.20). Applying standard trigonometric identities, equating the $\sin(2\omega t)$ and $\cos(2\omega t)$ terms and simplifying yields two equations of the form

$$\lambda_{13}V_{c0} + \lambda_{14}I_0 + \lambda_{15}I_{1q} + \lambda_{16}I_{1d} + \lambda_{17}I_{2q} + \lambda_{18}I_{2d} = 0 \tag{4.22a}$$

$$\lambda_{19}V_{c0} + \lambda_{20}I_0 + \lambda_{21}I_{1q} + \lambda_{22}I_{1d} + \lambda_{23}I_{2q} + \lambda_{24}I_{2d} = 0 \tag{4.22b}$$

in the $dq0$ domain where (4.22a) are from the $\sin(2\omega t)$ terms and (4.22b) are from the $\cos(2\omega t)$ terms.

Lastly, considering only the DC components in (4.14),

$$V_{\text{DC}} = 2v_0^{\text{up}} + 2L_{\text{arm}}\frac{\text{d}}{\text{d}t}I_0 + 2R_{\text{arm}}I_0 \tag{4.23}$$

and with balanced SM voltages and N SMs inserted at each time instant,

$$v_0^{\text{up}} = \{Nm^{\text{up}}(V_{c0} + v_{c1} + v_{c2} + v_{c3})\}_0 \tag{4.24}$$

where the $\{\}_0$ notation denotes that only the DC components inside the $\{\}$ brackets are taken. Equation (4.2) is first substituted into (4.3), then with (4.8a), (4.8b), and (4.8c) into (4.24), and next into (4.23). Applying standard trigonometric identities and simplifying

yields

$$\frac{\mathrm{d}}{\mathrm{d}t}I_0 = \xi_5 V_{\mathrm{DC}} - \frac{R_{\mathrm{arm}}}{L_{\mathrm{arm}}}I_0 + \frac{N}{2L_{\mathrm{arm}}}V_{\mathrm{c0}} + \frac{\lambda_2}{2L_{\mathrm{arm}}}I_{1q} + \frac{\lambda_8}{2L_{\mathrm{arm}}}I_{1d} + \frac{\lambda_{14}}{2L_{\mathrm{arm}}}I_{2q} + \frac{\lambda_{20}}{2L_{\mathrm{arm}}}I_{2d}. \quad (4.25)$$

At this point, the state equations for the DC components of the SM voltages and arm currents have been obtained, but not yet fully simplified. It is first noted that (4.19a), (4.19b), (4.22a), and (4.22b) constitute a system of equations and the expressions for I_{1q}, I_{1d}, I_{2q} and I_{2d} may be solved for in terms of V_{c0} and I_0. The general form for the given system is

$$\begin{bmatrix} \lambda_3 & \lambda_4 & \lambda_5 & \lambda_6 \\ \lambda_9 & \lambda_{10} & \lambda_{11} & \lambda_{12} \\ \lambda_{15} & \lambda_{16} & \lambda_{17} & \lambda_{18} \\ \lambda_{21} & \lambda_{22} & \lambda_{23} & \lambda_{24} \end{bmatrix} \begin{bmatrix} I_{1q} \\ I_{1d} \\ I_{2q} \\ I_{2d} \end{bmatrix} + \begin{bmatrix} \lambda_1 \\ \lambda_7 \\ \lambda_{13} \\ \lambda_{19} \end{bmatrix} V_{\mathrm{c0}} + \begin{bmatrix} \lambda_2 \\ \lambda_8 \\ \lambda_{14} \\ \lambda_{20} \end{bmatrix} I_0 = \begin{bmatrix} 0 \\ 0 \\ 0 \\ 0 \end{bmatrix}. \quad (4.26)$$

The expressions for I_{1q}, I_{1d}, I_{2q} and I_{2d} in terms of V_{c0} and I_0 are then substituted into (4.9) and (4.25) and expressed in a state-space form:

$$\frac{\mathrm{d}}{\mathrm{d}t}\begin{bmatrix} V_{\mathrm{c0}} \\ I_0 \end{bmatrix} = \begin{bmatrix} \xi_1 & \xi_2 \\ \xi_3 & \xi_4 \end{bmatrix} \begin{bmatrix} V_{\mathrm{c0}} \\ I_0 \end{bmatrix} + \begin{bmatrix} 0 \\ \xi_5 \end{bmatrix} V_{\mathrm{DC}}. \quad (4.27)$$

It must be noted that while there are 24 λ terms, only 16 of these are distinct when the modulation reference waveform considers the fundamental and second-order frequency components. Furthermore, if only the fundamental-frequency component is considered, only 12 distinct λ terms need to be calculated (Appendix A.1.1). The reason for presenting 24 λ terms is to maintain the flexibility of the model. In this form, not only can these two cases be considered without any changes in the formulations, but also if the modulation reference

waveform were to include other harmonics for example, the additions to the model are minor. Only the differential equation for the SM voltage (4.9) needs to be expanded if (4.2) does not include all of the desired terms. Similarly, if the system topology were to change, only the differential equation for the arm current needs to be updated. The equations for the AC components simply need to have the same form as (4.19a), (4.19b), (4.22a), and (4.22b), so that a system of equations for I_{1q}, I_{1d}, I_{2q} and I_{2d} in terms of V_{c0} and I_0 similar to (4.26) may be constructed and solved in the same manner as presented.

In (4.27), there are two coupled first-order differential equations. The response time of this type of mathematical system is measurable by a time constant, which is derived from the real part of its eigenvalues. Input variables will not impact the system eigenvalues; therefore, only the matrix with the ξ terms needs to be considered. Considering under-damped cases where

$$4(\xi_1\xi_4 - \xi_2\xi_3) > (\xi_1 + \xi_4)^2 \tag{4.28}$$

which will be held for small resistances as is typically the case, its two eigenvalues are complex conjugate pairs and, therefore, have the same real part. The time constant may then be expressed as

$$\tau = -\frac{2}{\xi_1 + \xi_4} \tag{4.29}$$

where the settling time is typically 3τ to 5τ. Equation (4.29) therefore provides an estimation of the response time of the MMC and can be obtained analytically. This means that the response time of the MMC may be determined without the computational cost of circuit simulations or iterative calculations.

4.2 Validation of Mathematical Model

A simulation case in PSCAD/EMTDC is designed and set up in order to validate the model. An MMC is connected to a resistive load and the operation of the MMC is controlled using PQ and CCSC schemes. Symmetric operation with a constant DC-side source is assumed. Perturbations are applied to the DC-side voltage to study the DC responses of the SM voltages in the MMC.

Table 4.1: MMC System Parameters

Parameter	**Value**
Output power P_{AC}	150 [MW]
Rated DC voltage V_{DC}	200 [kV]
Number of submodules per arm N	80
Submodule capacitance C_{sm}	4000 [μF]
Arm inductance L_{arm}	50 [mH]
Arm resistance R_{arm}	1 [Ω]
Load resistance R_{AC}	80.17 [Ω]

Although the main purpose of the model is to provide a time constant for the settling time of the SM voltage and arm current's DC components, the model is also able to reconstruct the AC components of the waveforms from their DC dynamics. This capability is used to validate the accuracy of the model. With the AC components, it also means that the control systems can be integrated with the simulation. In Fig. 4.2, the SM voltage, arm current, and power responses from the model are compared against those simulated from PSCAD/EMTDC. The meaning of average in the legend is that only the DC components are considered for the model, and a moving average with a centered window of one cycle length at 60 Hz is applied for the PSCAD waveforms. Each case includes the PQ control scheme, and CCSC scheme if

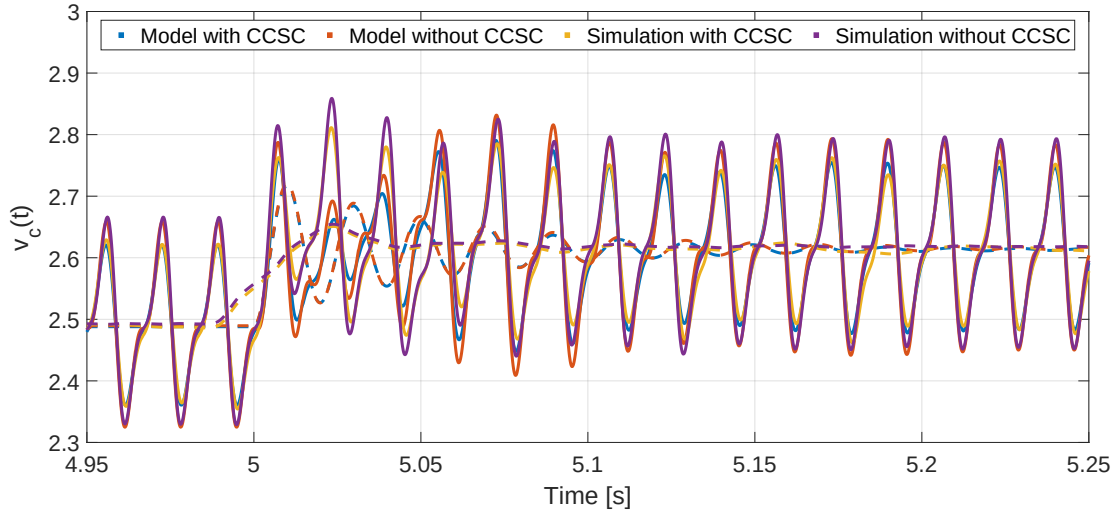

(a)

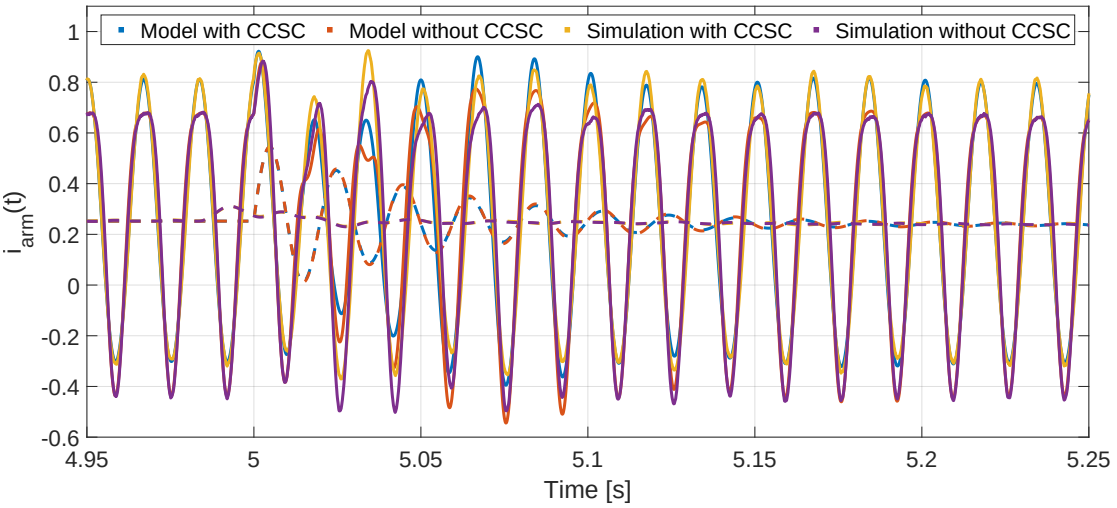

(b)

Fig. 4.2: Comparison of responses from the model and PSCAD/EMTDC simulation to a +5% change in V_{DC} with $C_{\mathrm{sm}} = 4000$ μF and $L_{\mathrm{arm}} = 50$ mH for (a) SM voltage [kV] and (b) arm current [kA] responses where the solid lines are the full waveform, and the dashed lines are the averaged waveform, and (c) power [MW] responses where the solid lines are when with CCSC, and the dashed lines are when without CCSC. (Continued on next page)

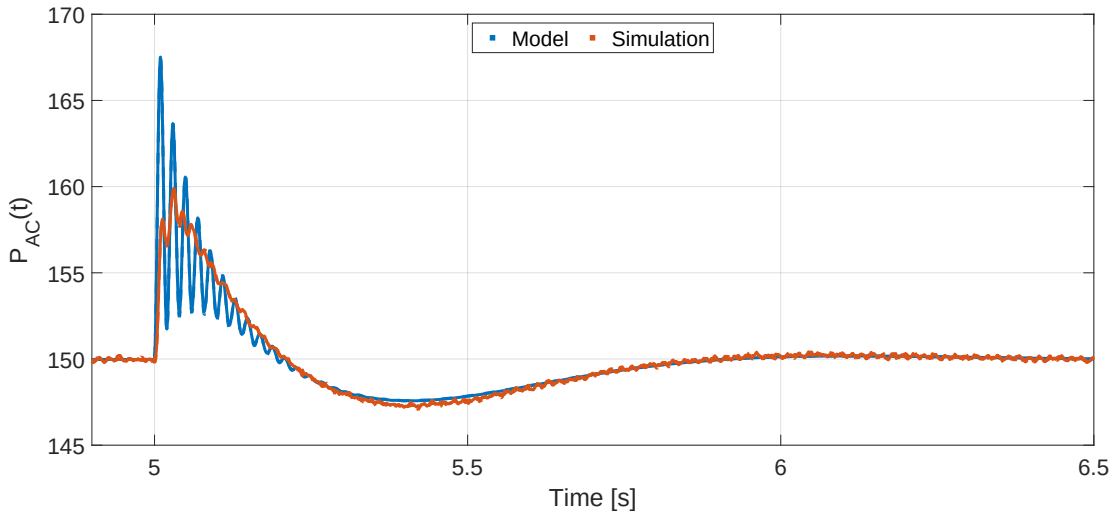

(c)

Fig. 4.2: (Continued from previous page) Comparison of responses from the model and PSCAD/EMTDC simulation to a +5% change in V_{DC} with $C_{sm} = 4000$ μF and $L_{arm} = 50$ mH for (a) SM voltage [kV] and (b) arm current [kA] responses where the solid lines are the full waveform, and the dashed lines are the averaged waveform, and (c) power [MW] responses where the solid lines are when with CCSC, and the dashed lines are when without CCSC.

specified (solid line).

It can first be seen that the DC components represented by the model capture the moving average of the PSCAD/EMTDC simulated waveforms. However, the advantage of using the model to simulate the DC components is that the waveform does not need to be known in advance. In PSCAD/EMTDC, the moving average cannot use a centered window because the signal is causal. If the average were being captured in real time, there would be a time delay because a backward window must be used. The model does not have this limitation. It can also be seen that the AC components are sufficiently captured. Since control systems based on the AC component values at each time step were included, this validates the model accuracy and demonstrates its ability to simulate the waveforms. It is noted that the model does not capture as much detail as the simulated waveforms. This is consequent of the model

not considering harmonics greater than the second order.

It is particularly evident in the arm currents (Fig. 4.2b) that the CCSC scheme handles the second harmonic current properly, since when CCSC is active, the second harmonic current becomes significantly less. It can be seen that CCSC does not have a significant impact on the settling time. This is because the magnitude of the second harmonic injected into the modulation reference waveform is small compared to the fundamental component. If the modulation reference waveform were to have a strong impact on the settling time, it should therefore be the fundamental modulation index that is studied.

The limitation of the model is demonstrated by repeating this simulation case but with a lower arm inductance. The arm inductance L_{arm} is now decreased to 15 mH (0.09 pu using base values of 200 MVA and 110 kV) from the previous value of 50 mH (0.31 pu). The accuracy of the model in reconstructing the AC components is largely dependent on the relative size of the AC transients to the DC transients. This is consequent of the model basis and it means that with more significant AC components, the model accuracy decreases as demonstrated in Fig. 4.3. With a lower arm inductance, the AC transients are now more prominent than before. The model is no longer able to capture the AC components of the waveforms to the same degree of accuracy. Nevertheless, the DC component still sufficiently captures the moving average of the simulated waveforms, and this is the primary importance. It must be recalled and emphasized that the main purpose of the model is to provide an estimate for the settling time of the SM voltage and arm current DC components. As the model still fulfills this purpose - even if it cannot always capture the AC dynamics - the formulations are still valid. This is consistent with the merit that the model does not need any waveform simulation to provide the settling time constant.

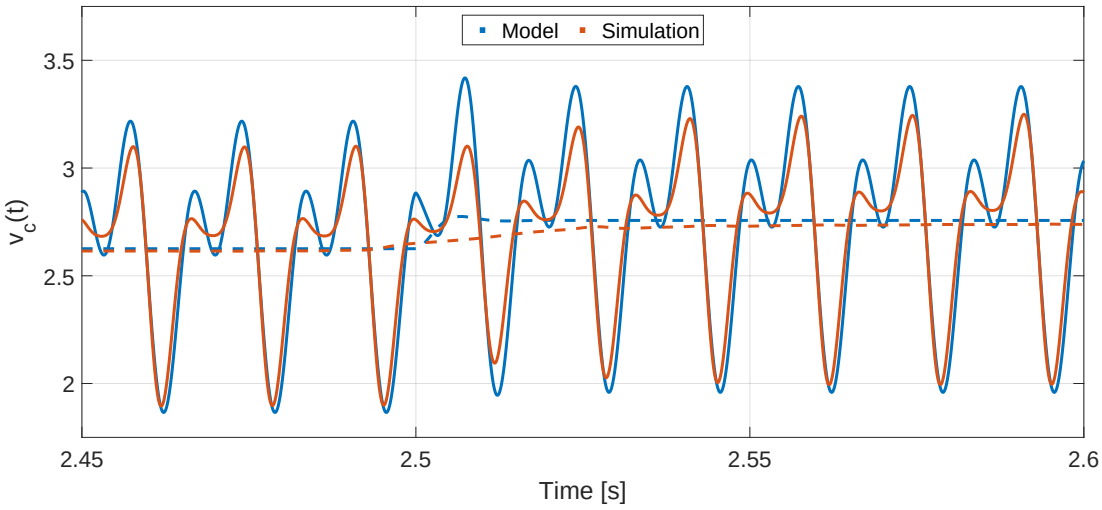

(a)

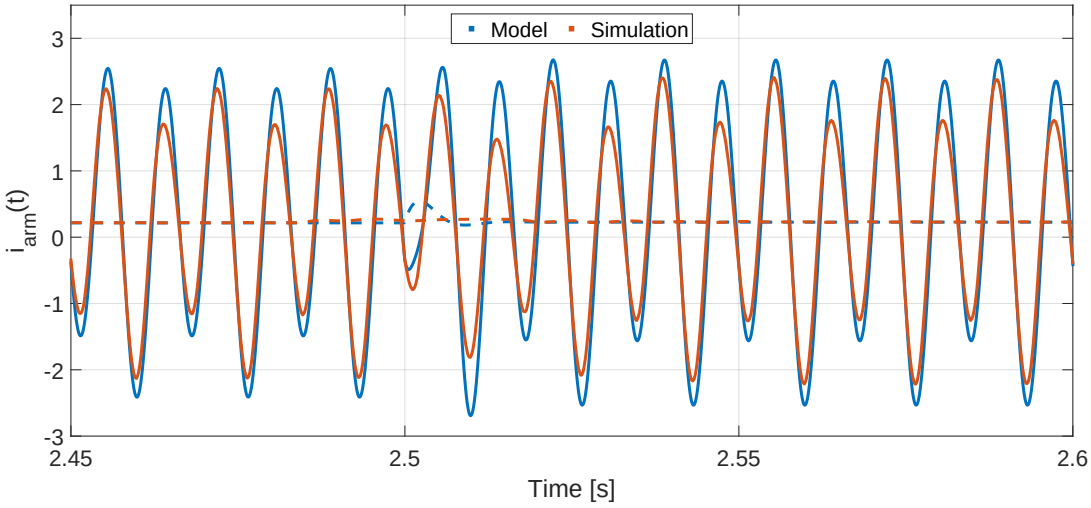

(b)

Fig. 4.3: Comparison of responses from the model and PSCAD/EMTDC simulation to a +5% change in V_{DC} with $C_{\mathrm{sm}} = 4000$ μF and $L_{\mathrm{arm}} = 15$ mH for (a) SM voltage [kV] and (b) arm current [kA] responses where the solid lines are the full waveform, and the dashed lines are the averaged waveform, and (c) power [MW] responses. (Continued on next page)

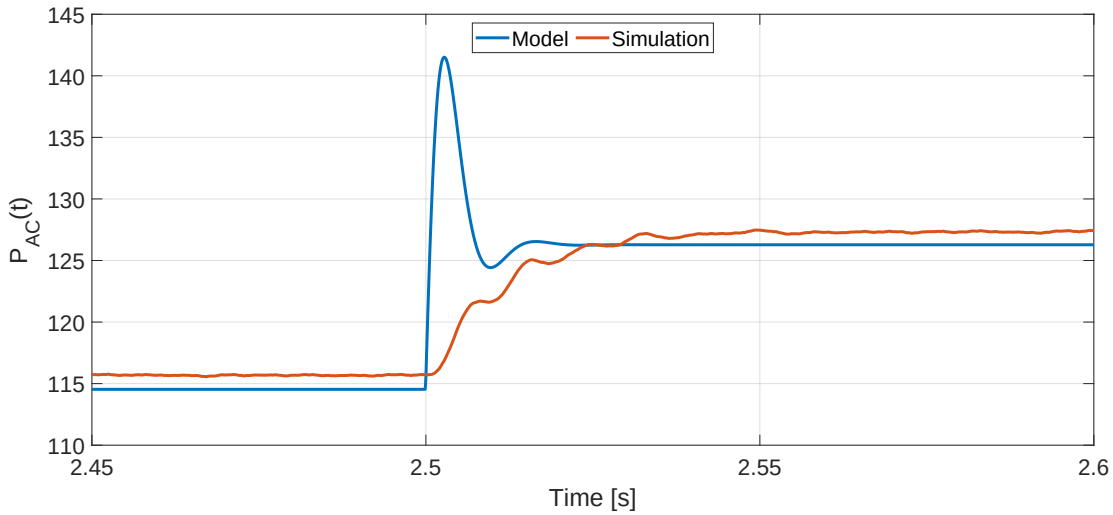

(c)

Fig. 4.3: (Continued from previous page) Comparison of responses from the model and PSCAD/EMTDC simulation to a +5% change in V_{DC} with $C_{\mathrm{sm}} = 4000$ μF and $L_{\mathrm{arm}} = 15$ mH for (a) SM voltage [kV] and (b) arm current [kA] responses where the solid lines are the full waveform, and the dashed lines are the averaged waveform, and (c) power [MW] responses.

4.2.1 Settling Time Extraction Algorithms

The settling time obtained from simulation needs to be arithmetically extracted from the waveforms in order to perform quantitative comparisons between the model's predictions and PSCAD/EMTDC simulations. Two particular approaches are considered: one based on the DC components as in the model, and one based on the full waveform.

4.2.1.1 DC-Based Extraction

The idea of this extraction algorithm is to observe the moving average (centered window) of the simulated waveform. When the moving average has settled, the waveform is considered as settled. However, if different SM capacitances are tested, there may be an impact on the measured settling time. This is because the SM voltage ripple generally decreases with

increasing SM capacitance. In calculating the moving average, with a smaller ripple, the measured settling time may be incorrectly underestimated. Similarly, with a larger ripple, the measured settling time may be incorrectly overestimated. The concern for this arises because all test cases should have the same tolerance rules for waveform settling in order to maintain consistency.

4.2.1.2 Full-Waveform-Based Extraction

The idea of this extraction algorithm is to observe the full simulated waveform, rather than only the DC component. The waveform is considered as settled when it reaches periodic steady-state (within a specified tolerance). With this settling condition, a variance in the SM voltage ripple will not have a significant impact on the measured settling time as with the DC-based extraction method. At each time-step, the algorithm looks three cycles ahead and compares to the three cycles from the previous time-step. These are compared using a circular shift, because if the waveform has settled, there should be a shift where these two data sequences are the same within a tolerance. Three cycles are used in order to take into account outliers (anomalies) where the waveform seemed to have settled, but suddenly needs more time to settle according to the set tolerance due to switching transients for instance.

4.3 Parametric Study on Response Speed

In this section, parametric analyses are conducted to investigate the MMC's settling time under different sizing and operating conditions. The primary design variable is the SM capacitance C_{sm} because it is the main energy storage element in the MMC. The secondary design variables include the arm inductance L_{arm}, the modulation index m, and the load

power factor. The observation variable is the settling time of the SM voltages upon a perturbation, which is predicted using the derived mathematical model and compared against detailed PSCAD/EMTDC simulations. This definition provides insight on how the electrical components and operating point of an MMC affect its response speed, which is an important factor to consider when implementing energy control. Each parametric analysis is described in a separate subsection in the same aforementioned order.

4.3.1 SM Capacitance and Arm Inductance

The test system is run as described in Section 4.2 with the SM capacitance C_{sm} and arm inductance L_{arm} varied parametrically. The values used for these two variables are tabulated in Table 4.2. The modulation index is fixed at 0.9 and the load is at unity power factor.

Table 4.2: Values used in SM Capacitance and Arm Inductance Parametric Analysis

$\boldsymbol{C_{\text{sm}}}$ **[μF]**	4000	4800	5600	6400	7200	8000
$\boldsymbol{L_{\text{arm}}}$ **[mH]**	15	20	25	30	35	40

Using the derived model, a time constant τ for the DC component of the SM voltage is obtained for each parametric case. This is used to set the upper and lower bounds of the predicted settling time of the full waveform. The measured settling time is obtained through data processing of the detailed PSCAD/EMTDC simulations for each parametric case using the full-waveform-based extraction algorithm. Different perturbation levels in the DC-side voltage of the MMC are also tested. These results are shown in Fig. 4.4. Each graph contains three surface plots. The two surface plots of lower opacity outlined in red and magenta represent three and five time constants, respectively, as determined by the mathematical model. This provides an estimated range for the actual settling time of the waveforms, which

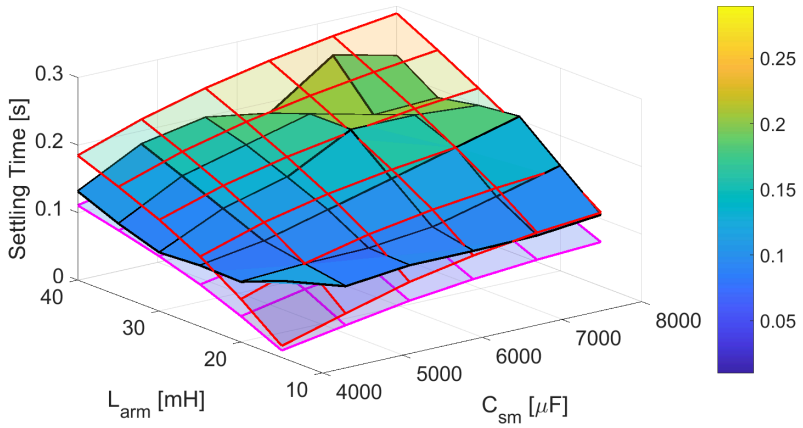

(a)

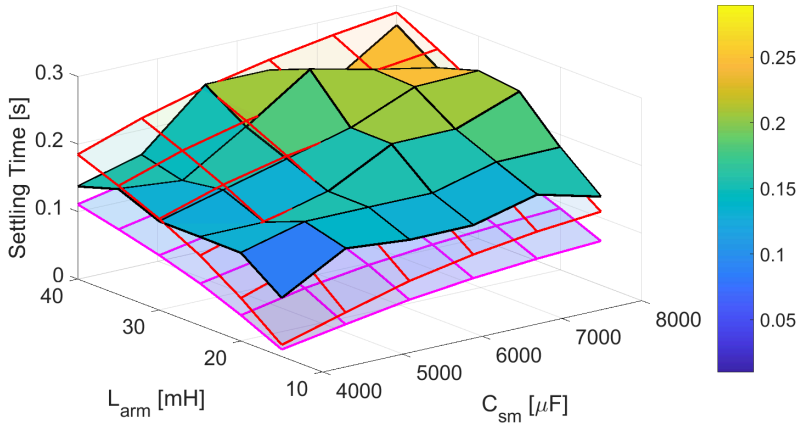

(b)

Fig. 4.4: SM voltage settling times with perturbation of (a) +5% (b) −10% (c) +2% change in V_{DC} for SM capacitance and arm inductance parametric analysis. Time bounds predicted by model in lower opacity, measured time in higher opacity. (Continued on next page)

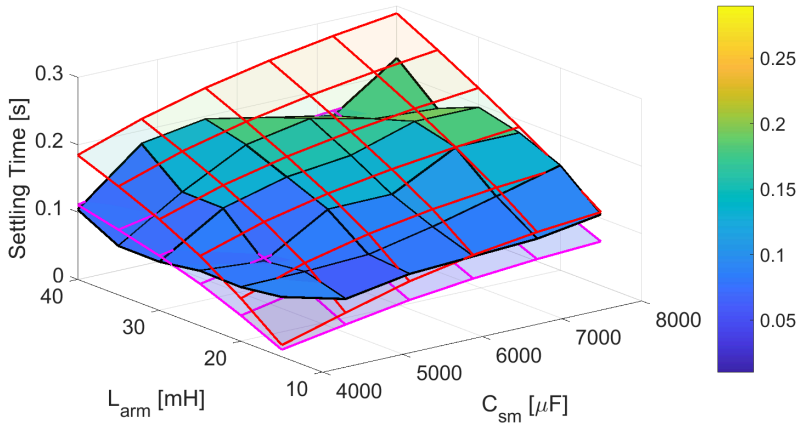

(c)

Fig. 4.4: (Continued from previous page) SM voltage settling times with perturbation of (a) +5% (b) −10% (c) +2% change in V_{DC} for SM capacitance and arm inductance parametric analysis. Time bounds predicted by model in lower opacity, measured time in higher opacity.

are plotted in higher opacity. If the highest opacity surface plot falls between the two lower opacity surface plots, it means that the model has successfully approximated the settling time.

The general trend observed is that increasing either the SM capacitance or arm inductance increases the settling time of the waveform. This is consequent of the inherent properties of these energy storage elements and is to be expected. The decreased $\frac{di}{dt}$ (by inductors) and $\frac{dv}{dt}$ (by capacitors) capabilities contribute to the slow down. It is important to note that the increments on the arm inductance are an order of magnitude higher than the increments on the SM capacitance. The resulting increase in settling time, however, does not have a difference of an order of magnitude. Furthermore, as the arm inductance increases, the effect from the SM capacitance increases. In other words, the impact these two components have on the MMC response time is not completely decoupled. This means that in selecting the SM capacitance with the consideration of the response speed, the arm inductance is also an

important factor to account for.

The validity of the model predictions are quantitatively evaluated against the measured settling times. The error t_{error} is quantified by how much the measured settling time t_{meas} is outside the bounds predicted by the mode, which may be represented by

$$t_{\text{error}} = \begin{cases} t_{\text{meas}} - 3\tau & \text{if } t_{\text{meas}} < 3\tau \\ t_{\text{meas}} - 5\tau & \text{if } t_{\text{meas}} > 5\tau \\ 0 & \text{otherwise.} \end{cases} \tag{4.30}$$

That is, the three possibilities are that the measured settling time t_{meas} is either (i) less than the lower bound, (ii) more than the upper bound, or (iii) inside the bounds predicted by the model. In the first case, the error will be negative to represent that the settling time was shorter than anticipated. In the second case, the error will be positive to represent that the settling time was longer than anticipated. If neither of these two cases is true, then the settling time was within the range predicted by the model and the error is quantified as zero.

An error analysis is conducted for each parametric case and shown in Fig. 4.5. It can be seen in the plots that the model accuracy depends on at least two factors: the magnitude of the perturbation and the SM voltage ripple. The former is evident across the different perturbations (Figures 4.5a, 4.5b, and 4.5c). The measured settling time is within the bounds predicted by the model for the majority of the parametric cases for the 5% and 2% perturbations. However, with the larger 10% perturbation, there are more cases in which the error is positive. The measured settling time is longer than predicted and this is because the system may need more than five time constants to settle to the same level as the smaller perturbations. Some error could also be attributed to the measurement, since the measurement

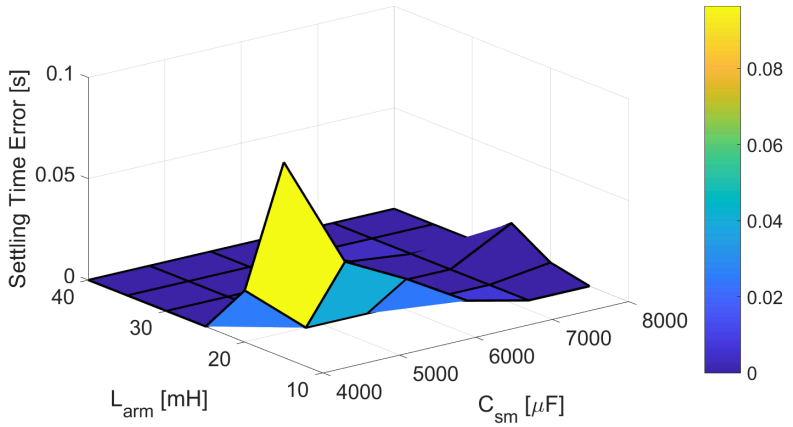

(a)

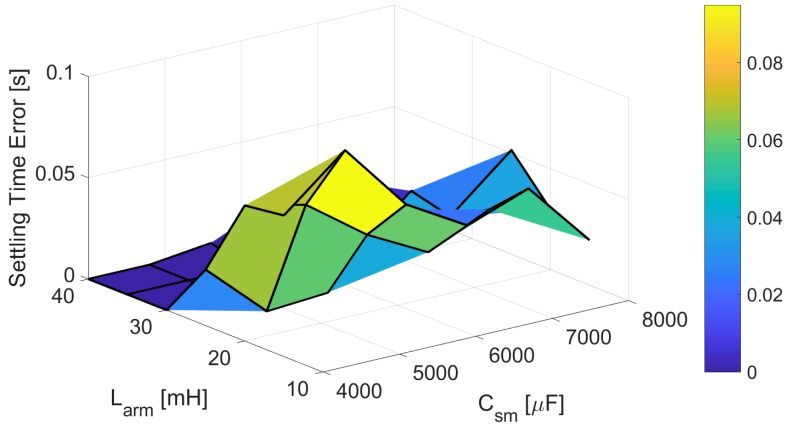

(b)

Fig. 4.5: Error of model SM voltage settling times subjected to a perturbation of (a) +5% (b) −10% (c) +2% change in V_{DC} for the SM capacitance and arm inductance parametric analysis considering (d) peak-to-peak SM voltage ripple. (Continued on next page)

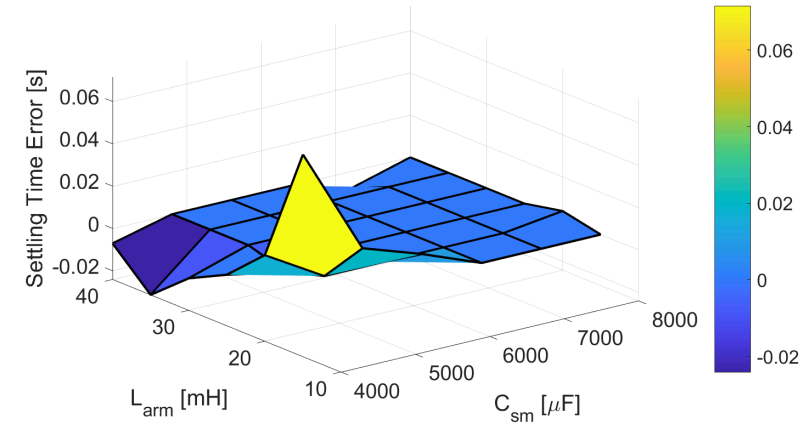

(c)

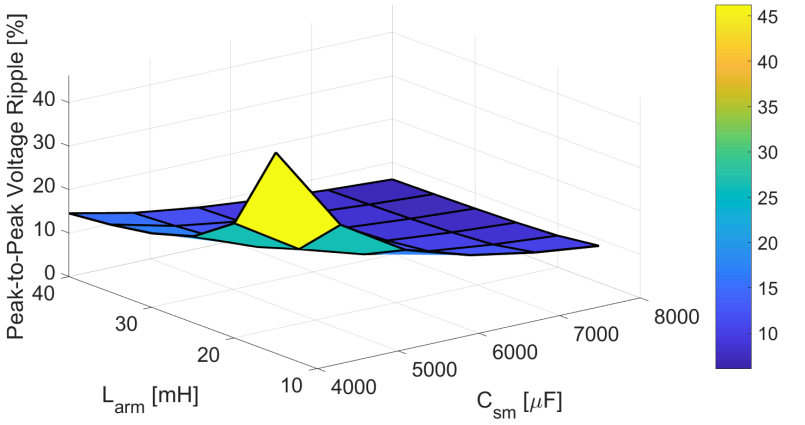

(d)

Fig. 4.5: (Continued from previous page) Error of model SM voltage settling times subjected to a perturbation of (a) +5% (b) −10% (c) +2% change in V_{DC} for the SM capacitance and arm inductance parametric analysis considering (d) peak-to-peak SM voltage ripple.

observes the full cycle of the waveform, and not only the DC component like the model. That is, some AC transients which are not fully accounted for in the model might be extending the settling time of the full waveform.

The SM voltage ripple, as shown in Fig. 4.5d, may also affect the model accuracy. The general trend is that as the ripple decreases, the model is more accurate. This is consistent with the implicit model assumption that the AC transients are not significant compared to the DC transients. It is noted, however, that for the 10% perturbation case, there are some parametric cases that have more error despite having a smaller ripple. This behaviour may be attributed back to the longer settling time due to a larger perturbation.

4.3.2 SM Capacitance and Modulation Index

In this section, the SM capacitance C_{sm} and modulation index m are varied in a parametric manner. At a fixed operating point, the modulation reference waveform is fixed and only the fundamental component is considered here. The arm inductance is fixed at 15 mH and the load power factor is unity across all parametric cases. The values used for these two variables are tabulated in Table 4.3. As before, the model is used to predict a range for the settling

Table 4.3: Values used in SM Capacitance and Modulation Index Parametric Analysis

$\boldsymbol{C_{\text{sm}}}$ $[\boldsymbol{\mu}\mathbf{F}]$	4000	4800	5600	6400	7200	8000
$\boldsymbol{m}$	0.75	0.8	0.85	0.9	0.95	1

time and is validated against the settling time obtained from detailed PSCAD/EMTDC simulations for each parametric case. These results are shown in Fig. 4.6. The same set of perturbations on the DC-side voltage of the MMC are tested. Each graph contains three surface plots following the same previous conventions. It is shown that the modulation index

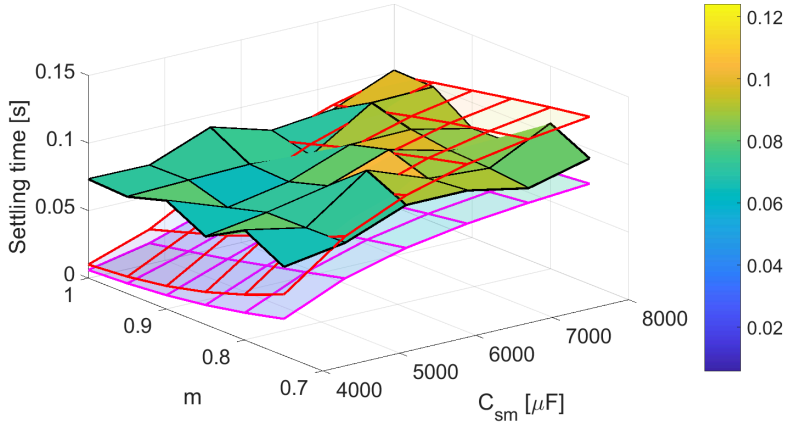

(a)

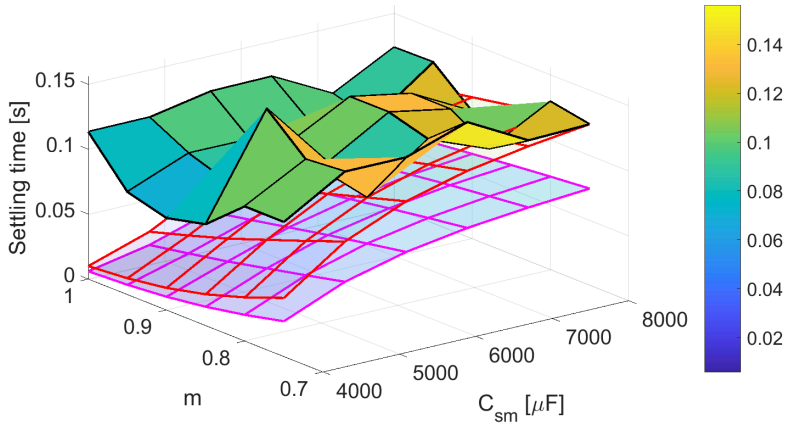

(b)

Fig. 4.6: SM voltage settling times with perturbation of (a) +5% (b) −10% (c) +2% change in V_{DC} for SM capacitance and modulation index parametric analysis. Time bounds predicted by model in lower opacity, measured time in higher opacity. (Continued on next page)

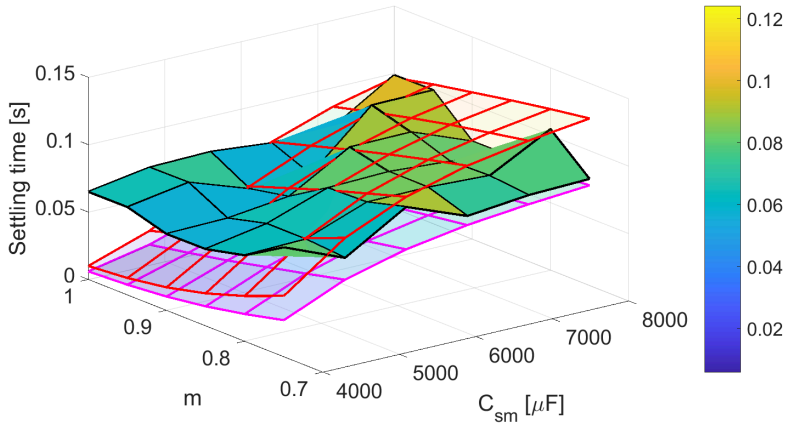

(c)

Fig. 4.6: (Continued from previous page) SM voltage settling times with perturbation of (a) +5% (b) −10% (c) +2% change in V_{DC} for SM capacitance and modulation index parametric analysis. Time bounds predicted by model in lower opacity, measured time in higher opacity.

does not have a significant impact on the settling time. This is supported by both the model and the acquired measurements. There is little variation in the settling times due to variations in the modulation index than variations in the inductance or capacitance. The same can be interpreted intuitively by considering that the modulation index is less inherent to an MMC than the sizing of its components, and therefore comparatively has less dominance in the natural response. This means in the interest of the settling time, the modulation index is not necessarily a primary factor of consideration.

To verify these results, an error analysis is conducted for each parametric case as before and shown in Fig. 4.7. As explained previously, the magnitude of the perturbation and the SM voltage ripple affect the model accuracy. The same behaviour regarding these two factors is seen again. However, compared to the parametric study with the arm inductance, there are more cases with error and the upper bound on the error is higher. This is because the SM voltage ripple is more significant in this parametric study as shown in Fig. 4.7d, and suggests

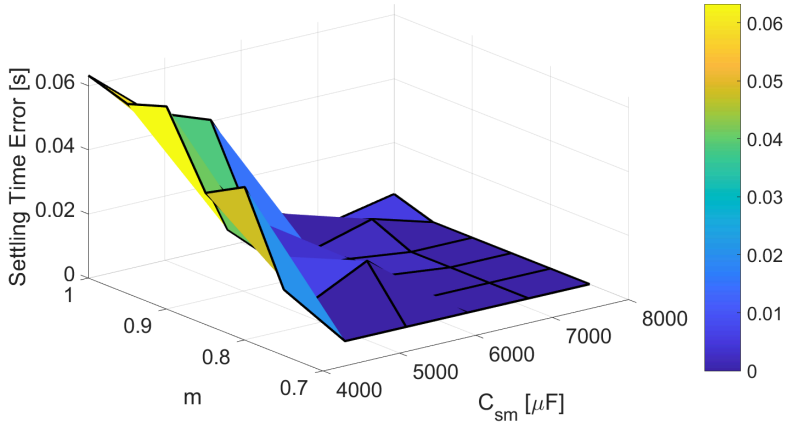

(a)

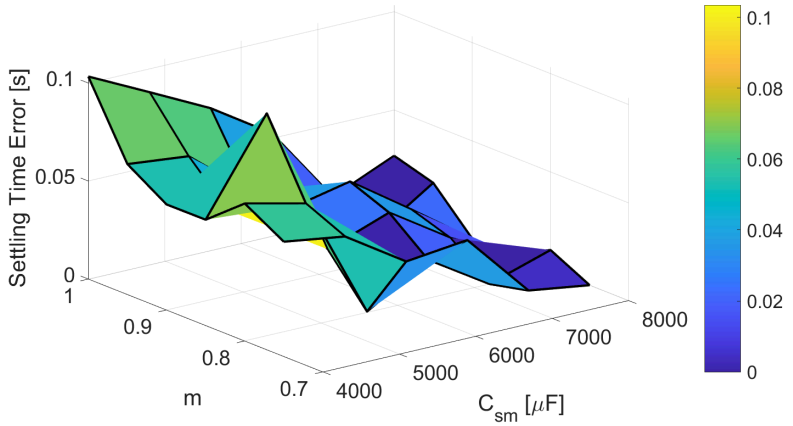

(b)

Fig. 4.7: Error of model SM voltage settling times subjected to a perturbation of (a) +5% (b) −10% (c) +2% change in V_{DC} for the SM capacitance and modulation index parametric analysis considering (d) peak-to-peak SM voltage ripple. (Continued on next page)

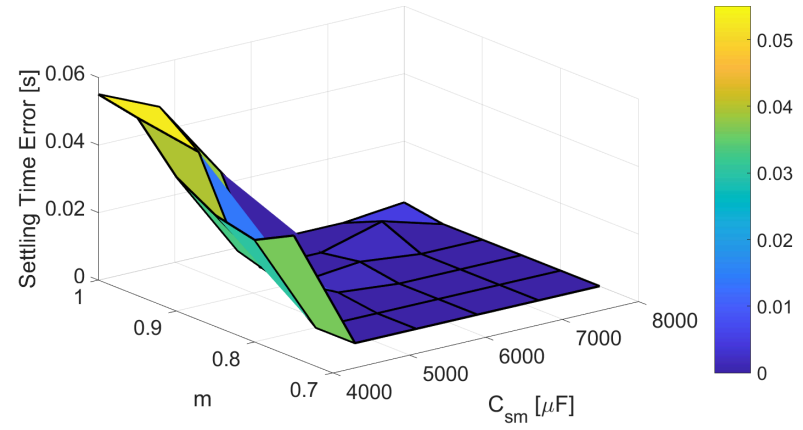

(c)

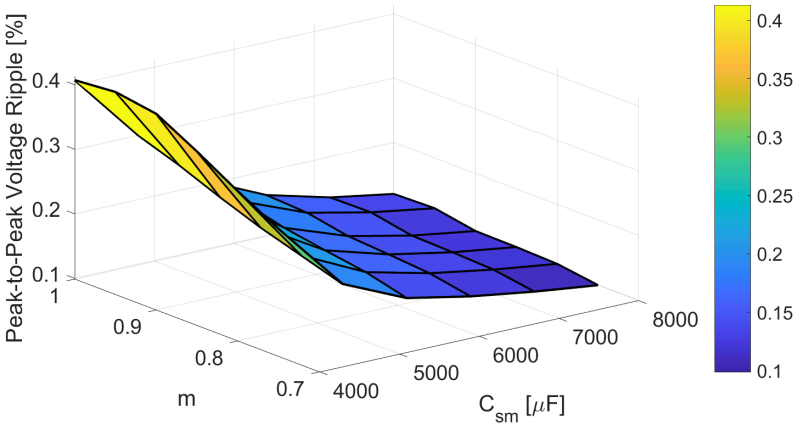

(d)

Fig. 4.7: (Continued from previous page) Error of model SM voltage settling times subjected to a perturbation of (a) +5% (b) −10% (c) +2% change in V_{DC} for the SM capacitance and modulation index parametric analysis considering (d) peak-to-peak SM voltage ripple.

that while the modulation index does not greatly affect the settling time, it plays a role in determining the SM voltage ripple. This is particularly true when the SM capacitance is lower. At the same time, the SM voltage ripple is higher than the parametric study with the arm inductance because there the arm inductance is fixed and at a lower value. Therefore, when the MMC is operating at a large modulation index, careful consideration should be taken against the ripple.

4.3.3 SM Capacitance and Load Power Factor

In this section, the SM capacitance C_{sm} and load power factor are varied in a parametric manner. The same test system as was described in Section 4.2 is still being used. The values used for these two variables are tabulated in Table 4.4. This range of power factors is selected to be consistent with the typical operating points of an MMC. The load is of type R-L and the magnitude of the impedance is fixed across all parametric cases. This means that the proportion of impedance from resistance and reactance must be varied to achieve different load power factors. An R-L load is used to because it is representative of a typical load that an MMC would be connected to in a power system. Each set of R-L values is computed and tabulated in Table 4.5. The modulation index and arm inductance are fixed at 0.9 and 15 mH respectively across all cases.

Table 4.4: Values used in SM Capacitance and Load Power Factor Parametric Analysis

$\boldsymbol{C_{\text{sm}}}$ **[μF]**	4000	4800	5600	6400	7200	8000	
Power Factor	0.7	0.75	0.8	0.85	0.9	0.95	1

Once again, the model is used to predict a range for the settling time and is validated against the settling time obtained from detailed PSCAD/EMTDC simulations for each para-

Table 4.5: Values of Load Components for Different Power Factors

Power Factor	0.7	0.75	0.8	0.85	0.9	0.95	1
$\boldsymbol{R_{AC}}$ **[Ω]**	56.4667	60.5000	64.5333	68.5667	72.6000	76.6333	80.6667
$\boldsymbol{L_{AC}}$ **[mH]**	0.1528	0.1415	0.1284	0.1127	0.0933	0.0668	0

metric case subjected to the same set of perturbations on the DC-side voltage of the MMC. These results are shown in Fig. 4.8. Each graph contains three surface plots following the same previous conventions, and indicate that the load power factor does not have a significant impact on the settling time. Although a lower factor means that the load is more inductive, this may not significantly affect the settling time predicted by the model because it is on the AC-side of the MMC. The time constant derived from the model is only based on the transients of the DC components. While there are more cases in which the measured settling time is closer to the upper bounds predicted by the model, this may not be attributed to the load power factor as the both the modelled and simulated settling times indicate relatively constant values across different power factors. It must be noted that as per Table 4.5, the load inductance across the different power factors does not vary greatly, which is consistent with the little observed changes in the settling times. This draws the conclusion back to the first parametric study that besides the SM capacitance, the arm inductance generally holds dominance in determining the MMC response speed.

The error analysis is conducted for each parametric case as before and shown in Fig. 4.9. The same errors that can be attributed to the magnitude of the perturbation and the SM voltage ripple affect the model accuracy are evident. As can be seen and previously mentioned, there are more cases in which the measured settling time is closer to the upper bounds predicted by the model with larger perturbations. Fig. 4.9c which is the case with

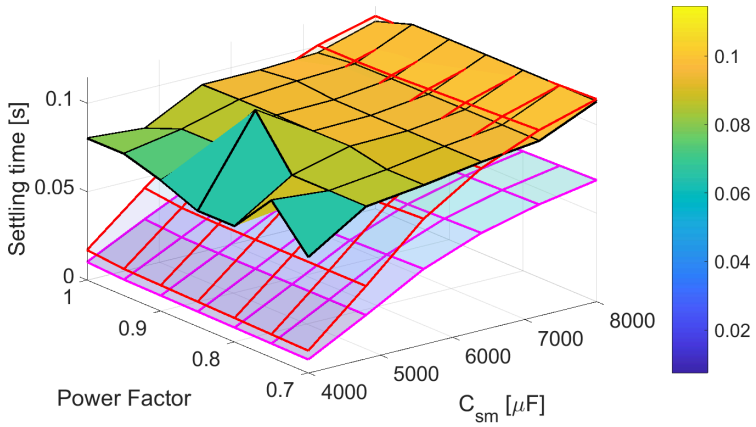

(a)

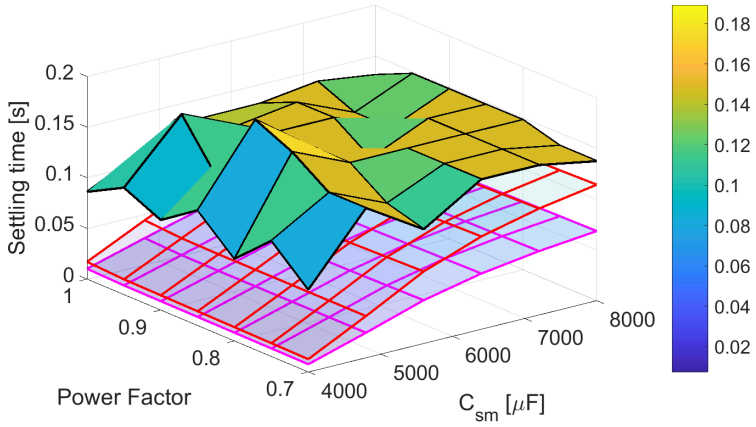

(b)

Fig. 4.8: SM voltage settling times with perturbation of (a) +5% (b) −10% (c) +2% change in V_{DC} for SM capacitance and power factor parametric analysis. Time bounds predicted by model in lower opacity, measured time in higher opacity. (Continued on next page)

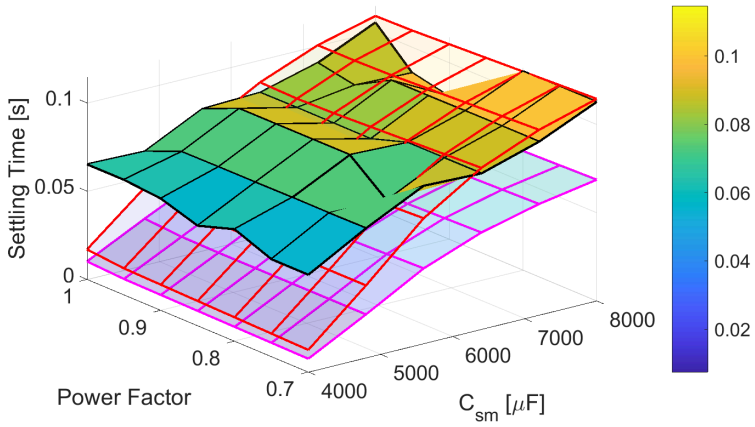

(c)

Fig. 4.8: (Continued from previous page) SM voltage settling times with perturbation of (a) +5% (b) −10% (c) +2% change in V_{DC} for SM capacitance and power factor parametric analysis. Time bounds predicted by model in lower opacity, measured time in higher opacity.

the smallest perturbation applied is theoretically the most accurate of the presented cases. It is noted that in this case particularly, there is some effect of the increasing inductive load for large C_{sm} values when the model becomes more accurate. Therefore, it can be concluded that a more inductive load may slow down the settling time, but it is not very significant. This means that the focus on component sizing should still be primarily associated with the SM capacitance and arm inductance. Similar to the modulation index, the load power factor is not as inherent to the operation of the MMC.

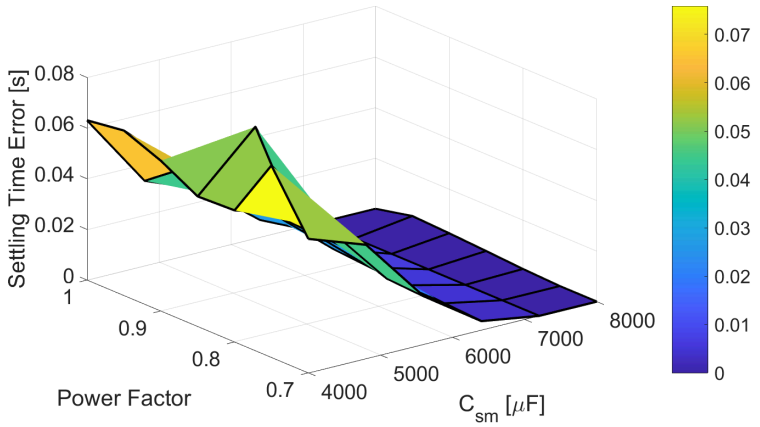

(a)

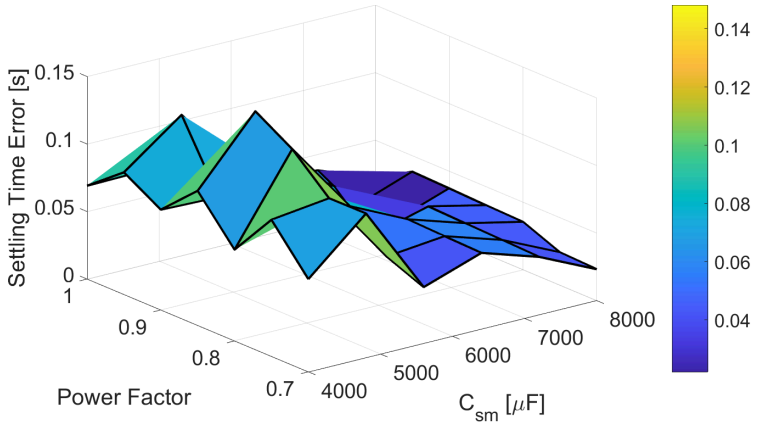

(b)

Fig. 4.9: Error of model SM voltage settling times subjected to a perturbation of (a) +5% (b) −10% (c) +2% change in V_{DC} for the SM capacitance and power factor parametric analysis considering (d) peak-to-peak SM voltage ripple. (Continued on next page)

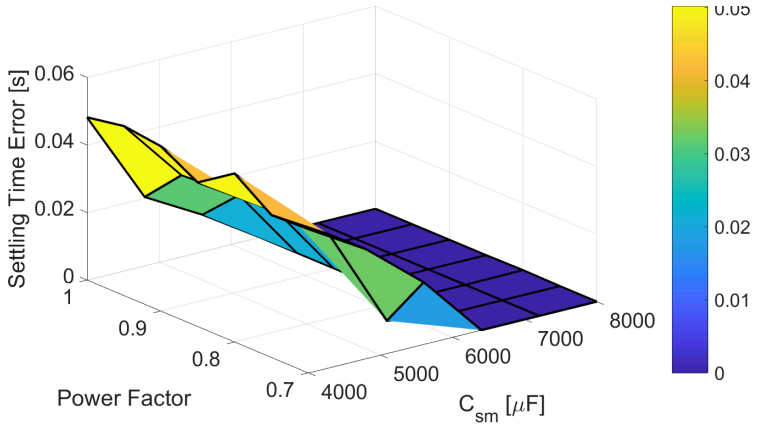

(c)

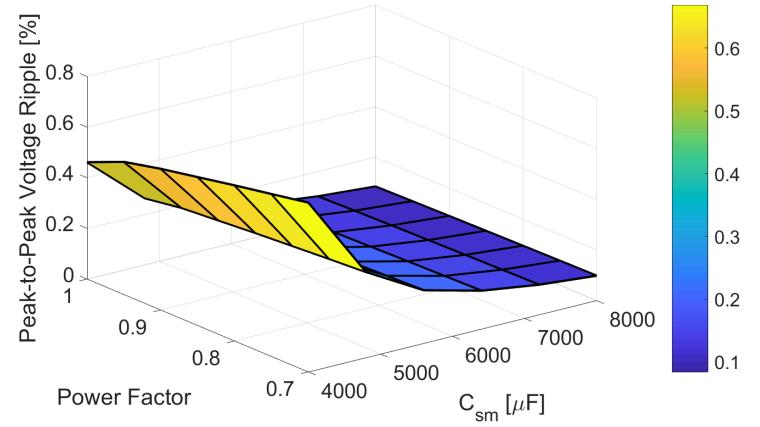

(d)

Fig. 4.9: (Continued from previous page) Error of model SM voltage settling times subjected to a perturbation of (a) +5% (b) −10% (c) +2% change in V_{DC} for the SM capacitance and power factor parametric analysis considering (d) peak-to-peak SM voltage ripple.

4.4 Summary

In this chapter, a 2×2 state space model was developed for the DC components of the SM voltage and arm current of the MMC. The model was compared against PSCAD/EMTDC simulations and shown to be able to capture the DC behaviour of these waveforms. Furthermore, when the AC transients are not significant (compared to the DC transients), the model can capture the full waveform of these waveforms. More importantly, from the model a closed-form equation for the settling time of the SM voltages of the MMC was derived. It was shown that increasing the SM capacitance and arm inductance are primary factor for increasing the settling time. On the other hand, factors relating to the operating point of the MMC, such as the modulation index and load power factor, did not have much effect on the settling time. The equation may be used as a design tool to size the components and determine the operating point of an MMC that meet a specified response speed. This is a key factor to the effectiveness of energy control in mitigating frequency excursions. Various parametric analyses were conducted to investigate the impact of such parameters on the response speed.

Chapter 5

Contributions, Conclusions, and Recommendations for Future Work

As electrical power generation becomes increasingly dominated by RESs, the contribution from SGs becomes proportionally less. However, RESs do not possess the large inherent inertia as SGs do, which results in a decreasing system inertia. This means that the natural inherent frequency damping may no longer be sufficient. Control schemes are implemented in MMCs to provide them with frequency support capability to help address this concern. However, the implementation is not simple. There are various factors that must be considered in order to provide the proper controller requirements and parameters to the control scheme. Otherwise, the intended merits from the controls may be compromised. In this thesis, the use of a frequency support control scheme in an MMC and how different system parameters affect its performance were investigated and analyzed both qualitatively and quantitatively. The main contributions and conclusions are summarized in this chapter, and recommendations to extend the scope of study are also identified.

5.1 Main Contributions and Conclusions

In this research, an energy-based control frequency support scheme was implemented in an MMC. This allows the MMC to respond to power imbalances by absorbing/releasing some of its internally stored energy when the system is subjected to a perturbation. Impacts of different system parameters on how effectively the control scheme mitigated frequency excursions were investigated through simulation studies, and a model was developed to provide a mathematical basis of the observations. The following are the main contributions and conclusions of this thesis:

- A system consisting of SGs and MMCs implemented with frequency support capability was developed in PSCAD/EMTDC. The frequency nadir and duration of the arresting period were observed through detailed simulation studies for when energy control was and was not implemented to evaluate the improvement in the inertial response. Results showed that the energy-based control frequency support scheme does not necessarily improve the frequency response. When it does, however, energy control improves the frequency response by extending the duration of the arresting period. The changes in the frequency nadir were relatively less due to the limited variation allowed in the energy stored in the MMC.

- The energy storage capacity of the MMC, the RES penetration level, and system inertia were varied in a parametric manner to investigate how these factors affect the performance of the energy-based control frequency support scheme. This was done for two different converters and under two different perturbations. Results showed that increasing the energy storage capacity of the MMC extended the duration that the frequency support scheme was active for, resulting in longer arresting periods. The

same was seen with increasing RES penetration levels, but in larger amount due to the greater increases in the total amount of available energy that can be used for frequency support. The quantitative improvements were not linear as expected from theory due to the non-linearities in the control system. Furthermore, the energy-based control scheme does not fully compensate the effect of the decreasing system inertia. This showed that the system inertia is a determining factor on the necessity of frequency support. Furthermore, the usability of energy control decreases with increasing perturbations due to the amount of energy that is required and the faster rates at which it must change.

- A state-space model representing the DC dynamics of the MMC was developed based on the fundamental differential equations of MMC operation, from which a closed-form equation for the MMC settling time was derived. The model was implemented as a custom component in PSCAD/EMTDC, and results were compared against detailed simulations in PSCAD/EMTDC. It was demonstrated that as the energy storage elements of the MMC increase, which are typically high when the MMC is designed for frequency support, that the dynamics of the arm currents and SM voltages are dominated by their DC components.

- The impact of the SM capacitance, arm inductance, modulation index, and load power factor of the MMC on its natural response speed were quantitatively evaluated using the model equation and the simulated waveforms from PSCAD/EMTDC. Results showed that the SM capacitance and arm inductance have a primary impact on the settling time of the arm current and SM voltages. Furthermore, their impact is non-linear and has a coupled effect. The modulation index and load power factor have less impact.

5.2 Future Work

In this thesis, parametric studies were conducted by simulations to study the impact of energy control on the system frequency response under different system and operating conditions. This has provided insight towards the design of MMCs for energy control as the RES penetration level of the grid increases. Due to the many possibilities of MMC, controllers, as well as system configurations and parameters, further research in this direction is available. The following extensions to this research are proposed:

- Conduct parametric analyses for different frequency support (energy control based) schemes. In this thesis, only one general energy control method for frequency support was studied. However, other schemes can be studied such as those that are inertia emulation based or require more input measurements such as ROCOF.

- Study the effect of redundant SMs in the MMC. It was seen that the SM capacitance is a determining factor in the frequency response improvement contributed by energy control. With redundant SMs, the MMC has more energy that can be used for compensate power imbalances. The trade-offs between including more (redundant) SMs and the MMC response speed may be studied.

- Evaluate the effectiveness of energy control for different types of governors and turbines (e.g., steam). This research only used a hydro-type governor and turbine. It was seen that the system parameters had an effect on the natural frequency response, and therefore the necessity of energy control. Different governor/turbine actions may affect the requirements of energy control because of their different responses to a perturbation.

- Include frequency dependence in the system load. This research only considered a

frequency independent load. With frequency dependence, the system load and therefore the power compensation required by the energy controller will vary and likely affect the level of improvement in the inertial response acquired through energy control.

- Investigate the use of energy control for damping oscillations in the power system. The applicability of energy control is not limited to only improving the frequency response. Different uses of energy control may have different sizing guidelines for energy storage.

Appendix A

Model Equations

A.1 λ Equations

$$\lambda_1 = -\frac{N}{2} m_{1q} \tag{A.1a}$$

$$\lambda_2 = -\frac{N}{4\omega C_{\text{sm}}} \left(m_{1d} + \frac{m_{1q} m_{2q}}{4} + \frac{m_{1d} m_{2d}}{4} \right) \tag{A.1b}$$

$$\lambda_3 = R_{\text{eq}} \tag{A.1c}$$

$$\lambda_4 = \frac{N}{4\omega C_{\text{sm}}} \left(1 + \frac{m_{1d}^2 + m_{1q}^2}{8} - \frac{m_{2d}^2 + m_{2q}^2}{6} \right) - \omega L_{\text{eq}} \tag{A.1d}$$

$$\lambda_5 = -\frac{N}{4\omega C_{\text{sm}}} \left(\frac{3 m_{1q}}{4} + \frac{m_{1d} m_{2q}}{6} + \frac{m_{1q} m_{2d}}{3} \right) \tag{A.1e}$$

$$\lambda_6 = -\frac{N}{4\omega C_{\text{sm}}} \left(\frac{3 m_{1d}}{4} + \frac{m_{1d} m_{2d}}{6} + \frac{m_{1q} m_{2q}}{3} \right) \tag{A.1f}$$

$$\lambda_7 = -\frac{N}{2} m_{1d} \tag{A.1g}$$

$$\lambda_8 = \frac{N}{4\omega C_{\text{sm}}} \left(m_{1q} - \frac{m_{1q} m_{2d}}{4} + \frac{m_{1d} m_{2q}}{4} \right) \tag{A.1h}$$

$$\lambda_9 = -\lambda_4 \tag{A.1i}$$

$$\lambda_{10} = \lambda_3 \tag{A.1j}$$

$$\lambda_{11} = \frac{N}{4\omega C_{\mathrm{sm}}}\left(\frac{3m_{1d}}{4} + \frac{m_{1q}m_{2q}}{6} - \frac{m_{1d}m_{2d}}{3}\right) \tag{A.1k}$$

$$\lambda_{12} = -\frac{N}{4\omega C_{\mathrm{sm}}}\left(\frac{3m_{1q}}{4} - \frac{m_{1q}m_{2d}}{6} - \frac{m_{1d}m_{2q}}{3}\right) \tag{A.1l}$$

$$\lambda_{13} = -\frac{N}{2}m_{2q} \tag{A.1m}$$

$$\lambda_{14} = -\frac{N}{8\omega C_{\mathrm{sm}}}\left(m_{1q}^2 - m_{1d}^2 + m_{2d}\right) \tag{A.1n}$$

$$\lambda_{15} = -\lambda_5 \tag{A.1o}$$

$$\lambda_{16} = -\lambda_{11} \tag{A.1p}$$

$$\lambda_{17} = R_{\mathrm{arm}} \tag{A.1q}$$

$$\lambda_{18} = \frac{N}{4\omega C_{\mathrm{sm}}}\left(\frac{1}{2} + \frac{m_{1d}^2 + m_{1q}^2}{3}\right) - 2\omega L_{\mathrm{arm}} \tag{A.1r}$$

$$\lambda_{19} = -\frac{N}{2}m_{2d} \tag{A.1s}$$

$$\lambda_{20} = -\frac{N}{8\omega C_{\mathrm{sm}}}\left(2m_{1d}m_{1q} - m_{2q}\right) \tag{A.1t}$$

$$\lambda_{21} = -\lambda_6 \tag{A.1u}$$

$$\lambda_{22} = -\lambda_{12} \tag{A.1v}$$

$$\lambda_{23} = -\lambda_{18} \tag{A.1w}$$

$$\lambda_{24} = \lambda_{17} \tag{A.1x}$$

A.1.1 Special Case: Fundamental Component Only in m^{ref}

$$\lambda_{13} = 0 \tag{A.2a}$$

$$\lambda_{19} = 0 \tag{A.2b}$$

$$\lambda_{11} = -\lambda_6 \tag{A.2c}$$

$$\lambda_{12} = \lambda_5 \tag{A.2d}$$

A.2 ξ Equations

$$\xi_1 = \frac{1}{2NC_{\mathrm{sm}}}\Big(\frac{\lambda_{24}\lambda_{13} - \lambda_{19}\lambda_{18}}{\lambda_{18}\lambda_{23} - \lambda_{17}\lambda_{24}}\lambda_{13} + \frac{\lambda_{17}\lambda_{19} - \lambda_{13}\lambda_{23}}{\lambda_{18}\lambda_{23} - \lambda_{17}\lambda_{24}}\lambda_{19} + \frac{\kappa_2\kappa_7 + \kappa_1\kappa_8}{\kappa_6\kappa_7 - \kappa_5\kappa_8}\kappa_{11} + \frac{\kappa_1\kappa_6 + \kappa_2\kappa_5}{\kappa_6\kappa_7 - \kappa_5\kappa_8}\kappa_{12}\Big) \tag{A.3a}$$

$$\xi_2 = \frac{1}{2NC_{\mathrm{sm}}}\Big(N + \frac{\lambda_{24}\lambda_{14} - \lambda_{20}\lambda_{18}}{\lambda_{18}\lambda_{23} - \lambda_{17}\lambda_{24}}\lambda_{13} + \frac{\lambda_{17}\lambda_{20} - \lambda_{14}\lambda_{23}}{\lambda_{18}\lambda_{23} - \lambda_{17}\lambda_{24}}\lambda_{19} + \frac{\kappa_4\kappa_7 + \kappa_3\kappa_8}{\kappa_6\kappa_7 - \kappa_5\kappa_8}\kappa_{11} + \frac{\kappa_3\kappa_6 + \kappa_4\kappa_5}{\kappa_6\kappa_7 - \kappa_5\kappa_8}\kappa_{12}\Big) \tag{A.3b}$$

$$\xi_3 = \frac{-1}{2L_{\mathrm{arm}}}\Big(N + \frac{\lambda_{24}\lambda_{13} - \lambda_{19}\lambda_{18}}{\lambda_{18}\lambda_{23} - \lambda_{17}\lambda_{24}}\lambda_{14} - \frac{\lambda_{17}\lambda_{20} - \lambda_{14}\lambda_{23}}{\lambda_{18}\lambda_{23} - \lambda_{17}\lambda_{24}}\lambda_{20} - \frac{\kappa_2\kappa_7 + \kappa_1\kappa_8}{\kappa_6\kappa_7 - \kappa_5\kappa_8}\kappa_9 - \frac{\kappa_1\kappa_6 + \kappa_2\kappa_5}{\kappa_6\kappa_7 - \kappa_5\kappa_8}\kappa_{10}\Big) \tag{A.3c}$$

$$\xi_4 = \frac{-1}{2L_{\mathrm{arm}}}\Big(2R_{\mathrm{arm}} - \frac{\lambda_{24}\lambda_{14} - \lambda_{20}\lambda_{18}}{\lambda_{18}\lambda_{23} - \lambda_{17}\lambda_{24}}\lambda_{14} - \frac{\lambda_{17}\lambda_{20} - \lambda_{14}\lambda_{23}}{\lambda_{18}\lambda_{23} - \lambda_{17}\lambda_{24}}\lambda_{20} - \frac{\kappa_4\kappa_7 + \kappa_3\kappa_8}{\kappa_6\kappa_7 - \kappa_5\kappa_8}\kappa_9 - \frac{\kappa_3\kappa_6 + \kappa_4\kappa_5}{\kappa_6\kappa_7 - \kappa_5\kappa_8}\kappa_{10}\Big) \tag{A.3d}$$

$$\xi_5 = \frac{1}{2L_{\text{arm}}} \tag{A.3e}$$

where

$$\kappa_1 = \lambda_1(\lambda_{17}\lambda_{24} - \lambda_{18}\lambda_{23}) + \lambda_5(\lambda_{19}\lambda_{18} - \lambda_{24}\lambda_{13}) + \lambda_6(\lambda_{13}\lambda_{23} - \lambda_{17}\lambda_{19}) \tag{A.4a}$$

$$\kappa_2 = \lambda_7(\lambda_{17}\lambda_{24} - \lambda_{18}\lambda_{23}) + \lambda_{11}(\lambda_{19}\lambda_{18} - \lambda_{24}\lambda_{13}) + \lambda_{12}(\lambda_{13}\lambda_{23} - \lambda_{17}\lambda_{19}) \tag{A.4b}$$

$$\kappa_3 = \lambda_2(\lambda_{17}\lambda_{24} - \lambda_{18}\lambda_{23}) + \lambda_5(\lambda_{20}\lambda_{18} - \lambda_{24}\lambda_{14}) + \lambda_6(\lambda_{14}\lambda_{23} - \lambda_{17}\lambda_{20}) \tag{A.4c}$$

$$\kappa_4 = \lambda_8(\lambda_{17}\lambda_{24} - \lambda_{18}\lambda_{23}) + \lambda_{11}(\lambda_{20}\lambda_{18} - \lambda_{24}\lambda_{14}) + \lambda_{12}(\lambda_{14}\lambda_{23} - \lambda_{17}\lambda_{20}) \tag{A.4d}$$

$$\kappa_5 = \lambda_3(\lambda_{17}\lambda_{24} - \lambda_{18}\lambda_{23}) + \lambda_5(\lambda_{21}\lambda_{18} - \lambda_{24}\lambda_{15}) + \lambda_6(\lambda_{15}\lambda_{23} - \lambda_{17}\lambda_{21}) \tag{A.4e}$$

$$\kappa_6 = \lambda_9(\lambda_{18}\lambda_{23} - \lambda_{17}\lambda_{24}) - \lambda_{11}(\lambda_{21}\lambda_{18} - \lambda_{24}\lambda_{15}) - \lambda_{12}(\lambda_{15}\lambda_{23} - \lambda_{17}\lambda_{21}) \tag{A.4f}$$

$$\kappa_7 = \lambda_4(\lambda_{18}\lambda_{23} - \lambda_{17}\lambda_{24}) - \lambda_5(\lambda_{22}\lambda_{18} - \lambda_{24}\lambda_{16}) - \lambda_6(\lambda_{16}\lambda_{23} - \lambda_{17}\lambda_{22}) \tag{A.4g}$$

$$\kappa_8 = \lambda_{10}(\lambda_{17}\lambda_{24} - \lambda_{18}\lambda_{23}) + \lambda_{11}(\lambda_{22}\lambda_{18} - \lambda_{24}\lambda_{16}) + \lambda_{12}(\lambda_{16}\lambda_{23} - \lambda_{17}\lambda_{22}). \tag{A.4h}$$

$$\kappa_9 = \lambda_2 + \frac{\lambda_{24}\lambda_{15} - \lambda_{21}\lambda_{18}}{\lambda_{18}\lambda_{23} - \lambda_{17}\lambda_{24}}\lambda_{14} + \frac{\lambda_{17}\lambda_{21} - \lambda_{15}\lambda_{23}}{\lambda_{18}\lambda_{23} - \lambda_{17}\lambda_{24}}\lambda_{20} \tag{A.4i}$$

$$\kappa_{10} = \lambda_8 + \frac{\lambda_{24}\lambda_{16} - \lambda_{22}\lambda_{18}}{\lambda_{18}\lambda_{23} - \lambda_{17}\lambda_{24}}\lambda_{14} + \frac{\lambda_{17}\lambda_{22} - \lambda_{16}\lambda_{23}}{\lambda_{18}\lambda_{23} - \lambda_{17}\lambda_{24}}\lambda_{20} \tag{A.4j}$$

$$\kappa_{11} = \lambda_1 + \frac{\lambda_{24}\lambda_{15} - \lambda_{21}\lambda_{18}}{\lambda_{18}\lambda_{23} - \lambda_{17}\lambda_{24}}\lambda_{13} + \frac{\lambda_{17}\lambda_{21} - \lambda_{15}\lambda_{23}}{\lambda_{18}\lambda_{23} - \lambda_{17}\lambda_{24}}\lambda_{19} \tag{A.4k}$$

$$\kappa_{12} = \lambda_7 + \frac{\lambda_{24}\lambda_{16} - \lambda_{22}\lambda_{18}}{\lambda_{18}\lambda_{23} - \lambda_{17}\lambda_{24}}\lambda_{13} + \frac{\lambda_{17}\lambda_{22} - \lambda_{16}\lambda_{23}}{\lambda_{18}\lambda_{23} - \lambda_{17}\lambda_{24}}\lambda_{19} \tag{A.4l}$$

References

[1] P. Kundur, *Power System Stability and Control*. New York, NY, USA: McGraw-Hill, 1994.

[2] Y. G. Rebours, D. S. Kirschen, M. Trotignon, and S. Rossignol, "A Survey of Frequency and Voltage Control Ancillary Services—Part I: Technical Features," *IEEE Transactions on Power Systems*, vol. 22, no. 1, pp. 350–357, 2007.

[3] J. Carrasco, L. Franquelo, J. Bialasiewicz, E. Galvan, R. PortilloGuisado, M. Prats, J. Leon, and N. Moreno-Alfonso, "Power-Electronic Systems for the Grid Integration of Renewable Energy Sources: A Survey," *IEEE Transactions on Industrial Electronics*, vol. 53, no. 4, pp. 1002–1016, 2006.

[4] B. Kroposki, B. Johnson, Y. Zhang, V. Gevorgian, P. Denholm, B.-M. Hodge, and B. Hannegan, "Achieving a 100% Renewable Grid: Operating Electric Power Systems with Extremely High Levels of Variable Renewable Energy," *IEEE Power and Energy Magazine*, vol. 15, no. 2, pp. 61–73, 2017.

[5] P. Bresesti, W. L. Kling, R. L. Hendriks, and R. Vailati, "HVDC Connection of Offshore Wind Farms to the Transmission System," *IEEE Transactions on Energy Conversion*, vol. 22, no. 1, pp. 37–43, 2007.

[6] N. Flourentzou, V. G. Agelidis, and G. D. Demetriades, "VSC-Based HVDC Power Transmission Systems: An Overview," *IEEE Transactions on Power Electronics*, vol. 24, no. 3, pp. 592–602, 2009.

[7] J. Sun, M. Li, Z. Zhang, T. Xu, J. He, H. Wang, and G. Li, "Renewable energy transmission by hvdc across the continent: system challenges and opportunities," *CSEE Journal of Power and Energy Systems*, vol. 3, no. 4, pp. 353–364, 2017.

[8] M. H. Okba, M. H. Saied, M. Z. Mostafa, and T. M. Abdel-Moneim, "High voltage direct current transmission - a review, part i," in *2012 IEEE Energytech*, 2012, pp. 1–7.

[9] E. W. Kimbark, *Direct current transmission*. Wiley-Interscience, 1971.

[10] O. E. Oni, I. E. Davidson, and K. N. I. Mbangula, "A review of LCC-HVDC and VSC-HVDC technologies and applications," in *2016 IEEE 16th International Conference on Environment and Electrical Engineering (EEEIC)*, 2016, pp. 1–7.

[11] L. Zuñiga-Garcia, A. Zaragoza-Hernández, J. M. Nadal-Martínez, G. A. Anaya-Ruiz, E. L. Moreno-Goytia, L. E. Ugalde-Caballero, and V. Venegas-Rebollar, "MMC technology and its participation in the integration of variable renewable energies and implementation of dc grids," in *2014 IEEE International Autumn Meeting on Power, Electronics and Computing (ROPEC)*, 2014, pp. 1–6.

[12] A. Lesnicar and R. Marquardt, "An innovative modular multilevel converter topology suitable for a wide power range," in *2003 IEEE Bologna Power Tech Conference Proceedings,*, vol. 3, 2003, pp. 6 pp. Vol.3–.

[13] S. Allebrod, R. Hamerski, and R. Marquardt, "New transformerless, scalable modular multilevel converters for hvdc-transmission," in *2008 IEEE Power Electronics Specialists Conference*, 2008, pp. 174–179.

[14] B. R. Andersen, "Hvdc transmission-opportunities and challenges," in *The 8th IEE International Conference on AC and DC Power Transmission*, 2006, pp. 24–29.

[15] H. Yang, Y. Dong, W. Li, and X. He, "Average-Value Model of Modular Multilevel Converters Considering Capacitor Voltage Ripple," *IEEE Transactions on Power Delivery*, vol. 32, no. 2, pp. 723–732, 2017.

[16] K. Ilves, A. Antonopoulos, S. Norrga, and H. Nee, "Steady-State Analysis of Interaction Between Harmonic Components of Arm and Line Quantities of Modular Multilevel Converters," *IEEE Transactions on Power Electronics*, vol. 27, no. 1, pp. 57–68, 2012.

[17] L. Harnefors, A. Antonopoulos, S. Norrga, L. Angquist, and H. Nee, "Dynamic Analysis of Modular Multilevel Converters," *IEEE Transactions on Industrial Electronics*, vol. 60, no. 7, pp. 2526–2537, 2013.

[18] S. Debnath, J. Qin, B. Bahrani, M. Saeedifard, and P. Barbosa, "Operation, control, and applications of the modular multilevel converter: A review," *IEEE Transactions on Power Electronics*, vol. 30, no. 1, pp. 37–53, 2015.

[19] A. Nami, J. Liang, F. Dijkhuizen, and G. D. Demetriades, "Modular Multilevel Converters for HVDC Applications: Review on Converter Cells and Functionalities," *IEEE Transactions on Power Electronics*, vol. 30, no. 1, pp. 18–36, 2015.

[20] K. Sharifabadi, L. Harnefors, H.-P. Nee, S. Norrga, and R. Teodorescu, *Design, Control, and Application of Modular Multilevel Converters for HVDC Transmission Systems*, 1st ed., ser. Wiley - IEEE. Wiley, 2016.

[21] A. L. P. de Oliveira, C. E. Tibúrcio, M. N. Lemes, and D. Retzmann, "Prospects of Voltage-Sourced Converters (VSC) applications in DC transmission systems," in *2010 IEEE/PES Transmission and Distribution Conference and Exposition: Latin America (T D-LA)*, 2010, pp. 491–495.

[22] F. Blaabjerg, R. Teodorescu, M. Liserre, and A. V. Timbus, "Overview of Control and Grid Synchronization for Distributed Power Generation Systems," *IEEE Transactions on Industrial Electronics*, vol. 53, no. 5, pp. 1398–1409, 2006.

[23] F. Blaabjerg, Zhe Chen, and S. B. Kjaer, "Power electronics as efficient interface in dispersed power generation systems," *IEEE Transactions on Power Electronics*, vol. 19, no. 5, pp. 1184–1194, 2004.

[24] J. W. Ingleson and E. Allen, "Tracking the Eastern Interconnection frequency governing characteristic," in *IEEE PES General Meeting*, 2010, pp. 1–6.

[25] "IEEE Standard for Interconnection and Interoperability of Distributed Energy Resources with Associated Electric Power Systems Interfaces," *IEEE Std 1547-2018 (Revision of IEEE Std 1547-2003)*, pp. 1–138, 2018.

[26] *RM11-7-000 Frequency Regulation Compensation in the Organized Wholesale Power Markets*, FERC, Washington, DC, USA, 2011.

[27] M. Saeedifard and R. Iravani, "Dynamic Performance of a Modular Multilevel Back-to-Back HVDC System," *IEEE Transactions on Power Delivery*, vol. 25, no. 4, pp. 2903–2912, 2010.

[28] Q. Tu, Z. Xu, and L. Xu, "Reduced Switching-Frequency Modulation and Circulating Current Suppression for Modular Multilevel Converters," *IEEE Transactions on Power Delivery*, vol. 26, no. 3, pp. 2009–2017, 2011.

[29] R. Eriksson, N. Modig, and K. Elkington, "Synthetic inertia versus fast frequency response: a definition," *IET renewable power generation*, vol. 12, no. 5, pp. 507–514, 2018.

[30] H.-P. Beck and R. Hesse, "Virtual synchronous machine," in *2007 9th International Conference on Electrical Power Quality and Utilisation*, 2007, pp. 1–6.

[31] I. Cvetkovic, D. Boroyevich, R. Burgos, Chi Li, M. Jaksic, and P. Mattavelli, "Modeling of a virtual synchronous machine-based grid-interface converter for renewable energy systems integration," in *2014 IEEE 15th Workshop on Control and Modeling for Power Electronics (COMPEL)*, 2014, pp. 1–7.

[32] S. D'Arco and J. A. Suul, "Virtual synchronous machines — Classification of implementations and analysis of equivalence to droop controllers for microgrids," in *2013 IEEE Grenoble Conference*, 2013, pp. 1–7.

[33] Q. Zhong and G. Weiss, "Synchronverters: Inverters That Mimic Synchronous Generators," *IEEE Transactions on Industrial Electronics*, vol. 58, no. 4, pp. 1259–1267, 2011.

[34] Z. Lv and Q. Zhong, "Control of modular multilevel converters as virtual synchronous machines," in *2017 IEEE Power Energy Society General Meeting*, 2017, pp. 1–5.

[35] C. Verdugo, J. I. Candela, and P. Rodriguez, "Grid support functionalities based on modular multilevel converters with synchronous power control," in *2016 IEEE International Conference on Renewable Energy Research and Applications (ICRERA)*, 2016, pp. 572–577.

[36] S. D'Arco, G. Guidi, and J. A. Suul, "Operation of a Modular Multilevel Converter Controlled as a Virtual Synchronous Machine," in *2018 International Power Electronics Conference (IPEC-Niigata 2018 -ECCE Asia)*, 2018, pp. 782–789.

[37] J. Hu, J. Zhu, and M. Wan, "Modeling and Analysis of Modular Multilevel Converter in DC Voltage Control Timescale," *IEEE Transactions on Industrial Electronics*, vol. 66, no. 8, pp. 6449–6459, 2019.

[38] H. Ali, B. Li, Z. Xu, H. Liu, and D. Xu, "Virtual Synchronous Generator Design Based Modular Multilevel Converter for Microgrid Frequency Regulation," in *2019 22nd International Conference on Electrical Machines and Systems (ICEMS)*, 2019, pp. 1–6.

[39] D. Panda, B. S. Raipurohit, and A. Monti, "Synthetic Inertia for Frequency Regulation of Electric Grid using Modular-Multilevel Converter," in *2019 IEEE Industry Applications Society Annual Meeting*, 2019, pp. 1–8.

[40] J. Fang, H. Li, Y. Tang, and F. Blaabjerg, "On the Inertia of Future More-Electronics Power Systems," *IEEE Journal of Emerging and Selected Topics in Power Electronics*, vol. 7, no. 4, pp. 2130–2146, 2019.

[41] I. M. Sanz, P. D. Judge, C. E. Spallarossa, B. Chaudhuri, and T. C. Green, "Dynamic Overload Capability of VSC HVDC Interconnections for Frequency Support," *IEEE Transactions on Energy Conversion*, vol. 32, no. 4, pp. 1544–1553, 2017.

[42] C. E. Spallarossa, M. M. C. Merlin, and T. C. Green, "Augmented inertial response of Multi-Level Converters using internal energy storage," in *2016 IEEE International Energy Conference (ENERGYCON)*, 2016, pp. 1–6.

[43] S. Samimi, F. Gruson, P. Delarue, F. Colas, M. M. Belhaouane, and X. Guillaud, "MMC Stored Energy Participation to the DC Bus Voltage Control in an HVDC Link," *IEEE Transactions on Power Delivery*, vol. 31, no. 4, pp. 1710–1718, 2016.

[44] M. Hagiwara and H. Akagi, "Control and Experiment of Pulsewidth-Modulated Modular Multilevel Converters," *IEEE Transactions on Power Electronics*, vol. 24, no. 7, pp. 1737–1746, 2009.

[45] K. Shinoda, A. Benchaib, J. Dai, and X. Guillaud, "Virtual Capacitor Control: Mitigation of DC Voltage Fluctuations in MMC-based HVdc Systems," *IEEE Transactions on Power Delivery*, vol. 33, no. 1, pp. 455–465, 2018.

[46] ——, "Virtual capacitor control for stability improvement of hvdc system comprising dc reactors," in *15th IET International Conference on AC and DC Power Transmission (ACDC 2019)*, 2019, pp. 1–6.

[47] S. Debnath and M. Chinthavali, "Control of MMC-HVDC in low-inertia weak grids," in *2017 IEEE 12th International Conference on Power Electronics and Drive Systems (PEDS)*, 2017, pp. 435–441.

[48] S. Yang, J. Fang, Y. Tang, H. Qiu, C. Dong, and P. Wang, "Modular Multilevel Converter Synthetic Inertia-Based Frequency Support for Medium-Voltage Microgrids," *IEEE Transactions on Industrial Electronics*, vol. 66, no. 11, pp. 8992–9002, 2019.

[49] G. T. Son, H. Lee, T. S. Nam, Y. Chung, U. Lee, S. Baek, K. Hur, and J. Park, "Design and Control of a Modular Multilevel HVDC Converter With Redundant Power Modules for Noninterruptible Energy Transfer," *IEEE Transactions on Power Delivery*, vol. 27, no. 3, pp. 1611–1619, 2012.

[50] B. Li, W. Zhang, and J. He, "Inertia emulation and dynamic voltage support scheme for mmc-based dc systems," *IET Renewable Power Generation*, vol. 13, no. 1, pp. 146–154, 2019.

[51] H. Kim, J. Kang, J. W. Shim, J. Beerten, D. Van Hertem, H. Jung, C. Kim, and K. Hur, "Exploiting Redundant Energy of MMC–HVDC to Enhance Frequency Response of Low Inertia AC Grid," *IEEE Access*, vol. 7, pp. 138 485–138 494, 2019.

[52] K. Shinoda, A. Benchaib, J. Dai, and X. Guillaud, "DC voltage control of MMC-based HVDC grid with Virtual Capacitor Control," in *2017 19th European Conference on Power Electronics and Applications (EPE'17 ECCE Europe)*, 2017, pp. P.1–P.10.

[53] Q. Hong, M. Nedd, S. Norris, I. Abdulhadi, M. Karimi, V. Terzija, B. Marshall, K. Bell, and C. Booth, "Fast frequency response for effective frequency control in power systems

with low inertia," *Journal of engineering (Stevenage, England)*, vol. 2019, no. 16, pp. 1696–1702, 2019.

[54] K. Ilves, S. Norrga, L. Harnefors, and H. Nee, "On Energy Storage Requirements in Modular Multilevel Converters," *IEEE Transactions on Power Electronics*, vol. 29, no. 1, pp. 77–88, Jan 2014.

[55] H. Bärnklau, A. Gensior, and S. Bernet, "Submodule Capacitor Dimensioning for Modular Multilevel Converters," *IEEE Transactions on Industry Applications*, vol. 50, no. 3, pp. 1915–1923, 2014.

[56] M. M. C. Merlin and T. C. Green, "Cell capacitor sizing in multilevel converters: cases of the modular multilevel converter and alternate arm converter," *IET Power Electronics*, vol. 8, no. 3, pp. 350–360, 2015.

[57] Z. Ke, J. Pan, K. Potty, W. Perdikakis, A. Shanmuganaatham, M. A. Sabbagh, J. Zhang, F. Luo, J. Wang, and L. Xu, "Optimal submodule capacitor sizing for modular multilevel converters with common mode voltage injection and circulating current control," in *2017 IEEE Energy Conversion Congress and Exposition (ECCE)*, 2017, pp. 1802–1808.

[58] C. Oates, "Modular Multilevel Converter Design for VSC HVDC Applications," *IEEE Journal of Emerging and Selected Topics in Power Electronics*, vol. 3, no. 2, pp. 505–515, 2015.

[59] Z. Xu, H. Xiao, and Z. Zhang, "Selection methods of main circuit parameters for modular multilevel converters," *IET Renewable Power Generation*, vol. 10, no. 6, pp. 788–797, 2016.

[60] Y. Tang, L. Ran, O. Alatise, and P. Mawby, "Capacitor Selection for Modular Multilevel Converter," *IEEE Transactions on Industry Applications*, vol. 52, no. 4, pp. 3279–3293, 2016.

[61] Z. Yin, H. Qiu, Y. Yang, Y. Tang, and H. Wang, "Practical Submodule Capacitor Sizing for Modular Multilevel Converter Considering Grid Faults," *Applied sciences*, vol. 10, no. 10, pp. 3550–, 2020.

[62] R. Oliveira and A. Yazdani, "An Enhanced Steady-State Model and Capacitor Sizing Method for Modular Multilevel Converters for HVdc Applications," *IEEE Transactions on Power Electronics*, vol. 33, no. 6, pp. 4756–4771, 2018.

[63] H. Jiang and B.-T. Ooi, "Damping analysis for transients of modular multilevel converter," in *2017 IEEE Energy Conversion Congress and Exposition (ECCE)*. IEEE, 2017, pp. 1527–1531.

[64] C. Zhao and T. Li, "Recovering the modular multilevel converter from a cleared or isolated fault," *IET generation, transmission & distribution*, vol. 9, no. 6, pp. 550–559, 2015.